Study for the computational resolution of conservation equations of mass, momentum and energy

Application to solar receivers in Concentrated Solar Power plants

Giulio Beseghi

Thesis to obtain the Master of Science Degree in

Energy Engineering and Management

Supervisors: Prof. Luís Filipe Moreira Mendes
Prof. Carlos-David Perez Segarra

Examination Committee

Chairperson: Prof. Edgar Caetano Fernandes
Supervisor: Prof. Luís Filipe Moreira Mendes
Member of the Committee: Prof. João Carlos de Campos Henriques

November 2017

Acknowledgments

First, I would like to thank my supervisors Carlos-David Perez Segarra and Luís Filipe Moreira Mendes. Segarra helped me throughout the whole process of the development of the code, giving me important advice and helping me to resolve all the problems that I encountered. Mendes supported me in the thesis writing process, giving me important information about how to structure and present my work, making me understand its flaws and how I could improve them.

I would also like to thank all the team at CTTC: professor Oliva, for giving me the opportunity to develop my thesis at such an important and qualified center; professor Trias, for helping me in the study of turbulence and natural convection, giving me all the bibliographic resources that I needed; the rest of the team, always available when I needed to ask help for the procedure used to develop my codes and to compare the results obtained.

Finally, I would like to thank my parents Andrea and Alessandra, for supporting me from the beginning and making my whole master experience possible; my grandparents Giovanna and Giorgio, for never doubting on me and making me feel proud of my work; my sister Maria, for trusting in me in these months; my girlfriend María, for cheering me up anytime I needed it. All of them, for the love they give me every day.

Abstract

The objective of the thesis is to provide a focused, comprehensive code based on Computational Fluid Dynamics to be applied to the study of natural and mixed convection of the air located outside an external cylindrical receiver of a Concentrating Solar Power (CSP) plant. CSP plants are a rapidly improving technology that is going to play an increasingly important role in electricity production in the decades to come. Convection of outer air in CSP plants represent a major concern mainly for two reasons: it must be solved to assess the thermal balance at the receiver and to calculate the local temperature of the materials; in fact, failure still represents an issue for the design of this component. The code will need to be able to describe both aspects. Therefore, a Direct Numerical Simulation approach is used, since it is able to solve thoroughly the three main equations that govern convection: the mass, momentum and energy conservation equations. In order to evaluate the change of the thermophysical properties due to the variation of temperature, a non-Boussinesq approach is proposed to solve the equations. After a contextualization of the external air convective losses of a Central Receiver System, the code is progressively built and validated, and a possible setup for its application to the thermal receiver is presented.

Keywords

Concentrating Solar Power; Computational Fluid Dynamics; Thermal receiver; Natural convection.

Resumo

O objetivo da presente tese é o desenvolvimento de um código abrangente e dedicado a ser aplicado ao estudo das convecções natural e mista em torno de um receptor cilíndrico externo de uma central de energia solar com concentração para produção de eletricidade (CSP). As centrais CSP são uma tecnologia em rápido desenvolvimento e que irá desempenhar um papel fundamental na produção de eletricidade nas próximas décadas. A convecção em torno dos recetores de centrais CSP reveste-se da maior importância e é um processo que tem de ser conhecido com duas finalidades: cálculo do balanço térmico do recetor; cálculo das temperaturas locais - a falha dos materiais devido à temperatura continua a ser um dos maiores problemas a solucionar no projeto deste componente. O código terá de ser capaz de descrever ambos os aspetos. Deste modo, foi usada uma abordagem de Simulação Numérica Direta pois permite resolver simultaneamente as três principais equações que governam a convecção: conservação de massa, momento e energia. Para estimar as variações das propriedades físicas dos materiais com a temperatura é proposta a uma abordagem do tipo non-Boussinesq para resolver as equações. Após uma contextualização das perdas convectivas devidas ao ar exterior num sistema de recetor central, o código é progressivamente construído e validado e um caso possível da sua aplicação a uma recetor é apresentado.

Palavras Chave

Energia Solar com Concentração; Mecânica dos Fluidos Computacional; Recetor Térmico; Convecção Natural.

Contents

List of Figures

List of Tables

List of Variables

G_{sc}	solar constant
G_{on}	extraterrestrial radiation
η_{opt}	optical efficiency
η_{th}	thermal efficiency
θ	incidence angle
G_{bt}	beam radiation on tilted surface
G_{bn}	beam radiation parallel to the sun rays
$\mathbf{n_s}$	sun ray direction
$\mathbf{n_c}$	direction normal to the surface
η_{cos}	cosine efficiency
ρ_h	heliostat reflectivity
η_{ref}	reflectiivity efficiency
η_{bs}	blocking & shading efficiency
τ_{atm}	atmospheric transmittance
H_T	tower focal height
ξ	broadband extinction coefficient
R	slant range
ξ	broadband extinction coefficient
V_R	visibility range
β	scattering coefficient
ρ_w	vapor concentration
H_s	site elevation
A_0, S_0, C_0	altitude and vapor-dependent reference constants
A, S, C	altitude and vapor-dependent constants adjusted for scattering
η_{atm}	atmospheric attenuation efficiency
σ_{tot}	total standard deviation
σ_{sun}	sunshape error

σ_s	surface error
σ_t	tracker error
η_{spil}	spillage efficiency
$\dot{Q}_{in}$	incident power
$\dot{Q}_{lost}$	lost power
$\dot{Q}_{ref}$	reflected power
$\dot{Q}_{cond}$	conductive power
$\dot{Q}_{conv}$	convective power
$\dot{Q}_{rad}$	radiative power
$\dot{Q}_{rec}$	power absorbed by the receiver
α_r	receiver absorptance related to the solar bandwidth
ρ_r	receiver reflectivity
h	heat transfer coefficient
T_r	receiver temperature
h_f, h_n	heat transfer coefficient due to forced and natural convection respectively
k_s	surface roughness
D	diameter
k	conductivity
ρ	density
$u\,v\,w$	velocity components along the x, y, z direction
μ	dynamic viscosity
c_P	specific heat
Re	Reynolds number
Nu	Nusselt number
Gr	Grashof number
T_{amb}	ambient temperature
T_{film}	film temperature
g, $\mathbf{g}$	gravity constant, gravity constant vector
β	air expansion coefficient
H	height
σ	Boltzmann constant
ε_r	receiver emissivity
T_{sg}	sky-ground temperature
F_{view}	view factor
A_r	receiver area

A_c	collector area
C_r	concentration ratio
ψ	variable of interest
$\hat{\psi}$	variable of interest expressed in the non-dimensional form
t	time
$\mathbf{u}$	velocity vector
Γ	diffusion coefficient
S_ϕ	source term
$\boldsymbol{\tau}$	deviatoric stress tensor
p	pressure
$\mathbf{f_e}$	diffusion coefficient
$\dot{\mathbf{q}}$	heat flux
u	specific internal energy
Ψ_e	specific internal energy source
$\mathbf{S}$	rate-of-strain tensor
$\mathbf{G}$	velocity gradient tensor
$\boldsymbol{\Omega}$	skew symmetric part of the velocity gradient tensor
ψ	stream function
ω	vorticity
P, W, E, S, N, T, B	principal, west, east, south, north, top, bottom nodes
w, e, s, n, t, b	west, east, south, north, top, bottom faces
a_W, a_E, a_S, a_N, a_T, a_B, a_P, b_P	discretization coefficients
C	Courant number
δ	convergence parameter
N, M, Q	number of nodes along the x, y, z direction
Pe	Peclet number
Ra	Rayleigh number
α	thermal diffusivity
γ	concentration factor
ν	cinematic viscosity
u_τ	shear velocity
τ_w	wall shear stress
y^+, u^+	distance and velocity expressed in wall coordinates

Acronyms

CCGT	Combined Cycle Gas Turbine
CDS	Central Difference Scheme
CFD	Computational Fluid Dynamics
CFL	Courant–Friedrichs–Lewy
CRS	Central Receiver System
CSP	Concentrated Solar Power
CPU	Central Processing Unit
DHC	Differentially Heated Cavity
DNI	Direct Normal Irradiance
DNS	Direct Numerical Simulation
EOS	Equation Of State
FSM	Fractional Step Method
FDM	Finite Difference Method
FVM	Finite Volume Method
HTF	Heat-Transfer Fluid
HRS	High Resolution Scheme
IEA	International Energy Agency
LCOE	Levelized Cost Of Electricity
LES	Large Eddy Simulation

LFR	Linear Fresnel Reflector
O&M	Operation & Maintenance
PBC	Periodic Boundary Conditions
PCM	Phase Change Material
PDE	Partial Differential Equation
PDS	Parabolic Dish System
PTC	Parabolic Trough Collector
QUICK	Quadratic Upstream Interpolation for Convective Kinematics
R&D	Research & Development
SMART	Sharp and Monotonic Algorithm for Realistic Transport
SUDS	Second-order Upwind Difference Scheme
TDMA	Tri-Diagonal Matrix Algorithm
TES	Thermal Energy Storage
UDS	Upwind Difference Scheme
WALE	Wall-Adapting Local Eddy

1

Introduction

Contents

Renewable energy has been achieving an increasingly large impact on electricity generation in the last decades, especially in the developed countries. Despite being known since the 19th century as hydroelectricity, its exploitation saw a recent acceleration, resulting in an increase of renewable energy production from $1.29\,\mathrm{Mtoe}$ in 2000 up to $1.89\,\mathrm{Mtoe}$ in 2014 (roughly a 50% increase) [1]. This is mainly due to two principal causes: the improvement of the existing technologies, both in terms of efficiency and profitability, and the growing interest of the public administrations, more and more concerned about the problematics of the well-established fossil-fuel energy generation. For this reason, in a future perspective the clean energy share is expected to rise at a high rate, and producers must follow the technological trend promoted by research and development. To do so, it has always been important to develop tools that describe the main phenomena involved in the power generation, in order to obtain a deep knowledge of the whole process. The reasons are several. Firstly, a correct modelization leads to a maximization of the efficiency. Efficiency is a crucial factor in energy generation, because of its direct impact on the cost of energy: a high efficiency involves lower costs and therefore major competitiveness. From this point of view, a consistent model is also responsible for a better understanding of the most critical processes. This helps to choose the most suitable technologies to adopt, leading to an optimization of the costs (initial investment and Operation & Maintenance (O&M) during the lifespan of the facility), as well as major safety.

The physical phenomena involved in energy production are countless: material strain, fatigue, phase change, oxidation, molecular diffusion, nuclear reaction, etc. However, any technology can be somehow identified by its energy transformation processes, that are crucial within the whole energy production. The traditional fossil-fuel energy transformation passes through four typical main steps: firstly a **combustion** increases the enthalpy of an oxidizing agent (usually oxygen, mixed with air), then the **heat transfer** increases the enthalpy of another fluid (the so-called “energy vector”), subsequently the **impact** of the fluid with a turbine makes the latter increase its rotation, and finally the **electromagnetic interaction** of an electric machine converts the kinetic energy of the turbine into the energy associated with the electric field generated. At least one of these energy transformations occurs also in any type of renewable energy production. In particular, heat transfer and kinetic energy transfer are particularly interesting to be analyzed, because they occur with almost all technologies and are the main ones that affect the efficiency (for instance, heat transfer in Concentrated Solar Power (CSP) and kinetic energy transfer in Wind Energy). Many times, heat and kinetic energy transfer occur in a single process simultaneously. In fact, the phenomena are strictly correlated, and most of the times cannot be treated as separated. Let us think, for instance, about a heater in a room. The temperature gradient makes the air move, since hot air is lighter than cold air. This motion transports the hot air, that consequently heats the nearby cold air through thermal diffusion. Heat transfer is responsible for motion, but motion is responsible for heat transfer as well. Even though these two phenomena cannot be treated separately, it is interesting to notice that they can always be treated as a whole using the conservation equation of three physical properties: mass, momentum, and energy. The three equations are, respectively, the continuity equation, the Navier-Stokes equation, and the thermal energy equation.

1.1 The reason for Computational Fluid Dynamics

The solution of this system of equations helps to describe energy transformation processes and can be used to optimize the output of a power plant, thanks to a correct design of the components. Solving the equations, though, is not an easy task. In very few cases some of them can be solved analytically; for instance, in a 1D laminar flow in a tube. In most occurrences, however, the complexity of the problem makes it impossible to obtain an analytical solution. As a consequence, two main approaches are available: the use of empirical correlations and the use of numerical simulation.

An empirical correlation is a formula that comes from experimental evidence: although it is not supported by a strict and rigorous theoretical model, it has been proved to be exhaustive to describe a phenomenon in its particular configuration. Yet these formulas are not rigorously justified by the theory, several times they are elaborated starting from a theoretical reasoning. Correlations are widely used in engineering, since they are a reliable tool, having been already tested practically. However, they feature some drawbacks. Firstly, many times they are only capable to describe a phenomenon as a whole, giving, as a result, a global variable, that is usually an average of the values in the entire region under study. Sometimes a general approach can be sufficient, but in numerous cases it is not: for instance, when designing a pipe, it is important to know the maximum operating temperature that it is expected to reach, not only the average. In other cases, it is crucial to understand where maxima and minima of local variables occur, to design components differently depending on the locations. Another shortcoming of the use of correlations is that many times they are strictly related to some specific configurations, or at least they are proved to be valid only for some of them.

This is the reason why a second approach is used as an alternative to correlations: numerical analysis. The aim of this method is to provide a stable, exhaustive and precise numerical solution of the phenomenological equations that describe a particular physical event. The reason why it is frequently not possible to solve these laws analytically is that they involve Partial Differential Equations (PDEs). The numerical simulation applied to fluid motion is called Computational Fluid Dynamics (CFD). CFD consists in a few basic steps. In the first place, all the infinitesimal terms are discretized by means of mathematical operators, so that a physical quantity is associated with them. Then, the domain is subdivided into a definite number of elements to be analyzed; these elements become the unknowns of the system of equations. With this approach, the original PDEs are reduced to a set of algebraic equations, the solution of which can be calculated through a computer. Of course every model is based on some hypotheses and assumptions, but once its limits are defined, numerical analysis is the procedure that provides the most accurate description of the phenomenon it is referred to. Still CFD has its limitations, too. Since it is a numerical method, the solution cannot be the exact one, given that the equations solved are not the real ones, but their approximation. Moreover, whenever an implicit method is used, any single unknown quantity converges to a value such that the algebraic equations give an error minor than a predefined convergence parameter; this error, although close to zero (normally it ranges from 10^{-4} to 10^{-6}), is impossible to avoid. Finally, a numerical simulation can reach an excessive Central Processing Unit (CPU) computational time. This occurs, for example, when the mesh needed to provide a correct solution needs to be extremely fine.[1] In fluid dynamics, this usually occurs in highly-turbulent flows, in which the eddy scales are remarkably small. These drawbacks are the reason why, in many cases, correlations are still preferred: ultimately, the objective is to seek a trade-off between accuracy and rapid solution.

1.2 Objective of the Thesis

The aim of this thesis is to propose an efficient and exhaustive method to describe the natural convection of external air at a thermal receiver of a CSP plant. Natural convection processes are governed by the three equations previously mentioned: mass, momentum, and energy conservation. It will be shown that a description of natural convection using a correlation method does not provide a sufficiently strong result: correlations are not capable to describe all the important phenomena that can arise in the heat and mass transfer processes of a fluid. Therefore, CFD will be the selected methodology to solve the equations, given the much higher reliability that it entails. Direct Numerical Simulation will be the CFD method used; this approach solves completely the three equations cited at any scale of motion of the fluid, giving particularly reliable results. A comprehensive method of solving the equations will be presented: the method considers the variation of the thermophysical properties of air due to the change of temperature. This method results to be more realistic than the assumption of constant thermophysical properties, since at the receiver the high temperatures can significantly affect the air properties. Only a few references in the literature regarding natural convection contemplate this aspect [2]; this thesis will provide one code that considers it and makes it suitable to be applied to the study of a receiver.

1.3 Thesis structure

The thesis will be articulated in five main Chapters. Chapter 1 has been already presented as the introduction. Chapter 2 will illustrate the principal CSP plant configurations and the state of the art of the

---

[1] A mesh is generally fine enough when the solution does not depend on it.

technology, to understand the main processes that occur in such facilities. As a part of it, an economic study will delineate the actual and future perspectives of profitability of this type of plant. Chapter 3 will present the equations of mass, momentum and energy in an elaborate way, and how CFD has to be applied to it. Chapter 4 will show benchmark cases to assess the validity of the developed codes. Finally, in Chapter 5, a possible application of the codes to the receiver of a CSP plant will be discussed, and the main conclusions of the work will be drawn.

2

Concentrated Solar Power

Contents

Concentrated (or Concentrating) Solar Power is a technology based on electricity generation given by a thermodynamic cycle of a fluid previously heated by concentrated solar radiation. Despite reaching a crescent interest only in the last few decades (especially due to the renewable energy shift trend), solar collector engines are not a new technology: the first working examples date back the year 1864, thanks to the experiments of August Mouchot, who later built the first engine as a truncated cone reflector [3]. The first solar power plant, built by Shuman in 1912, was kept operative for two years. During the 20th century, the technology underwent progressive improvements that lead to today's CSP plants.

2.1 Concentrated Solar Power – Facility Configuration

There exist different configurations of CSP systems, but all of them are characterized by some common features. The principle of work of CSP is the concentration of solar radiation by means of mirrors onto a surface, where heat is exchanged with a Heat-Transfer Fluid (HTF), the energy carrier. The fluid then undergoes a thermodynamic cycle that generates electricity. The characteristic components of each power plant are called **collector** and **receiver**. The collector is a series of mirrored surfaces pointing the sun, and it reflects the direct radiation on the receiver, a set of components that collect the radiation. The receiver increases its temperature, and transfers its energy to the HTF. This can happen directly or indirectly: in the second case, the zone that collects the energy from the receiver is called *primary circuit*; this zone then interacts with the *secondary circuit*, that consists in an enclosed zone where the HTF transports the energy. Tanks for energy storage can be adopted to generate electricity outside the sun-hours and stabilize production in case of variable demand.

The receiver is one of the most important components of any system, because it is where the technology makes the difference [4]: its elevated complexity, especially in the case of a solar tower system, can be responsible for a wide-ranging contribution to the global efficiency; if the receiver is well designed, the latter parameter can increase significantly. As said before, the thermodynamic cycle that follows is generally well-known, therefore comes with a limited room for improvement. The collector is a critical component as well, but not as challenging as the receiver due to a much lower complexity.

There are four principal configurations, illustrated in fig. 2.1: Parabolic Trough Collector (PTC), Linear Fresnel Reflector (LFR), Central Receiver System (CRS) and Parabolic Dish System (PDS). Except for the PDS technology, all the plants consist in a similar main configuration, apart from the collector-receiver system that is peculiar for each one of them. In fact, once the HTF has been heated, it undergoes a Rankine (or Brayton) cycle with appropriate alterations, depending on the technology used. The vapor expands in a turbine, then it condenses and finally it is pumped again into the heat exchanger. Both PTC and LFR are *linear concentrator systems*, i.e. the receiver has a linear-developed shape. CRS and PDS are, instead, *point concentrator systems*: solar rays are converged on a single focus point, located

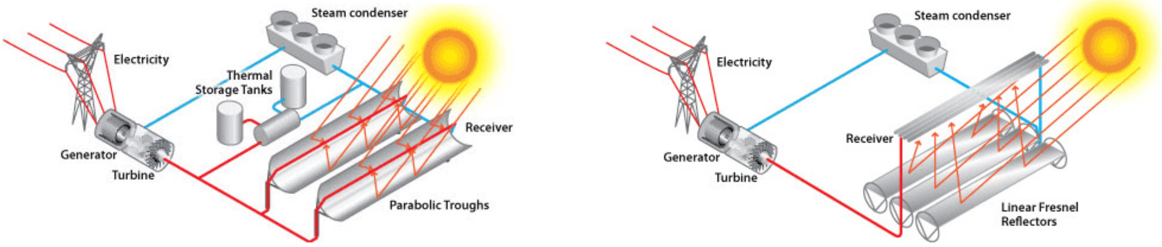

(a) Parabolic Trough Collector **(b)** Linear Fresnel Reflector

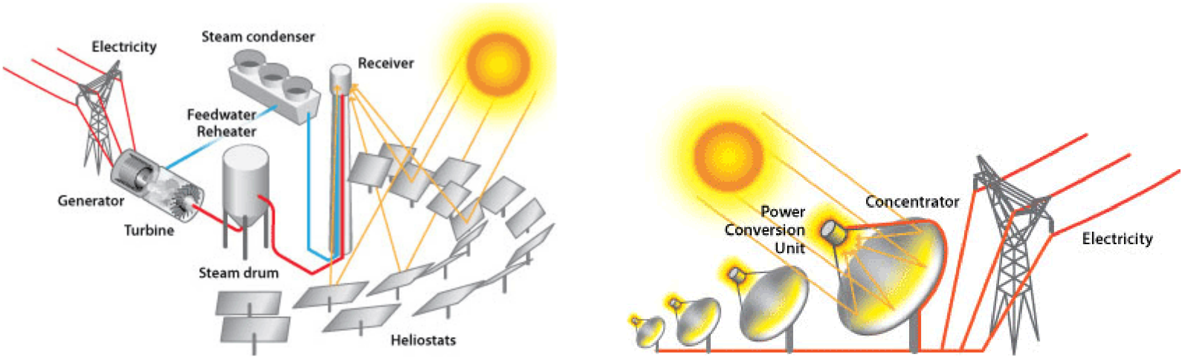

(c) Central Receiver System **(d)** Parabolic Dish System

Figure 2.1: Examples of the principal CSP configurations. Figures retrieved from Energy.gov (2013) [5–7].

where the receiver is fixed.

PTCs use a set of parabolic mirrors that focus the sun rays onto their relative receiver tube, as shown in fig. 2.1(a). The receiver consists in an absorber tube situated in the focal point of the parabola [8]. The mirrors follow the sun motion rotating on a single axis, usually north-south. PTC is the oldest CSP technology and therefore the most common and proven. It was occupying approximately the 82% of the global CSP installation in 2016 [9].

LFRs have a configuration similar to PTCs, as it is possible to see in fig. 2.1(b). The collector is made by several flat mirrors that recreate the geometry of a parabola in different planes: they in fact point rays to a common focus as the geometrical curve does. A major advantage of LFR over PTC is that the absorber is fixed and mirrors are flat, both being easier to manufacture and less expensive. A drawback that mirrors have is that they cannot recreate a perfect parabola, so they concentrate less energy per unit surface. However, they can be two-axis tracking, leading to an increment to the average radiation reflected per unit surface [8].

An example of CRS is shown in fig. 2.1(c). The collector of this plant is made of a series of flat (or slightly-curved) two-axes tracking mirrors called *heliostats*. Differently from the other configurations (including PDS), it points to a single receiver located on the top of a tower.

Parabolic dishes are point concentrators that use a parabolic mirror collector. When placed in series, they form a PDS, as shown by fig. 2.1(d). The mirror is a 3D paraboloid that focuses solar radiation onto its receiver, which contains a Stirling engine or a small gas turbine [10]. The receiver is fixed to the collector and they move in tandem around two axes. Electricity is produced separately in any receiver, so that the total installed power is the sum of the nominal power of every Engine. In 2013, the only operative plant was Maricopa Solar Project in Arizona, USA [8] (having started its activity in 2010).

2.2 State of The Art

The principal characteristics of the different plant configurations are resumed in tab. 2.1. CSP plants are characterized by a high level of technology used. On the one side, Rankine (or Brayton, or Stirling) cycles have been known for more than 100 years, and plants experienced innumerable adjustments in order to maximize the efficiency. On the other side, the receiver must combine high absorption of solar power and low heat losses. In conventional fossil-fueled plants, the zone where the highest temperature is reached is virtually detained from the ambient, because combustion occurs in an enclosed burner thermally insulated from the environment. In a CSP plant, the heat exchanger cannot be completely insulated, because it must permit the flux of energy coming from the outside (solar radiation). This is critical and can be accomplished only by designing the components with a high level of technology.

Table 2.1: Characteristics of the main CSP configurations (state of the art). The capacity range is relative to a single turbine. Data extracted from the International Renewable Energy Agency (IRENA) [11] and Xu et al. [9].

	Parabolic trough	Solar tower	Linear Fresnel	Dish-Stirling
Maturity of Technology	Commercially proven	Commercially proven	Early commericial projects	Demonstration projects
Capacity range [MW]	10-250	10-130	5-250	0.01-1
Operating temperature [°C]	350-400	250-565	250-350	550-750
Collector concentration [suns]	70-80	$>$1000	$>$60	up to 10000
Global efficiency [η]	0.1-0.16	0.1-0.22	0.8-0.12	0.16-0.29
Receiver/absorber	Moving with collector	Fixed	Fixed	Moving with collector
Power cycle	Steam Rankine, Organic Rankine	Steam Rankine	Steam Rankine, Organic Rankine	Stirling Engine, Steam Rankine
Storage with molten salt	Commercially available	Commercially available	Possible, but not proven	Probably, but not proven
Relative cost	Low	High	Low	Very high
Outlook for improvements	Limited	Very Significant	significant	High (through mass production)
Advantages	Mature technology, Modular units	High η, Compatible with Brayton cycle	Fixed, Low investment costs	High η, Modular units, Compatible with Brayton cycle
Disadvantages	Relatively low η	High O&M costs	Relatively low η	No thermal storage available, low maturity

The collector can represent a technological challenge as well, especially in the case of a parabolic dish technology: obtaining a close-to-perfect paraboloid is not an easy task for the manufacturing industry.

2.2.1 Heating fluid

The heating fluid (or the heating fluids, when a secondary circuit is present) has an important impact on the global efficiency of the plant. The thermodynamic properties of the fluid (conductivity, specific heat, liquid-steam transition temperature, viscosity ...) influence the heat transfer process. Air, for instance, is low-viscosity (which is an advantage, because the pumping energy needed is low) and cost-free, but it has low heat exchange rate, since it is a gas; up to 2015, the only plant using it (only as a primary HTF) was the *Jülich Solar Tower* in Germany [9]. Up to that date, water was being used in seven plants, among which world's largest (377 MW), *Ivanpah station* [12]; its only issues are its low conductivity and the scarcity in the arid regions where CSP is adopted. The technology used in steam Rankine cycle is well consolidated, making water HTFs a reliable choice. Thermal oils have been adopted in a few cases, but they come with many relevant issues such as the high cost and the limited temperature range in which they can operate (due to thermal degradation) [9]. Salt mixtures are an interesting alternative to steam/air because they have a much higher heat removal capability than water [13]. The most investigated molten salts are currently nitrites and nitrates, although many others have been proved. The temperature range of this HTF can be limited as well, although not as much as for thermal oils; moreover, it is important to remember that the difference between the maximum and minimum temperature achieved by the fluid depends on the type of power plant. Linear systems are only able to reach limited temperatures, that make molten salts a reasonable choice. Price can be as well a limitation for this technology. Research & Development (R&D) is investigating the use of metal as HTF, in order to reach higher temperatures than the molten salts limit [14]. Finally, the HTF choice must consider thermal energy storage, as explained in sec. 2.2.4.

2.2.2 Collector

R&D's main efforts regarding the collector are focused on the reflectance improvement of the mirrors. Mirror enhancements decrease the amount of needed reflecting surface. This is crucial, especially in solar tower systems, where heliostats can represent up to a half of the initial investment [15]. Heliostats are normally composed of a metal surface covered by a glass layer, sealed together to protect against moisture and avoid corrosion. Two typical metals used are silver and aluminum; the first has a higher reflectivity (0.95-0.97) compared to the second (0.88-0.92), but it is more expensive. The coating surface is normally made of glass because of its inert nature, low cost and physical strength. The combination of glass and silver gives the mirrors an overall reflectance that is currently of 0.93-0.94. A polymeric material is usually applied in order to increase the wind load resistance and avoid deformation. Metal/ glass mirrors are used also in PTC, LFR, and PDS. R&D is struggling to develop coatings made by polymeric films instead of glass because of their weight and optical properties. Polymers could represent an interesting alternative of glass especially in PTCs and PDSs, because they can be easily deformed.

Research is struggling to reduce the manufacturing cost of production of the mirrors, especially the parabolic-shaped. Regarding solar towers, There have been two trends regarding the size of the heliostats. Some manufacturers started increasing the surface-per-heliostat, in order to reduce components, and consequently O&M, and decrease the number of expensive trackers. This has lead to a surface per heliostat rising from $12\,\mathrm{m}^2$ in the 1970s up to the current 150 to $200\,\mathrm{m}^2$ [15]. The other trend has been the opposite, seeing some manufacturers reducing the area down to $1\,\mathrm{m}^2$, in order to exploit the benefits of mass production and simplify the drive mechanisms given minor wind loads on the mirrors. Smaller heliostats also imply a minor use of land, and therefore fewer energy dispersions due to the shorter distance from the tower [15]. Regarding parabolic troughs, dishes and linear Fresnel, the trend is to increase the mirrors' area, in order to reach higher temperatures.

Dust cleaning is another important process that has to be involved in any type of CSP plant, especially if located close to sand areas. Dust layers, in fact, decrease the reflectance of the mirrors, and therefore the energy that impacts on the receiver: efficiency can decrease up to the 70% if the surfaces are never cleaned throughout a year [9]. This problem is more difficult to treat in arid regions, where water access is expensive.

2.2.3 Receiver/Absorber

The receiver of a PTC is shown in fig. 2.2(a). The absorber tube consists of a highly-absorbing steel tube surrounded by a selective glass envelope separated by a vacuum (or air) zone [16]. This

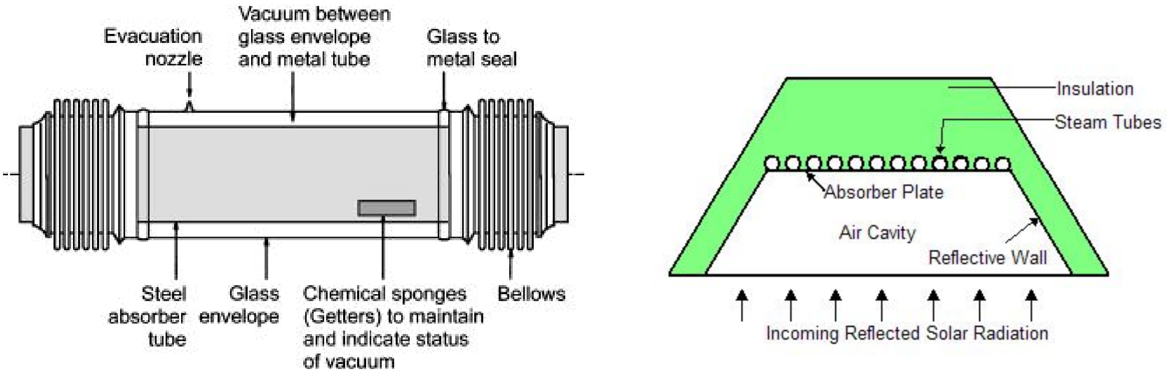

(a) Parabolic Trough Collector. Figure retrieved from Price et al. (2002) [16].

(b) Linear Fresnel Reflector. Figure retrieved from Wikipedia [17].

Figure 2.2: Heat collection element of a PTC and an LFR.

combination of materials with different optical properties is crucial: the outer glass is wavelength selective, and permits the solar radiation to enter, and be absorbed by the inner tube; at the same time, its selective nature blocks the thermal radiation of the tube. Moreover, the vacuum blocks the convective heat transfer between the two surfaces. Coating with a selective surface is usually performed on the absorbing tube, in order to guarantee the high absorptance of beam solar radiation and low emissivity at thermal radiation wavelengths. Luz International Ltd developed tubes that tested in 2002 characterized by a transmittance of the glass of 0.96, a solar absorptance of 0.95 and a thermal emittance at 300 °C of 0.15 [16]. These models are still a reference in PTC, and are being used in the Mojave Desert plant (operational in December 2014), which is one of the newest and largest PTC facilities in the world (250 MW).

LFR receivers consist of an inverted air cavity having an inner reflective surface that concentrates the solar radiation onto an absorber plate exchanging heat with ambient insulated tubes, as shown in fig. 2.2(b). LFR receivers differ for the geometry of the reflective surface (parabolic, trapezoidal, . . .), and the number of tubes [18]; the choice depends on the trade-off between cost and efficiency.

There are currently two main types of CRS receivers: tubular and volumetric [19]. In tubular receivers, the HTF flows inside a set of tubes that are heated by the focused solar radiation. There are two main types of tubular receivers. In the *external cylindrical receiver*, shown in fig. 2.3(a), the tubes are placed onto the inner part of an absorption surface that is exposed to atmosphere. In the *cavity receiver*, instead, the tubes are posed inside a cavity, as shown in fig. 2.3(b). Since the hot surface is

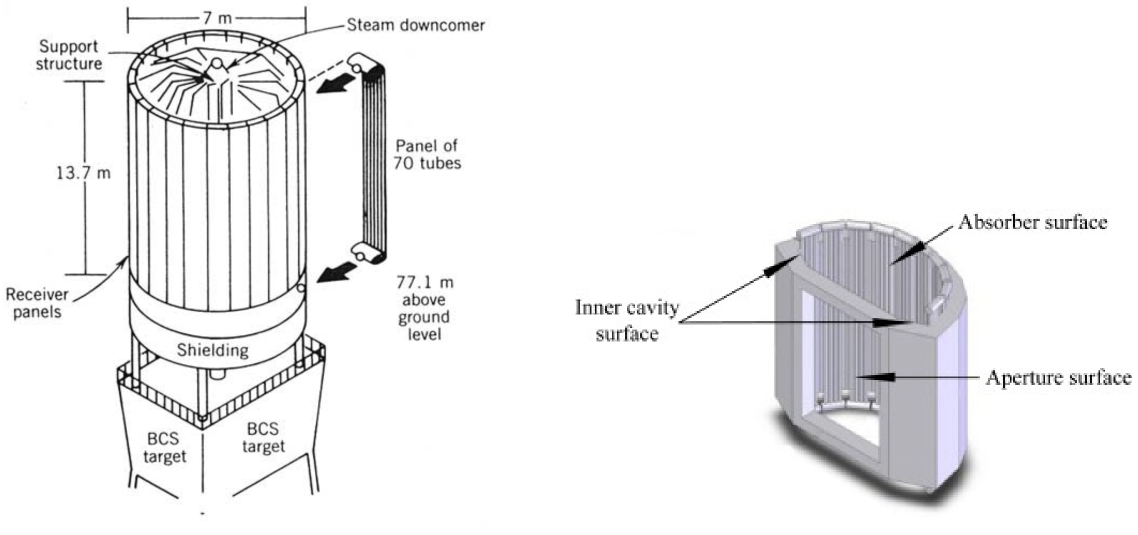

(a) External cylindrical receiver **(b)** Cavity receiver

Figure 2.3: Examples of the principal tubular receivers. In 2.3(a) the absorber surface is the external surface, while in 2.3(b) it is the internal surface. Figures retrieved from Zhang et al. (2015) [20] and Powerfromthesun.net [21].

not in direct contact with outer air, the convective and radiative heat losses are minor than in external receivers [19, 22]. Tubular receivers reach a thermal efficiency (i.e. the ratio of the energy absorbed by the HTF to the incoming solar energy) of $\eta_{th} = 0.8 \div 0.9$ [4]. R&D is focusing on reducing heat losses and local stresses on tubes. Also volumetric receivers have two main configurations: the *open volumetric receiver* and the *closed (or pressurized) volumetric receiver*. In the first case, shown in fig. 2.4(a), the receiver is divided in *primary* and *secondary circuit*. In the primary circuit, ambient air is sucked (usually thanks to a driving fan) and heated through the porous receiver. Then, an internal heat exchanger passes the energy of the hot air to another HTF flowing in the secondary circuit. Cooled air is then expelled. In the second case, shown in fig. 2.4(b), air is mechanically driven by a fan and follows an enclosed circuit. Hot air can be used directly in a Brayton cycle or cross a heat exchanger, releasing its energy to another HTF flowing in a secondary circuit. Volumetric heat receivers were demonstrated to be able to reach a thermal efficiency of $\eta_{th} = 0.89$ with a fluid outlet temperature of 700 °C [25]. However, volumetric receivers at such temperatures have been showing failures due to local overheating. Techniques to provide a more uniform heating are currently being inspected. The **Small Particle Air Receiver**, shown in fig. 2.5, is a particular type of volumetric receiver: designed in the 1970s, it uses a fluid containing micro-particles suspended in air [9]. These micro-particles help air absorb the sun radiation. Proven in theory a thermal efficiency up to 90% with an air temperature of 700 °C, current research is trying to create a physical prototype.

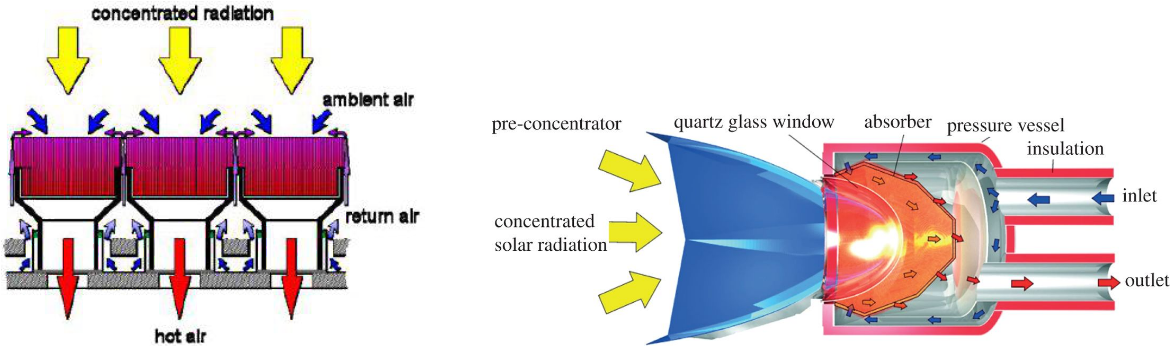

(a) Open volumetric receiver section

(b) Closed or pressurized volumetric receiver section

Figure 2.4: Examples of volumetric receivers. Figures retrieved from Prashant [23] and Muller-Steinhagen (2013) [24].

2.2.4 Thermal Energy Storage

Fig. 2.6 shows the two main configurations of a Thermal Energy Storage (TES) system. Energy storage is said to be **direct** if the fluid used to store energy is the one used to collect it, and **indirect** otherwise. The technology to be adopted depends on the HTF, that in its turn depends on the type of

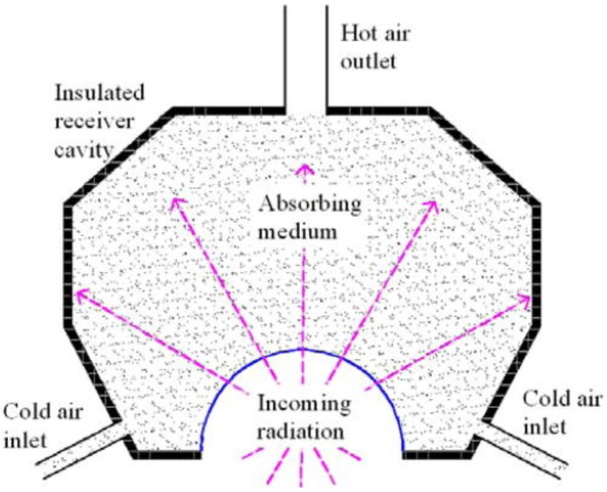

Figure 2.5: Section of a small particle air receiver. Figure retrieved from Kitzmiller & Miller (2011) [26].

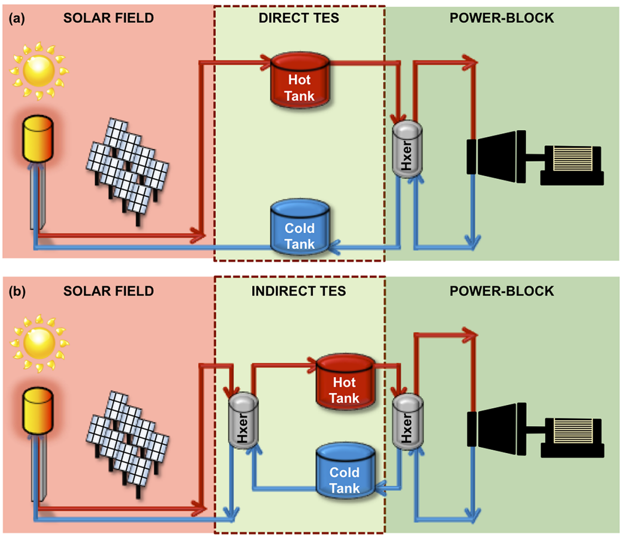

Figure 2.6: Direct and indirect TES for a CRS plant. Figure retrieved from Stekli, Irwin & Pitchumani (2013) [27].

plant. Indirect TES is less efficient because it implicates more process of energy transfer (and so more heat losses), but it permits to exploit the advantages of a substance with different properties (and cost) respect to the fluid undergoing the cycle.

Energy can be stored as *sensible heat*, *latent heat* or *thermo-chemical heat*. The first is based on internal energy variation due to temperature differences while the second due to phase change; the third, instead, is based on a thermo-chemical reaction that absorbs (charge) and releases (discharge) energy.

The main drawbacks of sensible heat storage are that it involves a low energy density and that it is difficult to release energy at a fixed temperature [28]. Solids as sensible TES have been studied, principally because of their high conductivity (that accelerates heat transfer), temperature range, and low cost. They include concrete, castable ceramics, graphite and silica sand. In case of solid TES, a configuration different from the two-tanks one can be used. It is called **Single-Tank Thermocline System** [29]: as fig. 2.7 shows, the fluid passes through a single tank that is maintained hot at the top and cold at the bottom. The region having a steep temperature difference is called **thermocline** and moves downwards when the tank is charged and upwards when it is discharged. The temperature gradient is maintained by the variation of the temperature of the fluid crossing the tank. Liquids, such as molten salts, are also used as sensible storage. Sometimes they contain encapsulated nanoparticles, that increase their energy density. One of the best-performing liquid used in TES is the solar salt, giving its low cost and elevated maximum temperature [31].

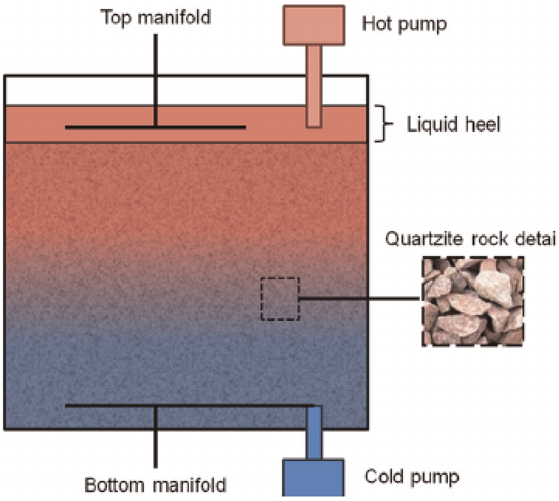

Figure 2.7: Example of a Single-Tank Thermocline System including quartzite rock bed. Figure retrieved from Flueckiger, Iverson, Garimella & Pacheco (2014) [30].

Latent energy storage is carried out with the use of Phase Change Materials (PCMs). Its strong advantage is that the heat exchange temperature is maintained constant during the whole process. Energy density is higher compared to sensible storage materials, but PCMs have a low thermal conductivity. For such reason, these materials can be "doped" with graphite or metal alloys, so that their conductivity is raised.

Thermo-chemical heat storage is based on reversible chemical reactions. Its great advantage is that the energy density can be up to 10 times larger than in the materials used latent energy storage. Moreover, the products of the storing reaction are kept at ambient temperature, therefore heat losses are minimized. However, they are also characterized by a low conductivity. Another drawback is that the reactions are usually not completely reversible, and their storage capability decreases in time.

2.3 Economic perspectives of CSP

The electricity market has been rapidly evolving in the last few years, mainly because of three causes: the significant increase of renewable energy share in the electricity market, the economic growth in developing countries, and the changes in the price of the energy commodities. The current situation has been created by the interaction and the balance of these three causes. The *Electricity Information Overview* of the International Energy Agency (IEA) shows the current trends in electricity generation [32]. Electricity production in OECD countries substantially halted from the amount it reached a decade ago, as shown in fig. 2.8. This happened because of the economic crisis that affected nearly any country in the beginning, and because of an increase of the energy efficiency that accelerated with the economic recovery. On the other hand, electricity production in non-OECD countries kept on rising at a high rate.

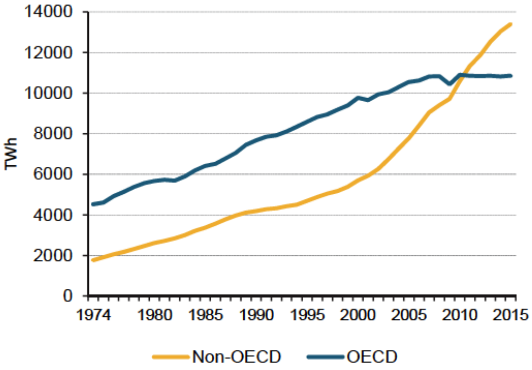

Figure 2.8: Total Electricity Production of OECD and non-OECD countries from 1974 to 2015, International Energy Agency [32].

Although the electricity production did not vary in OECD countries recently, the energy mix saw important changes in this period, as fig. 2.9(a) reports. Coal fell sharply, whereas natural gas and non-

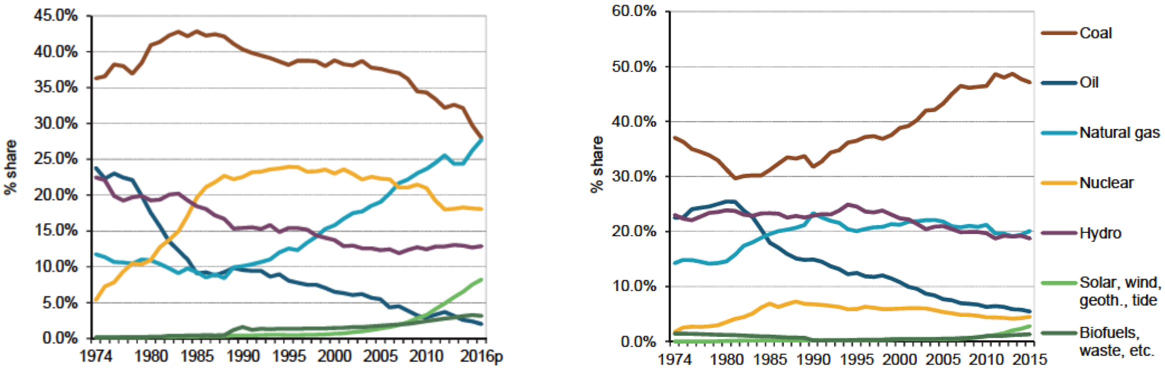

(a) OECD countries

(b) non-OECD countries

Figure 2.9: World electricity generation mix sources – International Energy agency [32].

hydro renewables more than doubled their share. The rise of the natural gas use commenced with the shale gas revolution (principally in the US, the most influential country in OECD) and continued with the fall of the gas price [33]. This shift towards natural gas was the principal cause of the diminishing use of coal: once the first became more competitive, the second lost its attractiveness. In non-OECD countries, however, this shift has not occurred yet, partly because shale-gas extraction needs a high level of technology and highly-skilled employees.

Renewable energies, instead, improved their share both in OECD and non-OECD countries, due to technology enhancements and because of more favorable policies. In fact, many governments started subsidizing clean energy and promoted it directly in order to fulfill international agreements. Although such policies were mainly issued in developed countries, lately they have started being promulgated in developing countries as well. At the 2015 United Nations Climate Change Conference in Paris (COP21), in particular, the majority of the countries signed a deal to advocate clean energy and promise to reduce carbon emissions (in order to maintain the global temperature increase below $2\,°\mathrm{C}$ higher than the pre-industrial levels). This agreement, if respected, is going to push further the adoption of renewable energy for electricity production. It is important to notice that coal already reached its maximum point also in non-OECD countries, and before the agreement of Paris.

Future trends of the power sector have been depicted in IEA's World Energy Outlook (2015) [34], published before the ratification of the Paris agreement. Looking toward 2040:

- electricity demand and installed power are expected to increase by more than 70% from 2015 levels, mostly because of non-OECD countries, led by China and India.
- coal share will fall by 11%, low-carbon technologies share will rise by 13% due to non-hydro renewables. In OECD countries, coal share will halve.

Projections taking the Paris agreement into account, in the same report, expected that electricity generation from non-hydro renewables will grow globally from the $1316\,\mathrm{TWh}$ of 2013 to the $10\,980\,\mathrm{TWh}$ of 2040.[1] The report shows the growth potential of the various renewables consequent to the Paris agreement. Data have been extracted and plotted to be visualized in fig. 2.10. CSP is the technology that is going to have the largest increase proportioned to the current exploitation: the electricity it will generate is expected to be about 200 times higher than nowadays, an average growth of 21% of the provided energy. The largest absolute increase will be instead seen by wind energy, with a production rising about

---

[1] These projections did not consider the withdrawal of the United States from the agreement under the Trump administration. However, it is still difficult to assess the impact of this decision, because:

- it is not expected to be integrally rejected, but only renegotiated (as many Republicans expressed this will)
- it will not take effect until the next five years, which include another round of general elections
- it will not ban the US from promoting green policies, but just free them from the pledge they had signed
- the United States is just a single country among 160 that have signed the agreement

Many columnists think that the resignation will eventually have only little impact [35], [36]. Renewables are therefore set to represent a major player in electricity generation in the next decades, both in developed and developing countries.

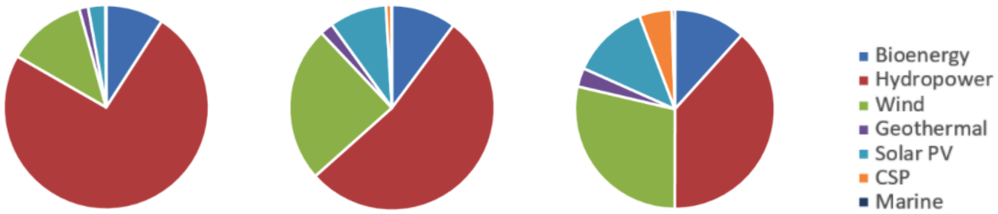

(a) 2013 data **(b)** 2025 forecast **(c)** 2040 forecast

Figure 2.10: World present consumption and forecast of electricity generated by renewable sources. Data shown in tab 2.2. – World Energy Outlook, International Energy Agency (2015) [34].

Table 2.2: World renewable consumption scenario – International Energy Agency.

	2013	2025	2040
Bioenergy	464	973	2077
Hydropower	3789	5083	6836
Wind	635	2344	5101
Geothermal	72	197	541
Solar PV	139	862	2232
CSP	5	83	937
Marine	1	7	93
Electricity generation [TWh]	5105	9549	17 817

4500 TWh. Solar PV will surpass bioenergy, and hydropower will lose its dominant nature (although it will continue to have the largest share). In any case, by 2040 the electricity mix is set to become more plural, having different technologies coexisting. CSP seems to have the highest potential in terms of growth. The next paragraph will try to assess it focusing on this particular technology and evaluating its advantages in comparison to the others.

2.3.1 CSP future trends

CSP operating plants are shown in fig. 2.11. The majority of the installed power is located in Spain and United States, that represent together almost half of the global market. It can be noticed that neither of the countries is building or developing new plants. This is a consequence of the energy policies of the two countries. The United States concluded its Investment Tax Credit (ITC), a tax credit of 30% on renewable energies, and new projects halted in 2014. Spain, on the other side, retroactively reduced its Favorable Feed-in Tariff (FIT) on solar technologies, not only damaging current businesses, but also increasing regulatory uncertainty and the risk of investment. The result is that no added capacity is being planned in these two countries [38].

In addition to the incentives, one of the reasons why Spain and the US are the countries that have more installed power is that, among the developed countries, they have one of the highest Direct Normal Irradiance (DNI), as shown in the in fig. 2.12. DNI is an indirect indicator of the global potential for CSP.

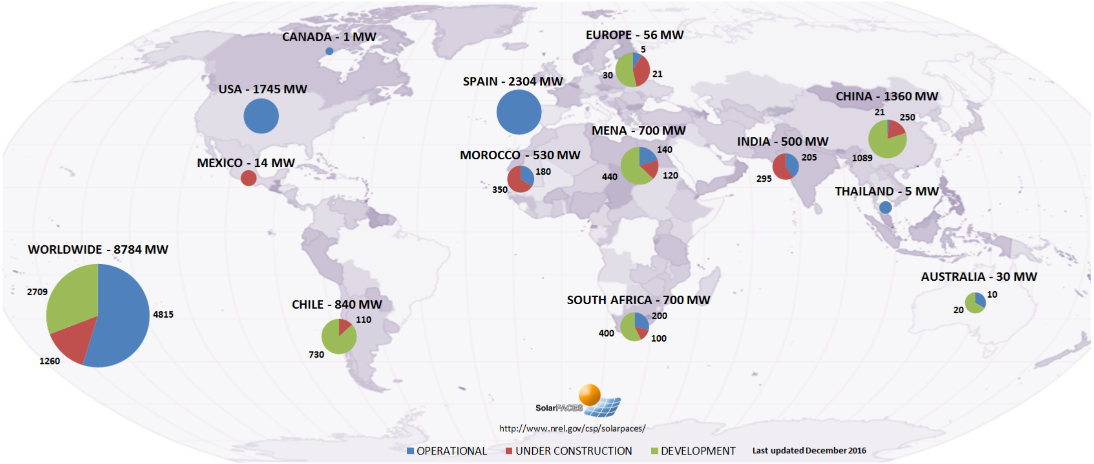

Figure 2.11: CSP projects: installed, under construction and under development total nominal power. Figure retrieved from HELIOSCSP [37].

The irradiation in the two countries is among the highest, especially among the developed countries. Therefore, Spain and United States started investing in R&D creating a business that is becoming more and more profitable also in countries under development. Now that the technology is becoming more mature, countries such as Chile, South Africa and China started investing relevantly on the technology, according to fig. 2.11. DNI is high also in many other regions in the world, as Australia, Mexico, Argentina, North Africa and The Middle East, where the possibility of growth of CSP there is high. The reason why the investment in Australia is still low in this technology despite being a developed country and despite its potential is a consequence of the regulatory structure for the development of renewables in the country. In fact, both at a local and at a federal level, Australia's delays in project approvals, frag-

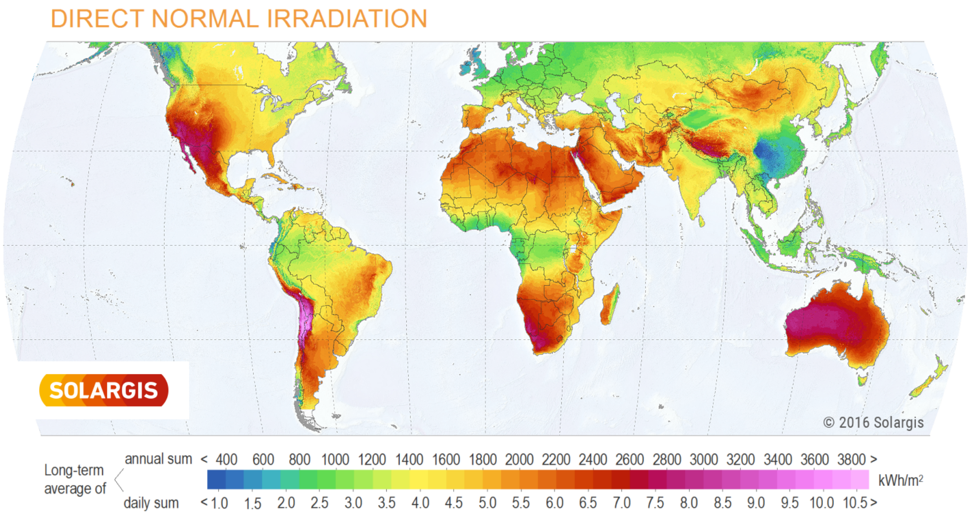

Figure 2.12: Global Direct Normal Irradiation – DNI Solar Map © 2016 Solargis [39].

mented regulation, insufficient incentives and continuous legislative redefinitions have posed significant barriers to clean electricity generation [40]. As a result, the exploitation of solar resources accounted only for a 3% of the energy generation in 2016 [41]. With a change in the country legislation toward renewable electricity production, CSP installed power could eventually start growing. The other countries that have a large DNI are still under development, but could already enter the CSP market following China, Chile and South Africa, now that the technology is becoming more and more profitable.

It must be said, however, that the countries that have the highest level of irradiance are also the ones where the use of photovoltaic energy is the most performing. The great advantage of solar PV over Concentrating Solar Power is that the former has undergone a huge cost reduction since it has been commercialized. According to the Economist, the price of crystalline silicon photovoltaic cells reduced 100 times from $76.67\,\$/\mathrm{W}$ in 1977 to $0.74\,\$/\mathrm{W}$ in 2013 [42]; currently, the price is about $0.22\,\$/\mathrm{W}$ [43] for polycrystalline cells. The huge price reduction was the eventual consequence of a large investment in R&D, due to the interest of companies attracted by the versatility of photovoltaic panels in comparison to the traditional energy system. Not being able to be commercialized as widely as PV systems, CSP projects gathered a minor interest, and their price did not reduce likewise. Levelized Cost Of Electricity (LCOE) is an important indicator to assess the profitability of electricity technologies and can be used to compare solar PV with Concentrating Solar Power. It represents the cost per energy actualized to the time of the initial investment.

$$LCOE = \frac{\text{sum of the costs over lifetime}}{\text{sum of electrical energy produced over lifetime}}$$

In 2016 Lazard made an interesting estimation of the unsubsidized LCOE in the United States, a reference country regarding R&D advancement [44]. The results have been reported in fig. 2.13. Regarding

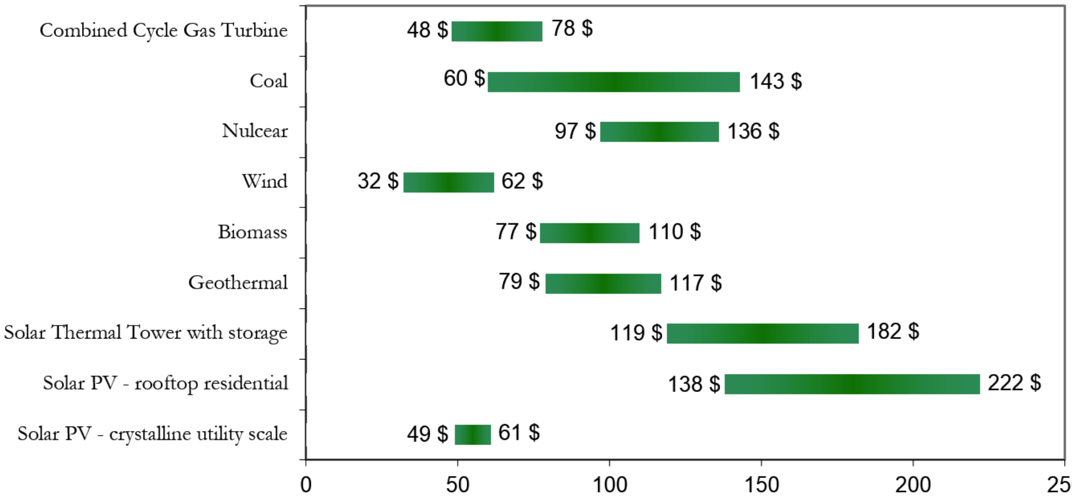

Figure 2.13: Unsubsidized LCOE ($/MWh) for the principal electricity sources. Data retrieved from Lazard (2016) [44].

CSP, the central receiver plant is considered, since it is nowadays the most profitable amongst the four technologies. The convenience in the price of photovoltaic energy (at utility scale) over CRS is unquestionable: the worst plant's LCOE is still half of the best CSP plant. CSP's costs are also higher than the majority of the other technologies. This makes clear that, at least nowadays, CSP cannot compete with them. However, solar thermal energy is not excessively more expensive than coal and nuclear energy. As Lazard points out, if coupled with an 18h thermal storage CSP can reach a LCOE 119 $/MWh that is competitive with some nuclear and coal facilities. If Concentrating Solar Power succeeds in becoming more and more inexpensive, it will be likely to reach a significantly larger market share, in line with the World Energy Outlook predictions. There are several reasons why we should expect that this eventually happens. The SunShot Initiative is a national program launched in 2012 by the U.S. Department of Energy in charge of outlining solar energy goals and track them. In 2016 they assessed that the 2020 goal of LCOE reduction that they had previously fixed was achieved at a 70% extent [38], and confirmed that the results were in line with the predictions. According to the study, the main technology improvements that could drive the costs downwards are:

- The achievement of high temperatures as a consequence of the improvement of the receiver technology. High temperatures would permit the exploitation of supercritical cycles (as air in a Brayton or Combined Cycle Gas Turbine (CCGT) cycle), resulting in a sharp enhancement of the cycle efficiency.
- Higher temperatures could be reached also using solar-selective coating, having a high absorptance but low emittance at thermal frequencies and vice versa at solar spectrum frequencies.
- The use of technological equipment to align accurately the heliostats and improve the focusing.
- The progress in Thermochemical Energy Storage and Latent Energy Storage, in the form of an increased efficiency and a cheaper manufacturing.
- A larger market, involving a larger economy of scale.
- Larger plants, resulting in a lower O&M.

In parallel with this betterments, it is crucial for CSP to increase its annual performance improving the dispatchability. In fact, the main costs of such a plant are the investment costs: with a more intense use, these costs would be amortized over a larger energy production; in such a way, the LCOE would decrease notably. This is the reason why TES is so important that it is always taken for granted to be a part of the future technologies. Although Sunshot defines the 2020 objectives both for PTCs and CRSs, it recognizes a 15% lower LCOE in the solar tower. The latter, according to the report, should reach a value of 59 $/MWh. At such levels, it would be competitive with the all the current technologies showed previously at fig. 2.13. This is a proof of what was before mentioned: with a successful technology development, CSP could become competitive with the other power technologies.

In any case, solar thermal energy should not only be compared to the others by the point of view of the cost. Renewables are characterized by many differences in the way they produce energy. Factors as predictability, reliability, and adaptability to the demand play a crucial rule and differentiate them from each other. One great advantage of Concentrating Solar Power, differently from photovoltaic and wind technologies, is that it is dispatchable. This means that electricity can be provided depending on the demand, and not only when the conditions are favorable. Wind availability can vary a lot depending on the weather conditions, and at a certain rate also solar PV production is susceptible to the atmospheric conditions. Whenever the direct radiation on the panels is reduced (e.g. when a cloud interposes between the modules and the sun), the power output of the plant decreases, causing a brusque reduction of the electricity sent to the grid. In a CSP plant with TES this does not happen. The reliability of electricity production is a value that the energy market recognizes, since stabilization of the grid has a cost. Moreover, CSP electricity generation is able to ramp quickly, and can help to maintain the grid stability when needed.

Even though solar thermal plants are more costly than PV, the thermal storage gives them a useful asset: the possibility of accumulating energy during the day and selling it in the late afternoon. From the economical point of view this is a great advantage, since in those hours the price is the highest of the whole day. At that time, the use of fossil fuel plants is high. Whenever solar thermal electricity is generated in that period, the carbon emissions are drastically cut. Therefore, CSP could represent an asset to reduce CO_2 emissions (and help the country respect the clean energy agreements, perhaps avoiding possible economic sanctions).

It is possible to conclude, then, that although CSP is not currently competitive with fossil fuels or renewable power plants without economic incentives, it could become an important asset in a short future. Investing in R&D could provide technological ameliorations to the plant and make it preferable to others, and this is the reason why it is forecast to expand considerably. Although many research programs finance study on the four plant configurations, the CRS currently represent the most promising technology.

Its adoption as a part of the electricity generation mix of a country could improve its renewable energy share, following the clean transition that they prearranged for themselves. The countries that would gain more from this technologies are the ones that lie on the regions with the highest DNI; most of the times, they are the same that are rapidly developing now, and that will be responsible for the largest increment of the world electricity generation.

2.4 Central Receiver Plant – Background

Every day, a huge amount of solar energy hits the Earth. In the aridest regions of Chile close to the equator, the energy of the sun rays that hits the Earth's surface in one year can be 2.5 times larger than the average amount of energy that hits an equal area in Europe. In all the solar power technologies this energy is captured and converted to electricity. However, both in solar PV and CSP during the conversion process a certain amount of energy is lost and released to the ambient. In particular, in CSP plants the energy is first reflected, then pointed to a region where it is passed to a fluid, subsequently extracted from the fluid by a turbine and finally it is transformed to electricity in an AC generator.

This section will provide an overview of the processes that are involved in a Central Receiver System from the incidence on the collector to the absorption in the receiver. This will permit to understand the first energy-transfer processes that take place in a CSP plant, and give a background analysis to perform further calculations at a later stage.

2.4.1 Solar Radiation

The Sun is a giant mass that releases a huge amount of energy every instant. Its effective blackbody temperature is $5777\,\mathrm{K}$, and it is defined as the temperature that would have a *blackbody* if it radiated the same amount of energy. Solar radiation is released homogeneously to any direction. Solar energy is conserved, but the more it travels away from the Sun, the more it distributes to a larger area. For this reason, the energy approaching the Earth is not constant; in fact the distance between the Sun and the Earth depending on the moment during the year. The mean Earth-Sun distance is called astronomical unit, and it measures around 1.5×10^{11} m. When the Earth is located at such distance, the solar energy per unit time on a unit surface normal to the sun rays outside the Earth's atmosphere is called **solar constant** $G_{sc} = 1367\,\mathrm{W/m^2}$. The solar power outside Earth's atmosphere is referred as **extraterrestrial radiation** G_{on} [45].

On the path to reach the terrestrial surface, this energy is partly reflected, partly scattered and partly absorbed by the atmosphere. In fact, the substances that constitute its various layers are not perfectly transparent and interact with the solar radiation. Fig. 2.14(a) shows the effect of the atmosphere on the sun rays. The smaller area defined by the green line represents the total amount of solar radiation that arrives at the Earth surface. Once it has crossed the atmosphere, solar radiation is made by two main components: **direct** (or beam) radiation and **diffuse** radiation. The former is the amount of radiation that directly travels from the sun to earth without having any interaction, thus maintaining its direction. The latter is the amount of solar radiation that has been scattered from particles in the air and therefore deviated from its original direction. The ratio of direct to diffuse radiation is not fixed, and depends strongly on the weather, as well as other air conditions (such as pollution, that has an important

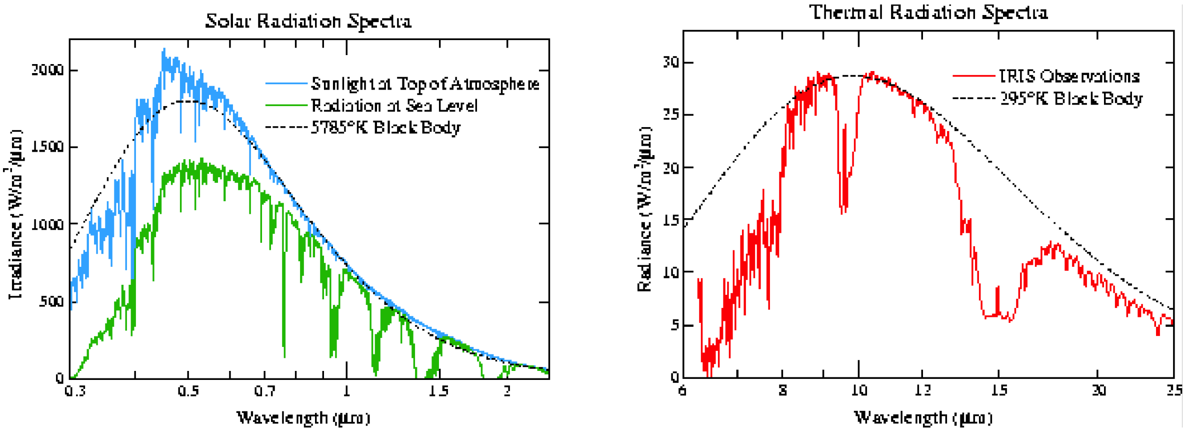

(a) Solar radiation

(b) Earth thermal radiation

Figure 2.14: Solar and Earth radiation spectra and comparison with a black body having the same global radiation. Figure retrieved from Hansen [46].

influence). In sunny days the direct radiation is far greater than the diffuse, while in cloudy days diffuse can become virtually the only component.

CRS plants (and in general all CSP plants) can only concentrate direct radiation, since the random direction of diffuse radiation does not permit it to be pointed to the receiver. This is the reason why such plants must operate on arid regions, where the amount of cloudy days is the lowest. In such days, the plants cannot be operative unless they had previously stored heat. The direct normal radiation intensity on a clear-sky day (which is the typical operative condition for a CSP plant) depends on extraterrestrial radiation, sun coordinates and climatic conditions, depending on the model used: in Appendix A the Hottel model is shown [45]. The time integration of the direct normal radiation gives the DNI.

2.4.2 Solar radiation losses

In order to calculate a CSP plant efficiency, it is important to define an incoming thermal power. In such plants, the direct normal radiation is selected. A significant amount of solar radiation is lost before being absorbed by the HTF. The main energy losses are:

cosine effect losses due to the relative inclination of the mirror respect to the sun;

heliostat absorption losses due to the limited reflectivity of the mirror;

atmospheric attenuation losses due to the interaction with air after the reflection;

shading/blocking losses due to the effect of shading or blocking of a mirror to another;

spillage losses due to the imperfect pointing on the receiver surface;

receiver reflection losses due to the limited absorptance of the receiver;

conduction losses due to heat conduction towards other elements of the tower from the receiver;

convection losses due to natural or forced air convection on the receiver;

radiation losses due to thermal radiation of the receiver.

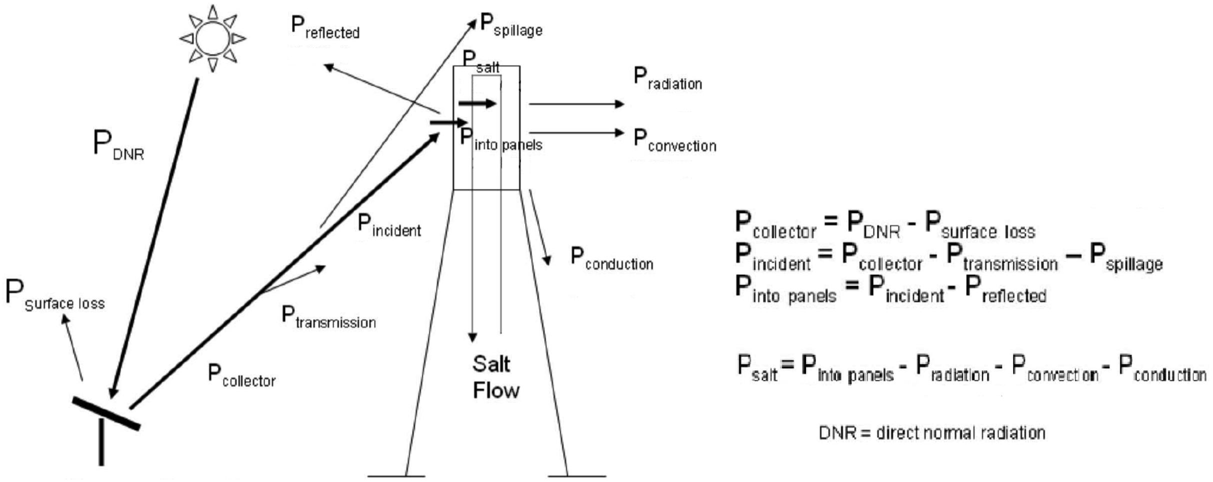

Figure 2.15: Principal losses of solar power from the incidence on the heliostats to the absorption by the HTF and relative thermal power balance. Figure edited from Lata, Rodríguez & de Lara (2008) [47].

The useful heat is the difference between the incoming heat and the sum of the losses, as shown in fig. 2.15. These losses can be separated in two main groups: the ones due to cosine effect, heliostat absorption, atmospheric attenuation, shading & blocking and spillage can be associated to the collector, while the ones due to receiver reflection, conduction, convection and radiation can be related to the receiver. By separating these two groups, it is also possible to define two relative efficiencies: the efficiency related to the collector, known as the **optical efficiency** η_{opt}, and the efficiency related to the receiver, known as the **thermal efficiency** η_{th}.

2.4.2.A Collector losses

All the collector losses are radiation losses, in the sense that a portion of solar radiation loses its path to the receiver. The model used to calculate the losses due to atmospheric attenuation is taken by the publication Cardemil, Starke, Scariot, Grams & Colle (2014) [48]. The model used to calculate spillage losses is extracted from the work of Schmitz, Schwarzbözl, Buck & Pitz-Paal (2006) [49].

The first loss that occurs is due to the **cosine effect**, graphically explained in fig. 2.16. The **angle of incidence** θ represents the angle between the sunbeams and the direction normal to the surface. The effective area of the solar radiation is the one perpendicular to the sun rays direction; in fact, if the heliostat is not oriented towards the sun, the same amount of energy is distributed on a larger area. Although heliostats A and B are the same, their effective area is different, as shown in the figure.

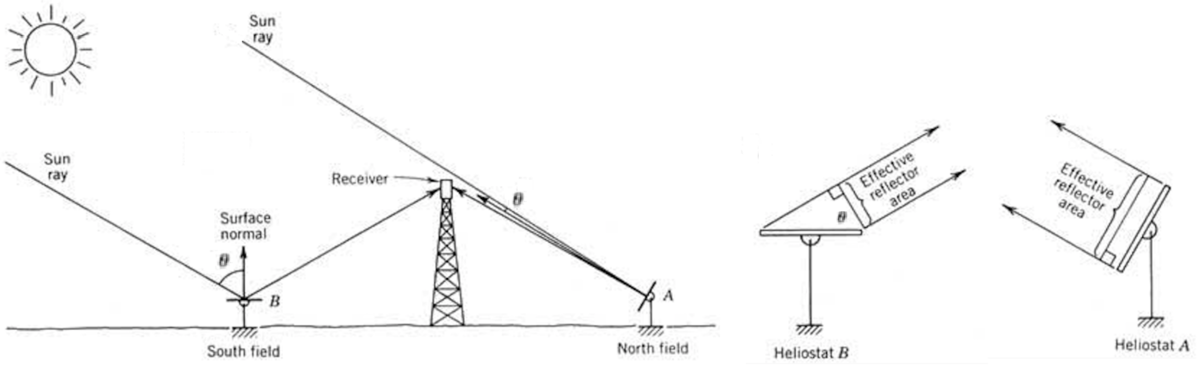

Figure 2.16: Dependence of the effective area on the angle of incidence between the sun and the heliostats (cosine effect). Figure edited from Powerfromthesun.net [21].

Therefore, the projection of the area makes the effective solar radiation equal to

$$G_{bt} = G_{bn} \, \cos\theta \tag{2.1}$$

where G_{bn} is the beam normal radiation and G_{bt} is the beam radiation on the tilted surface. The calculation of G_{bn} from G_{on} is explained in appendix A. To determine the orientation of the mirror, it must be imposed that normal of the heliostat surface is the bisector of the vectors pointing to the receiver and to the sun from the heliostat center. Given the vector pointing to the sun from the mirror $\mathbf{n}_s$ and the mirror normal to the surface $\mathbf{n}_c$, it is easy to note that

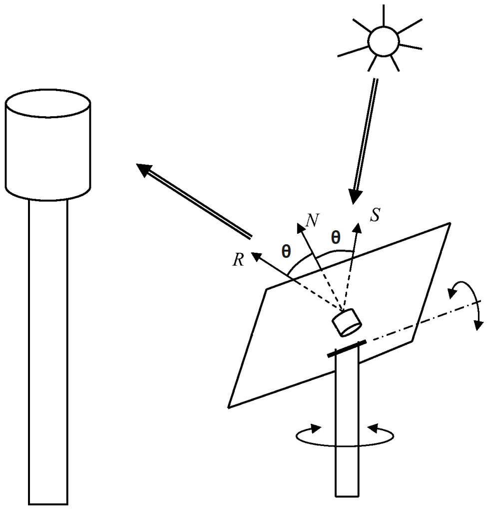

Figure 2.17: Heliostat orientation respect to the sun and the receiver location. Figure edited from Reznik (2009) [50].

$$\mathbf{n}_s \cdot \mathbf{n}_c = \cos\theta = \eta_{cos} \tag{2.2}$$

The cosine efficiency η_{cos} can be defined to factor in the cosine effect losses.

Once the radiation hits the heliostat it is largely reflected, but a part is absorbed by the mirror. The **reflectivity loss** in CSP plants has been described in sec. 2.2.2; typical values of reflectivity ρ_h are about 0.93-0.94 for clean mirrors. The efficiency η_{ref} related to the reflectivity losses is

$$\eta_{ref} = \rho_h \tag{2.3}$$

Part of the solar radiation can be blocked. Relatively to a specific mirror, if solar beams are obstructed before hitting it the phenomenon is called **shading**, whereas if it occurs afterward it is named **blocking**. Fig. 2.18 provides a graphical explanation. Projecting the area of a mirror along the beam direction and along the receiver direction, it is possible to compute respectively the shaded and the blocked area relative to that mirror. A blocking and shading efficiency η_{bs} can be defined as

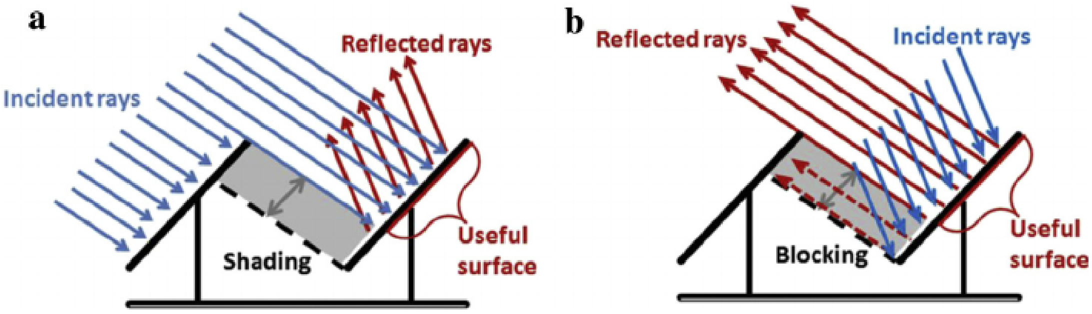

Figure 2.18: Blocking and shading effects on the useful surface. Figure retrieved from Montes, Rubbia, Abbas & Martínez-Val (2014) [51].

$$\eta_{bs} = 1 - \frac{\text{blocked and shaded surface}}{\text{total surface}} \tag{2.4}$$

Although it is possible to distinguish the effects of blocking and shading to a single mirror, eq. 2.4 refers to the total area of the system of heliostats. Shading and blocking can be predicted knowing the sun coordinates, the heliostats field and the tower disposition, and the dimensions of the mirrors.

On the path to the receiver, sunbeams are affected by **atmosphere attenuation**. There are several models that attempt to describe it. The one presented below is the Pitman and Vant-Hull transmittance model. The following equations are needed to calculate the atmosphere transmittance τ_{atm}:

$$\tau_{atm} = e^{-\xi\, R^S} \tag{2.5a}$$

$$\xi = C\, e^{-A H_T} \tag{2.5b}$$

$$1 - S = S_0\ (\beta + 0.0091)^{-1/2} \tag{2.5c}$$

$$\beta = 3.912/V_R \tag{2.5d}$$

$$C = C_0\ (\beta - 0.0037)^S \tag{2.5e}$$

$$A = A_0\ \ln\left((\beta + 0.0003\, \rho_w)\,/0.00455\right) \tag{2.5f}$$

$$C_0 = 0.0105\, \rho_w + 0.724 \tag{2.5g}$$

$$S_0 = 0.00101\, \rho_w + 0.0507 \tag{2.5h}$$

$$A_0 = 0.0112\, H_s + 0.0822 \tag{2.5i}$$

where ξ is the broadband extinction coefficient averaged over all wavelengths of the solar spectrum, R is the slant range (the distance between the heliostat and the focal point), H_s is the site elevation, ρ_w is the vapor concentration of air, V_R is the visibility range, β is the scattering coefficient, H_T is the tower focal height and A_0, C_0 and S_0 are altitude and water vapor-dependent proportionality constants. An atmospheric attenuation efficiency η_{atm} can be defined, equal to the air transmittance.

The last energy loss phenomenon involved between collector and receiver is the **spillage**. The solar radiation focused onto the receiver undergoes a little dispersion due to the imperfect calibration of the beam reflected direction. The dispersion is assumed to be probabilistic and aleatory, therefore it is distributed as a Gaussian function. The function standard deviation can be assumed to be

$$\sigma_{tot} = \sqrt{\sigma_{sun}^2 + \sigma_s^2 + (2\, \sigma_t)^2} \tag{2.6}$$

where σ_{sun} is the the sunshape error (that can be taken as 2.09 mrad independently of the DNI), σ_s is the surface error and σ_t is the tracking error. The spillage efficiency η_{spil} can be defined as

$$\eta_{spil} = \frac{1}{2\pi \cdot \sigma_{tot}^2} \int_x \int_y e^{-\frac{x^2+y^2}{2\, \sigma_{tot}^2}}\, dy\, dx \tag{2.7}$$

and represents the portion of the 3D curve that is located inside the receiver area. Spillage losses are defined globally for the whole system.

The combined effect of all the solar radiation losses makes it possible to define the optical efficiency.[2]

$$\eta_{opt} = \eta_{cos}\, \eta_{ref}\, \eta_{bs}\, \eta_{atm}\, \eta_{spil} \tag{2.8}$$

---

[2] In eq. 2.8, η_{cos} and η_{atm} are the global cosine effect efficiency and the global atmospheric attenuation efficiency, that factor in every heliostat of the field.

2.4.2.B Receiver losses

After losing part of its intensity, the total solar radiation reaches the receiver. The total heat incident on the receiver is referred as $\dot{Q}_{in}$. The thermal efficiency of the receiver η_{th} is defined as

$$\eta_{th} = \frac{\dot{Q}_{in} - \dot{Q}_{lost}}{\dot{Q}_{in}} = \frac{\dot{Q}_{in} - \dot{Q}_{ref} - \dot{Q}_{cond} - \dot{Q}_{conv} - \dot{Q}_{rad}}{\dot{Q}_{in}} \tag{2.9}$$

The first radiation loss after the sun rays hit the receiver is the **absorption loss**, due to the partial reflection of the receiver. The total amount of reflected radiation is the sum of the radiation that is reflected at any point of the receiver (inside or on the external surface) and that is eventually expelled. The rest of the energy gets trapped, and it is then absorbed. The absorptance of the receiver α_r can be defined as the fraction of the absorbed radiation over the total radiation, while the reflectivity ρ_r is the ratio of the reflected radiation to the total radiation. Consequently, the total heat absorbed by the receiver is

$$\dot{Q}_{rec} = \alpha_r \, \dot{Q}_{in} = (1 - \rho_r) \, \dot{Q}_{in} = \dot{Q}_{in} - \dot{Q}_{ref} \tag{2.10}$$

Part of the absorbed energy contributes to heat up the receiver solid components; the receiver transfer heat to the other solid parts of the tower through heat **conduction**. This amount of energy is not passed to the HTF, thus it gets lost. The amount of energy that gets lost for conduction is significantly lower compared to the other losses, so it can be neglected [47].

The high temperature of the receiver causes energy losses by **convection**. Heat convection depends on the temperature of the receiver T_r, the ambient temperature T_{amb} and the heat transfer coefficient h.

$$\dot{Q}_{conv} = h \, (T_r - T_{amb}) \, A_r \tag{2.11}$$

A convection losses model to evaluate the heat transfer coefficient in CRS receivers was developed by Siebers & Kraabel (1984) [52]. The model has two main assumptions: the temperature of the receiver and the convective heat transfer coefficient $\bar{h}$ are considered to be constant and equal to the average value around the receiver surface. These assumptions do not verify in reality, because the receiver is characterized by steep temperature gradients, both along its surface and along the outer layer of air. However, this simplified model can be used to supply a first quantitative description of the convective losses. The formulas shown below are referred to a cylindrical external-type receiver. Thermal convection between the receiver and the ambient can occur in as different forms: **forced convection** and **natural convection**. The first occurs when the wind is blowing onto the receiver, transporting the heat through the air; the second occurs in no-wind conditions, when the air motion is caused by the buoyancy forces created by its thermal gradient. In a more general case, the heat transfer coefficient depends on the combination of these two phenomena. This model combines the heat transfer coefficient due to forced convection $\bar{h}_f$ and the heat transfer coefficient due to natural convection $\bar{h}_n$.

$$\bar{h} = \left(\bar{h}_f^{3.2} + \bar{h}_n^{3.2}\right)^{1/3.2} \tag{2.12}$$

To calculate the first of the two terms, a correlation of forced convection of a cross-flow on a cylinder with pyramidal shaped roughness elements (that recreate the tubes of the receiver cylinder) is used. The Nusselt number related to this configuration depends on the surface roughness k_s/D; the equation presented belows refers to the case $k_s = 200 \cdot 10^{-5}$.

$$\begin{aligned} Re_D &\leq 4.1 \cdot 10^5 & Nu_D &= 0.3 + 0.488\, Re_D^{0.5} \left(1 + \left(Re_D/282000\right)^{0.625}\right)^{0.8} \\ 4.1 \cdot 10^5 < Re_D &\leq 1.2 \cdot 10^6 & Nu_D &= 8.64 \cdot 10^{-3}\, Re_D^{0.81} \\ Re_D &> 1.2 \cdot 10^6 & Nu_D &= 0.0455\, Re_D^{0.81} \end{aligned} \tag{2.13}$$

D represents the outer diameter of the cylindrical receiver, while k_s is the the effective sand grain roughness height, approximately equal to the tubes radius. The Nusselt number Nu_D and the Reynolds number Re_D are defined as function of the air conductivity k, density ρ, velocity u and viscosity μ:

$$Nu_D = \frac{h\,D}{k} \qquad\qquad Re_D = \frac{\rho\,u\,D}{\mu} \tag{2.14}$$

After obtaining the Nusselt number, the heat transfer coefficient $\bar{h}_f$ can be obtained by eq. 2.14. To apply the model, also the wind velocity $\bar{u}$ must be considered constant – as well as the air thermophysical properties. Regarding natural convection, the Nusselt number for a totally turbulent flow is shown below as a function of the Grashof number Gr_H calculated respect to the height H of the receiver.

$$Nu_H = 0.098\, Gr_H^{1/3} {\frac{T_r}{T_{amb}}}^{-0.14} \qquad\qquad Gr_H = \frac{\rho^2\, g\, \beta\, \left(T_r - T_{amb}\right)\, H^3}{\mu^2} \tag{2.15}$$

β is air coefficient of thermal expansion and g is the gravity constant. As in forced convection, the heat transfer coefficient $\bar{h}_n$ can be obtained by inverting eq. 2.14. The air properties for natural and forced convection are calculated at the film temperature, defined as $T_{film} = \left(T_r + T_{amb}\right)/2$.

Apart from convective losses, the receiver releases part of its energy as thermal **radiation**. To estimate it, the receiver is assumed to be a diffuse surface and the ambient a black body.[3] The radiation emitted by a body is expressed as a function of the receiver emissivity ε_r, the Boltzmann constant $\sigma = 5.67 \cdot 10^{-8}\, W/m^2\, K^4$, the average sky-ground temperature T_{sg} and the view factor from the receiver to the surroundings F_{view}. However, since ambient is considered as a black body, $F_{view} = 1$.

$$\dot{Q}_{rad} = \varepsilon_r\, \sigma\, \left(T_r^4 - T_{sg}^4\right) \cancelto{1}{F_{view}} A_r = \varepsilon_r\, \sigma\, \left(T_r^4 - T_{sg}^4\right)\, A_r \tag{2.16}$$

---

[3] The sky-ground system can be thought as a cavity in which the receiver is located.

The sky-ground temperature is a fictitious temperature that makes it possible to factor in the radiation of the sky and the ground toward the receiver. Eq. 2.17 of the thermal efficiency can be expressed explicitly:

$$\eta_{th} = \frac{\dot{Q}_{in} - \dot{Q}_{lost}}{\dot{Q}_{in}} = \alpha_r - \frac{\varepsilon_r\,\sigma\,\left(T_r^4 - T_{sg}^4\right)\,A_r + h\,\left(T_r - T_{amb}\right)\,A_r}{\dot{Q}_{in}} \tag{2.17}$$

It is finally possible to express all the losses from the direct solar radiation on the mirrors to the HTF fluid. All the radiation incident on the receiver that is not lost in any process is absorbed by the HTF, as the total balance of energy suggests. This useful energy can be expressed as $\dot{Q}_u = \eta_{th}\,\dot{Q}_{in}$, where $\dot{Q}_{in}$ is a function of the direct normal radiation, the optical efficiency and the concentration ratio $C_r = A_c/A_r$ (where A_c is the collector area and A_r is the receiver area).

$$\dot{Q}_{in} = G_{bn}\,C_r\,A_r\,\eta_{opt} \tag{2.18}$$

Eq. 2.17 can be re-formulated as

$$\eta_{th} = \alpha_r - \frac{\varepsilon_r\,\sigma\,\left(T_r^4 - T_{sg}^4\right) + h\,\left(T_r - T_{amb}\right)}{G_{bn}\,C_r\,\eta_{opt}} \tag{2.19}$$

Finally, the absorbed useful heat $\dot{Q}_u$ can be expressed as a function of the direct solar radiation:

$$\dot{Q}_u = G_{bn}\,C_r\,A_r\,\eta_{opt}\,\eta_{th} \tag{2.20}$$

2.4.3 Performance analysis

Sec. 2.4.2.A and sec. 2.4.2.B provided a useful description to calculate the efficiency of the heliostat field and the receiver. In this section the equations presented will be applied to a hypothetical case to understand the impact of the single losses on the overall efficiency. Later on, a sensitivity analysis of many variables that influence them will be performed. The independent variables that will be considered are shown in tab. 2.3. During this analysis, some of them will be changed within a range, while all the others will be kept constant. This will help to understand the importance of that specific variable on the final heat loss balance. It is important to specify that the sensitivity analysis does not want to describe the impact of the variation of the parameters relative to an existing case, but only to estimate the effect of these parameters. This means that a change in a variable will not correspond to a different configuration of the plant, but instead to a fictitious case characterized by the new variable. For example, it is impossible to change the receiver emissivity without modifying the material used to make it; however, there could be a fictitious plant having a different receiver characterized by the requested emissivity. In this way, the goal of the study will be preserved: the assessment of the heat losses impact due to the change of the variables. The sensitivity analysis will not be made on all the variables, though, but just on the non-trivial (i.e. the ones that do not have a direct proportionality with the overall efficiency) and most significant ones.

The base case is the Solar Two Project located in the Mojave desert; the system data are collected from the plant evaluation test report given by Pacheco et al. (2002) [53]. Weather data refer to the sample day of 27 July 2017 at 16:00 solar time, recorded in the closest meteorological station situated at the Barstow airport ($34^{\circ}51'13''N$ $116^{\circ}47'12''W$) [54]. Tab. 2.3 shows the value of the parameters taken in the base case, and their range used in the sensitivity analysis.

Table 2.3: Performance parameters of the analysis of a sample CRS plant.

Parameter	Base case	Sensitivity analysis range	Parameter	Base case	Sensitivity analysis range
$G_{bn}\ [kW/m^2]$	750		$T_r\ [°]$	774	$290 \div 1200$
$\theta[°]$	30	$0 \div 90$	$T_{amb}\ [°]$	42	$5 \div 45$
ρ_h	0.91		$A_r\ [m^2]$	99.3	
η_{bs}	0.93		$k_s\ [cm]$	2.1	
$H_s\ [m]$	588		$D\ [m]$	5.1	
$\rho_w\ [\%]$	12	$0 \div 65$	$u\ [km/h]$	10	$0 \div 60$
$V_R\ [km]$	16	$5 \div 16$	$H\ [m]$	6.2	
$H_T\ [m]$	76.2		ε_r	0.85	$0.5 \div 1$
$R\ [m]$	126	$86 \div 407$	F_{view}	1	
η_{spil}	0.99		$A_c\ [m^2]$	10 260	
α_r	0.94				

Solar direct normal radiation is calculated using the Hottel model explained in Appendix A. The angle of incidence is taken between the minimum and maximum possible angle of a heliostat. It is assumed that θ corresponds to the average angle of incidence of the whole system of heliostats. Although it is impossible that the average angle takes the extreme values of the sensitivity range, it can happen that a single heliostat is oriented to have such angles. Since the goal of the analysis is to understand the effect of the angle of incidence in all its possible configurations, these extreme values are considered. The collector reflectivity is calculated averaging the reflectivity of the two different types of heliostats described in the report. The blocking/shading efficiency and the spillage efficiency, instead, are not cited; therefore, the *PS10* plant is taken as reference [55], since it has a similar configuration. The site elevation, the vapor concentration, the visibility range, the ambient temperature and the wind velocity are extracted from the weather station. Their sensitivity range is the guessed one for locations where a CRS could operate. The tower height, the slant range, the receiver absorptance, the receiver area, the tube radius, the receiver diameter and the receiver height are given in the report. The receiver average temperature is extracted from the computational study made by Christian & Clifford (2012) [56] regarding the real plant. During the sensitivity analysis, the minimum temperature considered is the minimum receiver temperature to start the production, while the maximum one is a hypothetical temperature of a highly-efficient CRS plant receiver, that could be made available in a future perspective. A temperature of 1200 °C would not be borne by solar salts, thus the fluid involved must be a different one (such as a liquid metal). The receiver emissivity is not given in the report, therefore a typical value for a solar receiver is considered [22]. The sky-ground temperature is assumed to be equal to the ambient temperature. Finally, the air thermophysical properties are found using a correlation of the temperature [57].

The base case results are presented in tab 2.4. With this configuration, the most impacting loss is the cosine effect loss. Atmospheric attenuation, instead, hardly has an influence. The overall efficiency is 68.5%: of the 61.05 MW of solar power 41.79 MW are absorbed by the HTF.[4] The sensitivity analysis assesses the losses dependence on the presented variables. The variation of the heat losses as a function of the variables are plotted (fig. 2.19- 2.23) in a normalized form, in which the base case value is equal to one in the y-axis. The results related to the variation of humidity, visibility and slant range produced almost no effect on the overall efficiency. This indicates that in clear days the air transmittance does not waver significantly. Moreover, the variation of the slant range is too small related to the one needed to have an impact on the air transmittance. The angle of incidence, instead, shows a relevant impact on the useful heat (linearly proportional to the overall efficiency), according to fig. 2.19. The useful heat is maximum when the heliostats are perpendicular to the sun, then the curve decreases as a cosine function until it reaches a theoretical value of $\dot{Q}_u = 0$ MW for $\theta \approx 88°$. The curve shows that it is crucial to keep the angle as close as possible to the sun ray direction: for $\theta > 88°$ the efficiency starts falling sharply. Plants try to maximize the cosine efficiency in the design of the heliostat system. At low latitudes the zenith angle of the sun is high, so the heliostats are placed around the tower, to

Table 2.4: Base case results – efficiency and heat balance.

	Efficiency [%]		Heat [MW]
η_{cos}	86.6	$\dot{Q}_{sol}$	61.05
η_{ref}	90.8	$\dot{Q}_{in}$	44.18
η_{bs}	93.0	$\dot{Q}_{r,\,ref}$	0.52
η_{atm}	99.3	$\dot{Q}_{conv}$	0.20
η_{spil}	99.0	$\dot{Q}_{rad}$	1.67
η_{opt}	72.4	$\dot{Q}_u$	41.79
η_{th}	94.6		
$\eta_{overall}$	68.5		

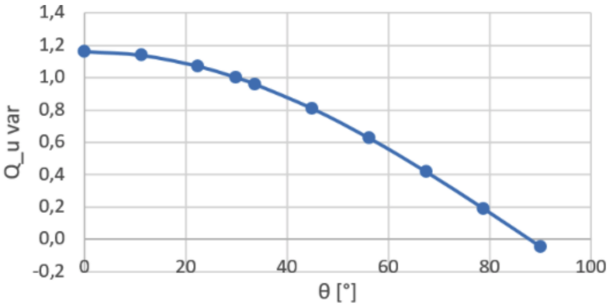

Figure 2.19: Useful heat $\dot{Q}_u$ as a function of the angle of incidence θ.

---

[4] The overall efficiency is defined, for simplicity, as the ratio of the HTF absorbed heat to the solar power due to direct radiation. It is equal to the product of the optical and thermal efficiency.

be maintained almost vertical. At higher latitudes, the tower position shifts to the south, so that the mirrors can point to the sun more efficiently [58]. The receiver temperature has a significant impact on the overall efficiency too. The useful heat decreases with the fourth power of T_r, complementary to the losses for radiation. Although radiative losses are rather higher than convective losses, in the base case they still have a limited impact on the overall efficiency; this can be seen comparing the thermal and the optical efficiency in tab. 2.4. However, the receiver temperature is expected to play an increasingly significant role in a future perspective, when it will reach higher values. The reason why a higher temperature is sought, although it means higher thermal losses, is explained by fig. 2.20(b). The figure shows the electrical power of a hypothetical Carnot cycle coupled to the system that is being analyzed: since the efficiency of the cycle rises if the maximum temperature of the fluid increases, the combined efficiency of the collector/receiver and the cycle can be higher if T_r increases. After a certain value, though, radiative losses become major than the gain in the cycle efficiency, and the power output starts decreasing. Carnot cycles are not feasible practically, but they are a simplified (but consistent) model to represent the plant's cycle efficiency as a function of the maximum temperature reached. Also the ambient temperature influences the receiver losses. This parameter affects both the convective and the radiative losses but hardly has an effect, as shown in fig. 2.21. Convective heat

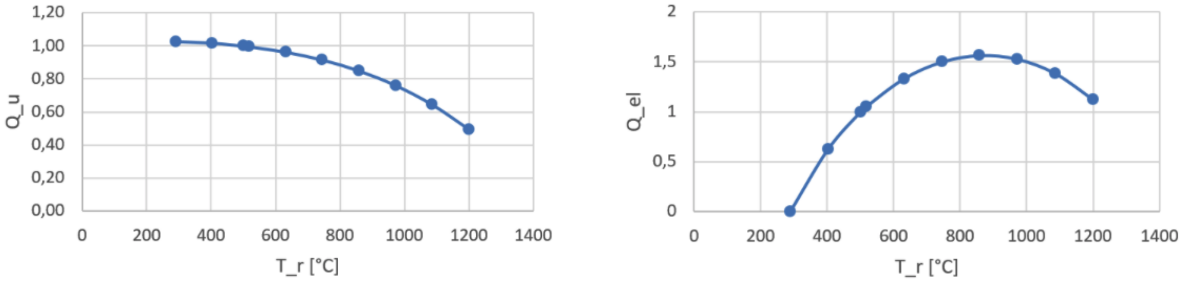

(a) Useful heat $\dot{Q}_u$ as a function of the receiver temperature

(b) Power output P_{el} for a hypothetical Carnot cycle given an incoming heat $\dot{Q}_u$ as in fig. 2.20(a)

Figure 2.20: Sensitivity analysis on the temperature of the receiver T_r.

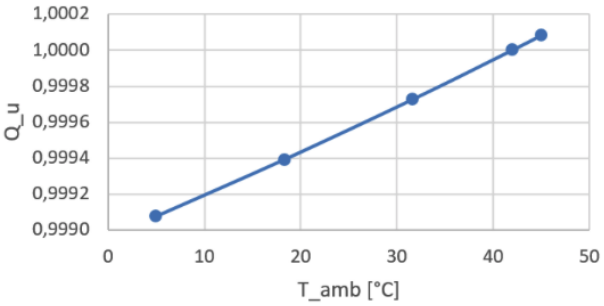

Figure 2.21: Useful heat $\dot{Q}_u$ as a function of the ambient temperature T_{amb}.

transfer starts to become relevant as the wind velocity increases. Fig. 2.22(a) shows that the useful heat decreases with the wind velocity. In particular, is it possible to spot a change in the curve declination: between 10 km/h and 15 km/h the effect of the roughness starts to influence forced convection.[5] This phenomenon contributes to raise the heat transfer coefficient and make forced convection dominant over natural convection. In a case of harsh winds (around 45 km/h), convection losses can become even higher than radiative losses. If these losses did not appear too relevant for the base case, the sensitivity analysis shows that they become it as the wind rises. The last parameter studied in the analysis is the receiver emissivity. The thermal efficiency decreases linearly with ε_r, as shown in fig. 2.23(a). Emissivity has a reasonable impact on radiative losses, so it should be kept low. Since emissivity and absorptance are usually linked for gray bodies, an additional analysis has been made, in which $\varepsilon_r = \alpha_r$, illustrated in fig 2.23(b). The dependence of the two optical properties shows that $\varepsilon_r = \alpha_r$ must be maximized to obtain the maximum useful heat. This leads to the conclusion that, although a low emissivity is

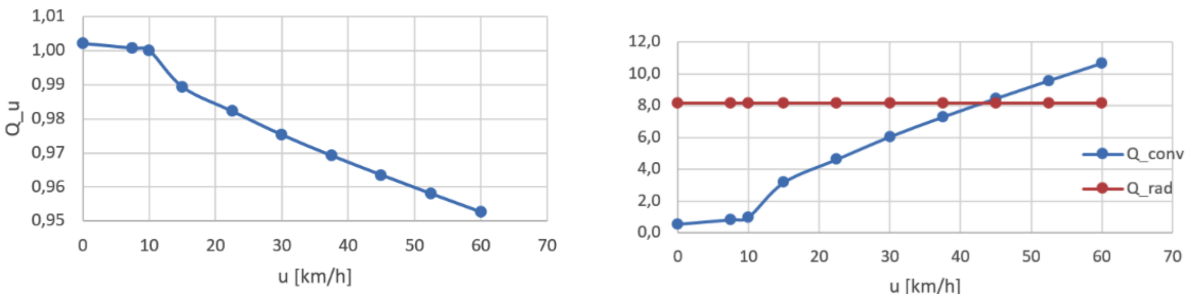

(a) Useful heat $\dot{Q}_u$ as a function of the wind velocity

(b) Comparison between convective and Radiative losses as a function of the wind velocity

Figure 2.22: Sensitivity analysis on the wind velocity u.

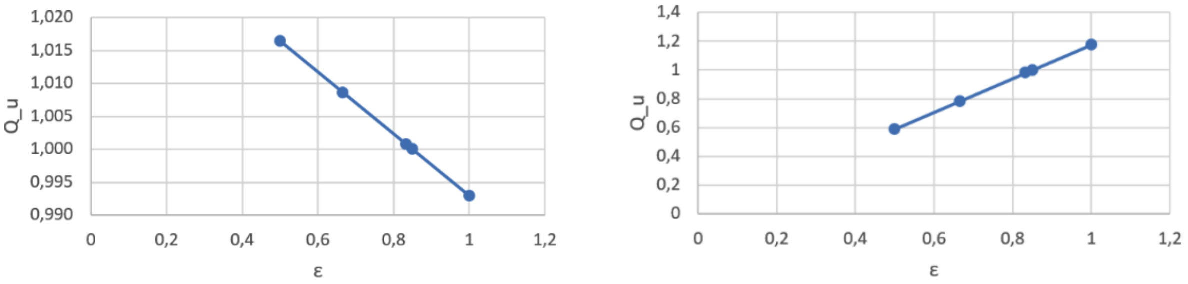

(a) Useful heat $\dot{Q}_u$ variation for a constant absorptance of the receiver α_r

(b) Useful heat $\dot{Q}_u$ variation for an absorptance of the receiver α_r equal to its emissivity ε_r

Figure 2.23: Sensitivity analysis on the receiver emissivity ε_r.

---

[5] In this range, however, the results are weaker. The transition zone is usually difficult to predict, especially with correlations, due to its unstable nature.

preferable, in the design of the receiver the absorptance must always have the priority. Gathering the information obtained in the analysis, it is now possible to draw some general considerations.

- Cosine losses have a great impact and are the first parameter to take into account in the design of the field, depending on its location, resulting in a precise heliostat field disposition.
- The receiver temperature is another important parameter for the correct design of the plant. Theoretically, if the HTF properties permit it, it should be raised until the radiative losses become more relevant than the thermodynamic cycle efficiency. The optimum temperature can be raised if the emissivity of the receiver is lowered. However, the latter parameter should not involve a lower absorptance of the receiver, which is crucial to maintain the thermal efficiency high. Selective materials can be used to achieve these results. Their ability to block a specific range of wavelengths of the radiation could make them absorb a high amount of solar radiation and block as much as possible infrared radiation (fig. 2.14 shows the spectrum of the two types of radiation).
- A higher receiver temperature could amplify natural convection, especially in case the wind velocity is relevant. A way to partly limit the convection in external cylindrical CRS could be made reducing the diameter of the tubes hence the roughness of the receiver.

A final consideration can be made, looking at eq. 2.19. A higher concentration ratio always improves the thermal efficiency of the receiver. A higher area of the collector, though, means that the heliostats are placed farther from the tower. This could have a limited impact in lowering the blocking/shading, the atmospheric and the spillage efficiency. Its main drawback, however, is that the investment cost raises, so a high concentration ratio is advisable as long as it is economically convenient.

2.4.4 Towards a new model for convective heat transfer

The analysis helped to understand the efficiency balance from the incoming direct solar radiation until the thermal power absorbed by the fluid. It is important to remark that this power must be guaranteed by a correspondent design of the receiver (that is, in this case, the heat exchanger). This process must take into consideration the conduction among the receiver parts and the convection between the receiver and the HTF, and how they are affected by different temperatures: in fact, the receiver is characterized by sharp gradients of temperature that make the heat transfer processes vary a lot depending on the location. Without this correct the design, it is not possible to guarantee the energy balance and thus operate at the rated temperature of the receiver.

Considering the thermal losses at the receiver, the analysis showed that radiative losses represent the major cause. However, convective losses are still relevant, since they represent around a 10% of the receiver losses. This value, moreover, increases dramatically with the wind velocity. In future, the use of selective surfaces resistant to high temperatures and oxidation could reduce the radiative losses dramatically, increasing the relative impact of convective losses in a significant way. It is clear, then, that convection phenomena must be known properly.

However, heat transfer is especially hard to model whenever convection is involved. The first reason is that convective heat transfer always includes a certain grade of turbulence. Turbulence is really tough to model given its unstable nature. Correlations rely on simplifications that usually do not occur, regarding, for example, roughness, geometry, thermophysical properties of the fluid. Moreover, turbulence shifts the heat losses from a global to a local point of view: if, one one hand, solar radiation still hits the surface of the receiver in an organized way (assumed to be a Gaussian distribution in sec. 2.4.2.A), on the other hand the turbulence that generates due to air convection leads to a chaotic motion of the fluid that makes the heat losses strongly locally dependent, without giving the possibility to describe them with a global distribution. Although the empirical correlation of Siebers & Kraabel represents an established formula accepted by the literature in numerous cases, it is clear that it cannot solve heat transfer locally. However, a prediction of the local conditions of the flow is crucial, since the fluid can influence significantly the temperature of the receiver and its local thermal stresses. Material failure due to overheating still represents a major issue in modern thermal receivers [9]. In particular, it must be guaranteed that the maximum temperature does not exceed the limits of the material. This can be done only if the local conditions of the receiver are modeled in a proper way and, consequently, the fluid flow is locally predicted.

It is then clear that a suitable efficacious model to assess the locally dependent properties of the convective flow is needed. CFD has been already presented in sec. 1.1, and it represents a rather interesting option: it directly tackles the governing equations involved in convection, and solves them with a consistent approach, being able to handle the unsteadiness and variability of the thermodynamic state of the system. Obviously some assumptions still have to be made, but they are far closer to the reality than what a global approach does. Numerical simulation is also effective in the other heat transfer processes (conduction and radiation) and makes all of them able to be coupled. Another advantage that it has is that it can predict the flow variations during transients: for example whenever the fluid cycle is regulated, or in the initial transient before reaching the nominal operative conditions. CFD can also be useful to describe the convection of the HTF in the receiver, in the storage process and in the condensation of the fluid: all these steps comprise a certain rate of convection, that must be predicted to optimize the system and make it safe. Given all these advantages, CFD is selected to be the way to analyze convection in the next chapters. As a first modelization, a CFD code will be developed to study natural convection.

CFD studies applied to natural convection of thermal receiver are largely available in the literature. Among the studies relative to tubular receivers, Christian & Clifford (2012) used a Spalart-Allmaras turbulence model to evaluate the convective and radiative losses of the Solar Two cylindrical receiver [56].

Kim, Kim & Stein (2015) analyzed a series of progressively enclosed receivers, varying from an external receiver to a full cavity receiver [59]. They used a standard $k-\varepsilon$ model. Both works were carried out with the ANSYS FLUENT commercial code, and do not mention the treatment of the thermophysical properties (if some were considered constant or not). Fang, Wei, Dong & Wang analyzed natural and forced convection of a cavity receiver under windy conditions (2011) [60]. Again, they used a standard $k-\varepsilon$ model solved with FLUENT. Very few works used a Direct Numerical Simulation approach to study natural convection; one important example is the work of Lé Queré, Minot & Mirenayat (1981), that studied an isothermal cubic open cavity [61]. Lé Queré also published many articles about turbulent natural convection in air-filled cavities with Direct Numerical Simulations and Large Eddy Simulations, also considering the effect of the variation of the thermophysical properties due to the change of temperature, in 2004 [62] and 2005 [2].

The objective of the next chapters is to develop an important numerical tool that can be applied to energy and mass transfer processes, and show its effectiveness when applied in the analysis of the natural convection of a cylindrical external receiver. The CFD codes will be developed by using the C++ programming language. Its main advantage is that it is a compiled language, which makes it really efficient and keeps the time of execution low, even though it presents a good rate of flexibility. Many commercial CFD programs already exist, but the goal of this thesis is to develop a code from scratch optimized for the study natural convection at the receiver of a solar tower.

After an explanation of the main phenomena analyzed, the code developed will be verified and validated with the literature, in order to build up a reliable computational structure that is able to tackle natural convection.

3

Mathematical Formulation and Numerical Methodology

Contents

Engineering processes that involve fluid dynamics and heat transfer are all governed by laws that can be expressed, with a certain amount of simplification, by a set of equations. All of these equations are based on the conservation of a specific property and involve the constitutive nature of the material. In this thesis, three main conservation equations will be considered. They regard three quantities: mass, momentum, and energy. The equations will be solved directly, at every time step, without any turbulence model. This approach is called Direct Numerical Simulation (DNS).[1] The advantage of using it is that it is the most precise (and therefore reliable) to describe mass and energy transformation processes: all the scales of energy transfer are computed, without having to formulate theoretical models to simplify the computation process.

3.1 Governing Equations

Before analyzing each equation singularly, it is important to understand that the mass, the momentum and the energy conservation equations can be viewed as a particular case of a single equation: the **convection-diffusion equation**. In its differential form, it can be expressed as in the form

$$\underbrace{\frac{\partial(\rho\,\phi)}{\partial t}}_{\text{I}} + \underbrace{\nabla\cdot(\rho\,\mathbf{u}\,\phi)}_{\text{II}} = \underbrace{\nabla\cdot(\Gamma\,\nabla\phi)}_{\text{III}} + \underbrace{S_\phi}_{\text{IV}} \tag{3.1}$$

where ρ is the fluid density, ϕ is the variable of interest, $\mathbf{u}$ is the velocity vector, Γ is the diffusion coefficient and S_ϕ is the source term. This equation describes a phenomenon in which the property ϕ is transported by means of two phenomena: convection and diffusion. It can be divided in four terms:

I. The rate of change of the variable. It indicates the change of variable due to its accumulation.

II. The convective term. It indicates the transport of the quantity due to the flow of the fluid.

III. The diffusive term. It indicates the transport of the quantity due to the interaction with close particles.

IV. The source term. It indicates the rate of generation of the quantity in the domain.

Mass, momentum and energy equations only represent different form of this equation, and the aforementioned terms can be pointed out in all of them. They are presented below, in their differential form.

Table 3.1: Convection-diffusion equation form for mass, momentum and energy equations.

Equation	ϕ	Γ	S_ϕ
Mass	1	0	0
Momentum	$\mathbf{u}$	μ	$-\nabla p + \nabla\cdot\boldsymbol{\tau} - \nabla\cdot(\mu\nabla\mathbf{u}) + \rho\mathbf{g}$
Energy	u	k	$-\nabla\cdot\dot{\mathbf{q}} - p\nabla\cdot\mathbf{u} + \boldsymbol{\tau} : \nabla\mathbf{u}$

---

[1] The literature usually refers to a simulation as DNS only when all the three dimensions are involved. However, a direct solution of the 2D Navier-Stokes equation can be performed as well (just neglecting the projection of the equation on the third axis). For simplicity, from now on the approach will be said to be a DNS also when applied to a 2D studies.

Mass conservation equation

The differential form of the mass conservation equation is

$$\frac{\partial \rho}{\partial t} + \nabla \cdot (\rho\,\mathbf{u}) = 0 \tag{3.2}$$

The velocity vector as a function of its independent components is $\mathbf{u} = u\,\mathbf{i} + v\,\mathbf{j} + w\,\mathbf{k}$, where u, v and w are the velocities referred to the x, y and z axes respectively. Eq. 3.2 is also known as **continuity equation**. It states that the mass increase in an infinitesimal control volume is equal to the net flux on the control volume (so, basically, that no mass can be generated). Using the mass conservation equation and the calculus identities B.1 and B.2, the right-hand side of the convection-diffusion equation becomes

$$\rho\,\frac{\partial \phi}{\partial t} + \rho\,\mathbf{u}\cdot\nabla\phi + \underbrace{\cancelto{0}{\phi\,\frac{\partial \rho}{\partial t} + \phi\,(\nabla\cdot(\rho\,\mathbf{u}))}}_{\text{mass conservation}} = \rho\,\frac{\partial \phi}{\partial t} + \rho\,\mathbf{u}\cdot\nabla\phi \tag{3.3}$$

Momentum conservation equation

The differential form of the momentum conservation for a Newtonian fluid equation is

$$\rho\,\frac{\partial \mathbf{u}}{\partial t} + \rho\,(\mathbf{u}\cdot\nabla)\,\mathbf{u} = -\nabla p + \nabla\cdot\boldsymbol{\tau} + \rho\,\mathbf{g} + \,\mathbf{f_e} \tag{3.4}$$

$\boldsymbol{\tau}$, the **deviatoric stress tensor**, is defined as $\boldsymbol{\tau} = \mu\,\left(\nabla\mathbf{u} + \nabla\mathbf{u}^{\mathrm{T}}\right) - \frac{2}{3}\,\mu\,(\nabla\cdot\mathbf{u})\,\mathbf{I}$, where μ is the dynamic viscosity and $\mathbf{I}$ is the identity matrix. p is the pressure, $\mathbf{g}$ is the gravity acceleration and $\mathbf{f_e}$ represents the surface body forces (except gravity). In the problems considered, the latter term will be equal to zero. The equation, then, can be rewritten as

$$\rho\,\frac{\partial \mathbf{u}}{\partial t} + \rho\,(\mathbf{u}\cdot\nabla)\,\mathbf{u} = -\nabla p + \nabla\cdot\left(\mu\,(\nabla\mathbf{u} + \nabla\mathbf{u}^{\mathrm{T}}) - \frac{2}{3}\,\mu\,(\nabla\cdot\mathbf{u})\,\mathbf{I}\right) + \rho\,\mathbf{g} + \,\mathbf{f_e} \tag{3.5}$$

The momentum is associated with the kinetic energy of the system. The nonlinearity nature of the term $\rho\,(\mathbf{u}\cdot\nabla)\,\mathbf{u}$ is the main responsible for turbulence.

Energy conservation equation

The energy equation states that the internal energy increase of a fluid is equal to the net sum of the heat fluxes around it. It can be written as the function of the specific internal energy of the fluid u, the external heat flux $\dot{\mathbf{q}}$ and the rate of generation of the specific internal energy Φ_e.

$$\rho\,\frac{\partial \mathrm{u}}{\partial t} + \rho\,\mathbf{u}\cdot\nabla\mathrm{u} = -\nabla\cdot\dot{\mathbf{q}} - p\,\nabla\cdot\mathbf{u} + \underbrace{\cancelto{0}{\boldsymbol{\tau}:\nabla\mathbf{u}}}_{\text{friction negligible}} + \Phi_e \tag{3.6}$$

In heat exchange problems the contribution of the deviatoric stresses on energy can be considered negligible compared to the other terms appearing in the equation. In this dissertation also Φ_e will be considered null. The internal energy of a fluid can be expressed as a function of the temperature T and the specific heat c_P as $d\mathrm{u} = c_P \, dT$. Assuming that c_P is constant and writing heat conduction explicitly ($q = -k \, \nabla T$, according to Fourier's law), the energy conservation equation can be rearranged as

$$\rho \, c_P \, \frac{\partial T}{\partial t} + \underbrace{\rho \, c_P \, \mathbf{u} \cdot \nabla T}_{\text{II}} = \underbrace{\nabla \cdot (k \, \nabla T)}_{\text{III}} - \nabla \cdot \dot{\mathbf{q}}^R - p \, \nabla \cdot \mathbf{u} \tag{3.7}$$

k is the thermal conductivity. $\dot{\mathbf{q}}^R$ represents the remaining heat flux not due to conduction (e.g. the radiative heat flux). In eq. 3.7 it is possible to recognize the convective and diffusive terms (II and III).

Incompressible flow

In case of incompressible flow ($\frac{d\rho}{dt} = 0$), the mass, the momentum and the energy equations can be reformulated. Eq. 3.2 is reduced to the form

$$\nabla \cdot \mathbf{u} = 0 \tag{3.8}$$

Using eq. 3.8 and the rate-of-strain tensor $\mathbf{S} = \frac{1}{2} \left(\nabla \mathbf{u} + \nabla \mathbf{u}^{\mathrm{T}} \right)$, the momentum equation becomes

$$\rho \, \frac{\partial \mathbf{u}}{\partial t} + \rho \, (\mathbf{u} \cdot \nabla) \, \mathbf{u} = -\nabla p + \nabla \cdot (2 \, \mu \, \mathbf{S}) + \rho \, \mathbf{g} \tag{3.9}$$

In case the viscosity is constant, applying the identities B.3, B.4 and eq. 3.8, the equation becomes

$$\rho \, \frac{\partial \mathbf{u}}{\partial t} + \rho \, (\mathbf{u} \cdot \nabla) \, \mathbf{u} = -\nabla p + \mu \, \nabla^2 \mathbf{u} + \rho \, \mathbf{g} \tag{3.10}$$

where ∇^2 represents the Laplacian. Eq. 3.10 represents the **Navier-Stokes equation** for incompressible fluids. The energy equation, finally, becomes

$$\rho \, c_P \, \frac{\partial T}{\partial t} + \rho \, c_P \, \mathbf{u} \cdot \nabla T = \nabla \cdot (k \, \nabla T) - \nabla \cdot \dot{\mathbf{q}}^R \tag{3.11}$$

Boussinesq approximation

Although the incompressible form of the governing equations simplifies significantly the mathematical formulation of fluid dynamics, many times it is too distant from the reality to be applied. The Equation Of State (EOS) of a fluid usually expresses the density as a function of temperature and pressure ($\rho = \tilde{\rho} \, (p, \, T)$). Convection heat transfer always involves a variation of these two variables to a certain degree; however, if on the one hand the pressure usually changes within a limited range, especially in natural convection, on the other hand the temperature always vary enough to have a tangible influence on the density. The Boussinesq approximation permits to combine simplified equations and the effect of the density variation where it counts more: in the buoyancy forces. This approximation states that the density is considered constant ($\rho = \rho_0$, where $\rho_0 = \tilde{\rho}\,(T_0)$) everywhere except in the term that multiplies the gravity acceleration, responsible for the buoyancy forces, where it is considered to be linear with the temperature. This assumption is only valid if ΔT is little, so that the density can effectively be assumed as linear and $\Delta\rho \ll \rho_0$. In the mass conservation equation ρ remains constant, so the final form is equal to eq. 3.8. Together with the Boussinesq approximation, it is generally assumed that k, c_P and μ are constant as well. The Navier-Stokes equation becomes

$$\rho_0 \frac{\partial \mathbf{u}}{\partial t} + \rho_0\,(\mathbf{u}\cdot\nabla)\,\mathbf{u} = -\nabla p + \mu\,\nabla^2\mathbf{u} + \rho_0\,[1 - \beta\,(T - T_0)]\,\mathbf{g} \tag{3.12}$$

where β is the thermal expansion coefficient of the fluid. $\rho_0\,\mathbf{g}$ is usually merged with the pressure: given that $\mathbf{g} = -g\,\mathbf{k}$, where g is the gravity constant, it is possible to define $\nabla p' = \nabla p - \rho_0\,\mathbf{g} = \nabla p + \rho_0\,g\,\mathbf{k} = \nabla p + \rho_0\,g\,\nabla z = \nabla\,(p + \rho_0\,g\,z)$. Then, the momentum and the energy equation can be written as

$$\rho_0 \frac{\partial \mathbf{u}}{\partial t} + \rho_0\,(\mathbf{u}\cdot\nabla)\,\mathbf{u} = -\nabla p' + \mu\,\nabla^2\mathbf{u} - \rho_0\,\beta\,(T - T_0)\,\mathbf{g} \tag{3.13}$$

$$\rho_0\,c_P \frac{\partial T}{\partial t} + \rho_0\,c_P\,\mathbf{u}\cdot\nabla T = k\,\nabla^2 T - \nabla\cdot\dot{\mathbf{q}}^R \tag{3.14}$$

Conduction in solids

Conduction in solids can be viewed as a particular case of eq. 3.11 where $\mathbf{u} = 0$.

$$\rho\,c_P \frac{\partial T}{\partial t} = \nabla\cdot(k\,\nabla T) - \nabla\cdot\dot{\mathbf{q}}^R + \phi_e \tag{3.15}$$

Stream function and vorticity

The governing equations have been expressed as function of velocity. However, they can also be expressed using the stream function and the vorticity. The advantage of this approach is that it involves a minor number of equations in 2D cases (considering that eq. 3.13 must be projected on the x and y axis to be solved). This method can be applied only when $\nabla\cdot\mathbf{u} = 0$. The condition is always respected by giving the definition of the **stream function** $\boldsymbol{\psi}$, that is such that

$$\mathbf{u} = \nabla\times\boldsymbol{\psi} \tag{3.16}$$

Applying the identity B.5, eq. 3.8 is respected automatically, and does not need to be solved. If the flow is 2D, the stream function can be expressed as a scalar function. The details are explained in sec. B.3.

The stream function becomes $\boldsymbol{\psi} = \psi\,\mathbf{k}$, and the velocity projections can be easily expressed as

$$u = \frac{\partial \psi}{\partial y}, \qquad\qquad v = -\frac{\partial \psi}{\partial x} \tag{3.17}$$

Knowing the velocity components, ψ can be obtained by

$$\psi = \int_A^B u\,dy - v\,dx \tag{3.18}$$

The vorticity $\boldsymbol{\omega}$, instead, is defined as

$$\boldsymbol{\omega} := \nabla \times \mathbf{u} \tag{3.19}$$

In a 2D case, as explained by sec. B.3, $\boldsymbol{\omega}$ becomes $\boldsymbol{\omega} = \omega\,\mathbf{k}$, where

$$\omega = \frac{\partial v}{\partial x} - \frac{\partial u}{\partial y} = -\nabla^2 \psi \tag{3.20}$$

Although the governing equations as functions of the stream function and the vorticity will not be used, these parameters will be calculated to compare the results with reference cases of other authors.

3.2 Numerical Methodology

The CFD approach consists in resolving the governing equations of fluid dynamics by means of numerical analysis. The discretization method used in this dissertation is the Finite Volume Method (FVM), since it is particularly suitable in simple geometries that are modeled using structured meshes; such meshes will be used in this thesis, because no complex geometries are investigated. A mesh is said to be structured if it is identified by regular connectivity. The FVM approach consists in discretizing the governing equations on a mesh and integrate them in non-overlapping control volumes associated to every node of the mesh. For every node a unique thermodynamic state is defined. Properties are not only defined at the nodes: whenever the equations involve properties that must be calculated at the volume surfaces, a suitable interpolation method is used. These methods will be explained later on in convection problems.

The approach used to discretize the mesh is based on rectangular-face control volumes, as shown by fig. 3.1. This approach is called **Node Centered**: every node is situated at the center of the control volume it refers to. At the boundaries, the nodes have no volume, so the equations are solved in their differential form using consistent boundary conditions. For every node P, the neighboring nodes W, E, S, N and the outer faces w, e, s, n are defined (in the 3D case the bottom and top nodes B, T and they relative faces b, t also appear). The derivatives at the faces are calculated as the difference of the property at two adjacent points divided by their distance. For example, $\left.\frac{\partial T}{\partial x}\right|_w = \frac{T_P - T_W}{d_{PW}}$, where d_{PW} is

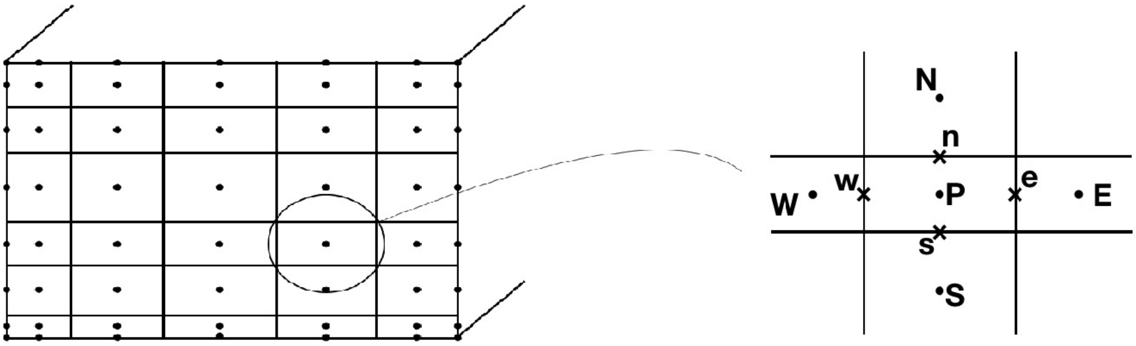

Figure 3.1: Collocated 2D mesh together with the nomenclature used for neighboring nodes and faces.

the distance between the nodes P and W. Time discretization, instead, depends on the method used. A method is said to be **explicit** if the variable to be computed only depends on known variables, while it is said to be **implicit** if it also depends on unknown variables. The discretization is performed at the center of the time step; there are many types of implicit and explicit methods, and each one defines a way to calculate the variables at $n + 1/2$ (n is the current time step, $n + 1$ is the next time step). Some methods of first and second order will be presented in the problems of the next chapter.[2] The derivatives in time are discretized at $n + 1/2$ as well (e.g. $\frac{\partial \rho}{\partial t}\big|_{n+1/2} = \frac{\rho^{n+1} - \rho^{n}}{\Delta t}$). After the discretization, it is always possible to express the equations for the point P as a function of the neighboring points:

$$a_P \, \phi_P^{n+1} = a_W \, \phi_W^{n+1} + a_E \, \phi_E^{n+1} + a_S \, \phi_S^{n+1} + a_N \, \phi_N^{n+1} + a_B \, \phi_B^{n+1} + a_T \, \phi_T^{n+1} + b_P \tag{3.21}$$

a_P, a_W, a_E, a_S, a_N, a_B, a_T, b_P are the **discretization coefficients**. b_P is the coefficient of the known variables, while all the other coefficients multiply an unknown variable. The existence and uniqueness of a solution to the set of algebraic equations is guaranteed by the fact that the number of the equations is equal to the number of unknowns, since for every node there exists an equation. In an explicit method eq. 3.21 reduces to the form $a_P \, \phi_P^{n+1} = b_P$, since there are no unknown variables except the one at the node. Explicit methods have the advantage of being low CPU consuming, since they compute the property directly. The main drawback of these methods is that they must fulfill the Courant–Friedrichs–Lewy (CFL) condition to be stable: the time step must be small enough to make the discretized equations consistent with the initial governing equations [64]:

$$\Delta t < C \, \Delta x, \qquad\qquad \Delta t < C \, \Delta x^2 \tag{3.22}$$

where C is a number that depends on the governing equation it is referred to and the thermodynamic state of the system. In complex problems a fine mesh is needed, so the time step has to be small and the

---

[2] A convergence method is said to be of order n if the error is proportional to the n-th power of the step size [63].

number of iteration dramatically rises. Implicit methods, instead, are unconditionally stable. Therefore, a higher time step can be chosen; however, many iterations per time step are needed. In fact, the properties are calculated by means of an iterative method that hypothesizes them and computes them until the result of two subsequent iterations differs by a value minor than the **convergence parameter** δ. δ is a value set before the iteration and represents to the computational error. The choice between an implicit or explicit method depends on the nature of the problem.

Staggered Mesh

A **collocated mesh** is a mesh where all the properties are defined at the nodes, as explained in the previous section. Together with this approach, the **staggered mesh** approach will be used. In a staggered mesh, the variables that are expressed as vectors (in this case the velocity) are defined in a secondary grid where the center of the control volumes are located at the center of the faces of the collocated grid. The gray areas that cover u_P and v_P shown in fig. 3.2 correspond to the control volumes of the grids staggered along the x and y axes respectively. To calculate the velocities on the collocated mesh, an interpolation among consecutive points of the staggered mesh is performed.

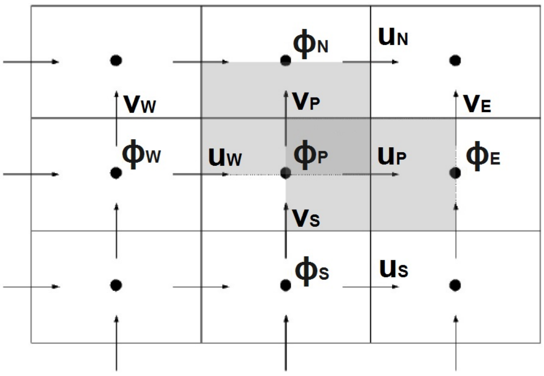

Figure 3.2: Staggered mesh. The gray areas represent the x and y staggered control volumes.

Staggered grids will be used because they can avoid incorrect odd-even decoupling between pressure and velocity, and can be easily defined in structured grids.

Iterative solver

In implicit methods, a line-by-line Tri-Diagonal Matrix Algorithm (TDMA) algorithm is used, which consists in solving any column of the mesh with the TDMA algorithm, and then loop them with a Gauss-Seidel algorithm.[3] In 3D problems, surfaces are looped one more time with the Gauss-Seidel algorithm.

---

[3] TDMA and Gauss-Seidel iterative solvers are described by Conte & Boor (1980) [65].

4

Heat Transfer Processes – Computational Study

Contents

4.1 Convection-Diffusion Equation

The first two problems represent a first numerical model to study two phenomena widely present in heat and mass transfer: diffusion and convection.

4.1.1 Two-Dimensional Heat Conduction in a Nonuniform Material

The first problem analyzed treats the phenomenon of diffusion through heat conduction. In a solid, heat propagates through diffusion between molecules, since no motion is involved.

Problem definition

An infinitely long rod is composed of four different materials that have different properties. The west wall is in contact with a fluid at $T_{gW} = 33\,°\mathrm{C}$ and heat transfer coefficient of $h_W = 9\,\mathrm{W/m^2K}$. The east wall temperature varies as $T = 8 + 0.005\,t\,°\mathrm{C}$. The south wall is kept constant at $T = 23\,°\mathrm{C}$. The north wall is heated by a uniform flux of $\dot{Q}_{fN} = 60\,\mathrm{W/m}$.[1] The initial temperature field is $T_0 = 8\,°\mathrm{C}$. The goal is to show the numerical solution of the diffusion equation and calculate the T field variation for $t \in [0,\, 10000]$ s.

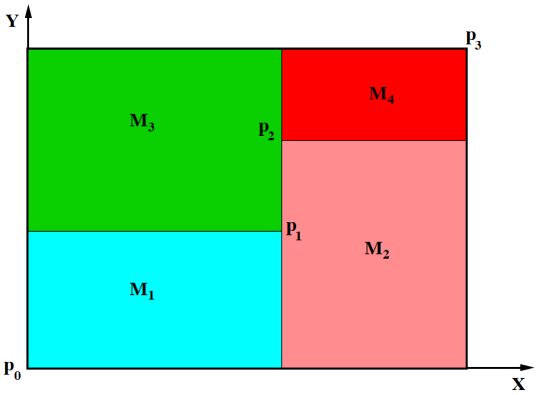

Figure 4.1: Section of the rod, showing the four materials it is composed of.

	$x[m]$	$y[m]$
p_1	0.5	0.4
p_2	0.5	0.7
p_3	1.1	0.8

	$\rho[kg/m^3]$	$c_P[J/kg\,K]$	$k[W/m\,K]$
M_1	1500	750	170
M_2	1600	770	140
M_3	1900	810	200
M_4	2500	930	140

Table 4.1: Geometric coordinates and physical properties of the four materials.

Resolution of the governing equations

Heat conduction in a solid is governed by eq. 3.15. ϕ_e is null in this case. To make a more general case in which convection and incoming flow are possible at every wall, the boundary conditions are reformulated in tab. 4.2. Since a value of $h = \infty$ is not possible to use in numerical computation, a value of $h_E = h_S = 10^{30}$ is used. NB indicates the neighboring node or in this case the outer conditions.

---

[1] 60 W/m distributed along an edge long 1.1 m result in a heat flux $\dot{q}_f = 54.5\,\mathrm{W/m^2}$.

Table 4.2: Boundary conditions of the four material problem reformulated.

Wall $[NB]$	$T_{gNB}[^\circ C]$	$h_{NB}[W/m^2\,K]$	$\dot{Q}^{\leftarrow}_{fNB}[W/m]$
W	33	9	0
E	$8+0.005\,t$	∞	0
S	23	∞	0
N	0	0	60

The section of the rod is divided such that the control volumes between p_0 and p_1, p_1 and p_2, p_2 and p_3 have the same height, and the ones between p_0 and p_1, p_1 and p_3 have the same length. The horizontal nodes numeration ranges from 1 to $N1+N2$ for internal nodes ($N1, j$ are the nodes of the volumes that have x_{p_1} as coordinate of the east face), and the vertical numeration ranges from 1 to $M1+M2+M3$. Eq. 3.15 is integrated in space for the internal nodes:

$$\int_V \rho\, c_P \frac{\partial T}{\partial t}\, dV = \int_V \nabla \cdot (k\, \nabla T)\; dV \tag{4.1}$$

Applying the divergence theorem B.7, discretizing in space and considering that ρ and c_P are constant in the volumes and $S_w = S_e$ and $S_s = S_n$, the equation becomes

$$\rho_P\, c_{P_P} \frac{\partial T_P}{\partial t} V_P = -k_w \frac{T_P - T_W}{d_{PW}} S_w + k_e \frac{T_E - T_P}{d_{PE}} S_w - k_s \frac{T_P - T_S}{d_{PS}} S_s + k_n \frac{T_N - T_P}{d_{PN}} S_s \tag{4.2}$$

After time integration the equation becomes

$$\begin{aligned} \rho_P\, c_{P_P} \frac{T_P^{n+1} - T_P^n}{\Delta t} V_P = \beta \left[\left(-k_w \frac{T_P - T_W}{d_{PW}} + k_e \frac{T_E - T_P}{d_{PE}} \right) S_w + \left(-k_s \frac{T_P - T_S}{d_{PS}} + k_n \frac{T_N - T_P}{d_{PN}} \right) S_s \right]^{n+1} \\ + (1-\beta) \left[\left(-k_w \frac{T_P - T_W}{d_{PW}} + k_e \frac{T_E - T_P}{d_{PE}} \right) S_w + \left(-k_s \frac{T_P - T_S}{d_{PS}} + k_n \frac{T_N - T_P}{d_{PN}} \right) S_s \right]^{n} \end{aligned} \tag{4.3}$$

β is a parameter that makes it possible to use different integration schemes: $\beta = 0$ corresponds to the *explicit Euler* method, $\beta = 1$ to the *implicit Euler* method and $\beta = 1/2$ corresponds to the *Crank-Nicolson* method. The discretization coefficients are shown below:

$$\begin{aligned} &a_W = \beta\, k_W \frac{S_w}{d_{PW}}, \quad a_E = \beta\, k_E \frac{S_w}{d_{PE}}, \quad a_S = \beta\, k_S \frac{S_s}{d_{PS}}, \quad a_N = \beta\, k_N \frac{S_s}{d_{PN}}, \quad a_P = \rho\, c_P \frac{V_P}{\Delta t} + a_W + a_E + a_S + a_N, \\ &b_P = \rho\, c_P \frac{V_P}{\Delta t} T_P^n + (1-\beta) \left[\left(-k_w \frac{T_P^n - T_W^n}{d_{PW}} + k_e \frac{T_E^n - T_P^n}{d_{PE}} \right) S_w + \left(-k_s \frac{T_P^n - T_S^n}{d_{PS}} + k_n \frac{T_N^n - T_P^n}{d_{PN}} \right) S_s \right] \end{aligned} \tag{4.4}$$

k is referred to the face, and assumes a value of $k_f = \frac{d_{RL}}{d_{Lf}/k_L + d_{Rf}/k_R}$ at the boundary between two materials, where R and L are the right and left nodes respectively.[2] At the boundaries, the sum of the incoming heat flux (convective flux and given flow) on the surface and the outgoing one (the conductive

---

[2] k_f is defined in this way to make the heat flux equal on both sides of the surface. The explanation is given in sec. B.4.

flux) must be zero. In fact, the nodes have no volume, so there is no accumulation of energy.

$$h_{NB}\left(T_{gNB}^{n+1}-T_P^{n+1}\right)+\frac{\dot{Q}_{fNB}^{\leftarrow}}{L}=-k_P\,\frac{T_{NB}^{n+1}-T_P^{n+1}}{d_PNB} \tag{4.5}$$

where h_{NB} is the heat transfer coefficient of the gas outside the NB wall and $\frac{\dot{Q}_{fNB}^{\leftarrow}}{L}$ is the given flow. The discretization coefficients can be extracted from eq. 4.5.

$$a_{NB}=\frac{k_P}{d_{PNB}},\qquad a_P=h_{NB}+a_{NB},\qquad b_P=h_{NB}\,T_{g\,NB}^{n+1}+\frac{\dot{Q}_{fNB}^{\leftarrow}}{L} \tag{4.6}$$

For the explicit scheme, the CFL condition needed is shown below

$$\Delta t\leq 0.25\,\min\frac{\Delta x\,\Delta y}{k/\rho\,c_P} \tag{4.7}$$

Results

The problem is solved using a constant collocated mesh of 66×48 internal control volumes.[3] The code is tested with the reference solution obtained by the team of the Heat and Mass Transfer Technological Center (CTTC) of Terrassa. Fig. 4.2 shows the heat maps obtained with a time step $\Delta t=100\,\mathrm{s}$ (except the explicit scheme that nedeed a $\Delta t=0.09\,\mathrm{s}$ to respect the CFL conditions). The explicit Euler makes almost no error, since it time step is really low; the Crank-Nicolson method, still, is a second order method, so it has a high accuracy despite the large time step. The implicit Euler is a first order method and has a large time step, so it makes a small error, as fig. 4.2 shows. Setting a time step of $\Delta t=1\,\mathrm{s}$ almost no difference is found.

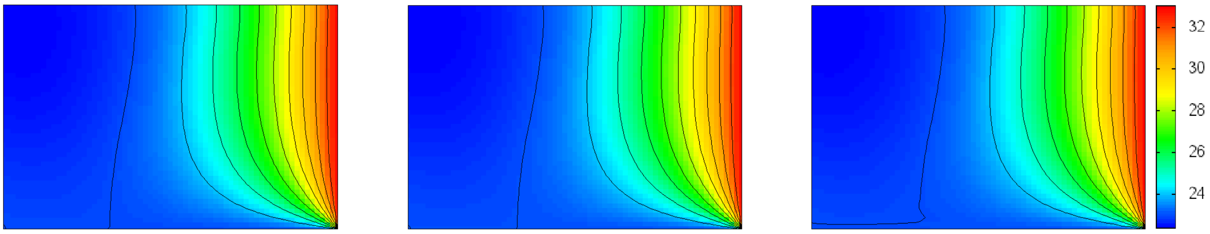

(a) Explicit Euler **(b)** Crank-Nicolson **(c)** Implicit Euler

Figure 4.2: Temperature maps of the material section at $t=5000\,s$.

The initial time variation of the temperatures of two locations can be found in fig. C.1. The explicit Euler almost overlaps with the reference solution, while both the Crank-Nicolson and the implicit Euler

---

[3] The actual mesh is, therefore, 68×50, due to the external nodes. The notation used in the dissertation will always refer to the internal nodes, also when it is not specified.

show a small difference; the second order method, though, gives a more accurate result for the very first time steps.

Comparing the convection-diffusion equation with the conduction equation, it is possible to point out the diffusivity term $\Gamma = \frac{k}{\rho\, c_P}$. This term takes the name of **thermal diffusivity**. The diffusivity of the four materials are $\Gamma_{M_1} = 1.5 \times 10^{-4}$, $\Gamma_{M_2} = 1.1 \times 10^{-4}$, $\Gamma_{M_3} = 1.3 \times 10^{-4}$, $\Gamma_{M_4} = 0.6 \times 10^{-4}$. The diffusivity influence the velocity at which the temperature of wall E propagates through the medium. The consequence of fact that Γ_{M_4} is almost the half of Γ_{M_2} can be seen in fig. 4.2: although a heat flux is entering the north wall and the south wall (which has a lower temperature than E) is farther, the isotherms in M_4 are closer to the east wall.

The three methods demonstrate to be suitable for the study of conduction, especially if the order is II and the time step is small. The code is suitable to be applied in conduction problems regarding the receiver of a CRS.

4.1.2 Smith-Hutton Problem

The Smith-Hutton problem (1982) [66] involves all the terms of the convection-diffusion equation, so it is useful to introduce convection.

Problem definition

The task is to solve the convection-diffusion equation for the prescribed velocity field shown in fig. 4.3. In this case, the steady state of the problem will be analyzed. The flux enters the bottom-left section and

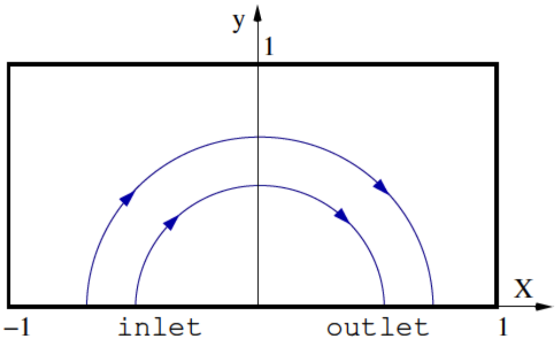

Figure 4.3: Smith-Hutton problem configuration. Figure retrieved from Smith & Hutton (1982) [66].

velocity component	field function
u	$2\,y\,\left(1-x^2\right)$
v	$-2\,x\,\left(1-y^2\right)$

Table 4.3: Velocity field for the Smith-Hutton problem.

goes out in the bottom-right section. Being $\alpha = 10$, the boundary conditions of the property ϕ are

$$\begin{aligned} &\phi = 1 + \tanh\left[\alpha\ (2\,x+1)\right] && y = 0;\ x \in (-1,0) && \text{(inlet)} \\ &\frac{\partial \phi}{\partial y} = 0 && y = 0;\ x \in (0,1) && \text{(outlet)} \\ &\phi = \tanh\ \alpha && && \text{(elsewhere)} \end{aligned}$$

The solutions of the problem depend on a parameter called **Péclet number**, defined as the ratio of convection transport to diffusion transport: $Pe = \frac{\rho\, u\, L}{\Gamma}$. u and L are the characteristic velocities and length of the problem, in this case equal to 1. Results for $Pe = 10,\ 10^3,\ 10^6$ are compared.

Resolution of the governing equations

Integrating in space and applying the divergence theorem B.7, the left-hand side of the convection-diffusion equation 3.1 can be rewritten as

$$\left.\frac{\partial(\rho\,\phi)}{\partial t}\right|_P V_P + \dot{m}_e\,\phi_e - \dot{m}_w\,\phi_w + \dot{m}_n\,\phi_n + \dot{m}_s\,\phi_s \tag{4.8}$$

where $\dot{m}_f = \rho\,\mathbf{u}\,\mathbf{n}\,S_f$ is the mass flow on the surface f ($m_f > 0$ in the positive coordinate direction). The mass equation (eq. 3.2), applying eq. B.1 and multiplying by ϕ_P becomes

$$\phi_P\left.\frac{\partial \rho}{\partial t}\right|_P V_P = \dot{m}_w\,\phi_P - \dot{m}_e\,\phi_P + \dot{m}_s\,\phi_P - \dot{m}_n\,\phi_P \tag{4.9}$$

Applying eq. B.1 to the first term of eq. 4.8 and inserting eq. 4.9, eq. 4.8 becomes

$$\rho\left.\frac{\partial\,(\phi_P)}{\partial t}\right|_P V_P + \dot{m}_e\ (\phi_e - \phi_P) - \dot{m}_w\ (\phi_w - \phi_P) + \dot{m}_n\ (\phi_n - \phi_P) + \dot{m}_s\ (\phi_s - \phi_P) \tag{4.10}$$

The integration in space of the right-hand side of the convection-diffusion equation, instead, leads to

$$\Gamma_e\left.\frac{\partial \phi}{\partial x}\right|_e S_e - \Gamma_w\left.\frac{\partial \phi}{\partial x}\right|_w S_w + \Gamma_n\left.\frac{\partial \phi}{\partial x}\right|_n S_n - \Gamma_s\left.\frac{\partial \phi}{\partial x}\right|_s S_s \tag{4.11}$$

Discretizing in space $\frac{\partial \phi}{\partial x}|_f = \frac{\phi_R - \phi_L}{d_{RL}}$ and substituting $D_f = \Gamma_f\,\frac{S_f}{d_{RL}}$, eq. 4.11 can be expressed as

$$D_e\ (\phi_E - \phi_P) - D_w\ (\phi_P - \phi_W) + D_n\ (\phi_N - \phi_P) - D_s\ (\phi_P - \phi_S) \tag{4.12}$$

The property at the faces ϕ_f is not known, so it must be interpolated by an approximation scheme for convective terms. The schemes investigated in the thesis are five:

Upwind Difference Scheme (UDS) a first order method, unconditionally stable.

Central Difference Scheme (CDS) a second order scheme, conditionally stable.

Second-order Upwind Difference Scheme (SUDS) a second order scheme, conditionally stable.

Quadratic Upstream Interpolation for Convective Kinematics (QUICK) a third order scheme, conditionally stable.

Sharp and Monotonic Algorithm for Realistic Transport (SMART) an adaptive scheme based on QUICK, locally reduced to UDS to be stable.

The High Resolution Schemes (HRSs) (as CDS, SUDS, QUICK, SMART) are introduced using the deferred correction approach: $\dot{m}_f\ (\phi_f - \phi_P)$ is expressed as $\dot{m}_f\ \left(\phi_f^{UDS} - \phi_P\right) + \dot{m}_f\ \left(\phi_f^{HRS} - \phi_f^{UDS}\right)$, such as when the algorithm converges the ϕ_f^{UDS} terms cancel out. Moreover, named F the node such that f stands between F and P, the substitution $\dot{m}_f\ \left(\phi_f^{UDS} - \phi_P\right) = \frac{\dot{m}_f - |\dot{m}_f|}{2}\ (\phi_F - \phi_P)$ is done. Then, eq. 4.10 and eq. 4.12 are combined.

$$\begin{aligned}
&\rho\, \underset{\text{steady state}}{\cancelto{0}{\left.\frac{\partial(\phi_P)}{\partial t}\right|_P}}\, V_P + \frac{\dot{m}_e - |\dot{m}_e|}{2}\ (\phi_E - \phi_P) - \frac{\dot{m}_w + |\dot{m}_w|}{2}\ (\phi_W - \phi_P) + \frac{\dot{m}_n - |\dot{m}_n|}{2}\ (\phi_N - \phi_P) \\
&\quad - \frac{\dot{m}_s - |\dot{m}_s|}{2}\ (\phi_S - \phi_P) = D_e\ (\phi_E - \phi_P) - D_w\ (\phi_P - \phi_W) + D_n\ (\phi_N - \phi_P) - D_s\ (\phi_P - \phi_S) \\
&\quad - \dot{m}_e\ \left(\phi_e^{HRS} - \phi_e^{UDS}\right) + \dot{m}_w\ \left(\phi_w^{HRS} - \phi_w^{UDS}\right) - \dot{m}_n\ \left(\phi_n^{HRS} - \phi_n^{UDS}\right) + \dot{m}_s\ \left(\phi_s^{HRS} - \phi_s^{UDS}\right) \qquad (4.13)
\end{aligned}$$

from which it is possible to obtain the discretization coefficients. All the boundary conditions are trivial to obtain, except the one at the outlet, that must be discretized:

$$\left.\frac{\partial\phi}{\partial y}\right|_P = \frac{\phi_N - \phi_P}{d_{PN}} = 0 \qquad \longrightarrow \qquad \phi_P = \phi_N \qquad (4.14)$$

The equation is resolved with the implicit method: an initial ϕ distribution is guessed, and then values of the mesh are looped until convergence.

Results

The problem is solved with a constant collocated mesh of 21×10 nodes, to be compared with a similarly spaced mesh presented in the reference article [66]. The maps of the flows are presented in fig. C.2. It is important to state that the SMART scheme did not show a stable convergence for the cases $Pe = 10^3$ and $Pe = 10^6$: the value of the nodes close to the region where the gradient of ϕ is high got close to the result and started oscillating around it, so the error could not become lower than convergence parameter. This is probably due to the fact that the SMART scheme is adaptive, and a little variation of ϕ_P could change significantly the equation used by the scheme to make the interpolation. The maps presented, then, are the ones obtained after a significant amount of iterations that made sure that the variables were only having really slight variations around the result. The low incidence of this error is shown in the flow maps.

The values of ϕ at the outlet, obtained with the five different schemes, are compared. The solution for $Pe = 10$, shown in fig. C.3(a), does not present great differences among the convective schemes. For $Pe = 10^3$, instead, the results start to become clearly different. The UDS curve is separated from the group, especially in the points relative to a high gradient. SMART and QUICK schemes stay close to the reference solution, although the latter, together with the SUDS scheme, is responsible for an unphysical ϕ value higher than the inlet maximum.[4] The CDS scheme as well seems to be pretty accurate. For $\phi = 10^6$, this schemes apparently becomes the most accurate, closer than SMART to the reference solution in the points relative to the steepest gradient. The nature shown by the other schemes is the same as for $Pe = 10^3$, although it is accentuated. CDS, despite being only a second order method, could appear as the best choice looking at the outlet; however, the maps of the flow (appendix C) show its inaccuracy because of the spacial oscillations it creates. This phenomenon is called **overshooting**, and it is typical for non-dissipative convection schemes. Looking at the maps, it is clear that the most plausible is the one obtained with SMART: QUICK shows little overshooting as well, while SUDS involves some inaccuracies in the prediction of diffusion such as UDS, though at a lower rate. This phenomenon is called **false diffusion**: the convective term gives a solution that is the one expected with a higher diffusive term Γ (so a lower Péclet number) [67]. False diffusion tends to decrease with the accuracy order of the convective scheme.

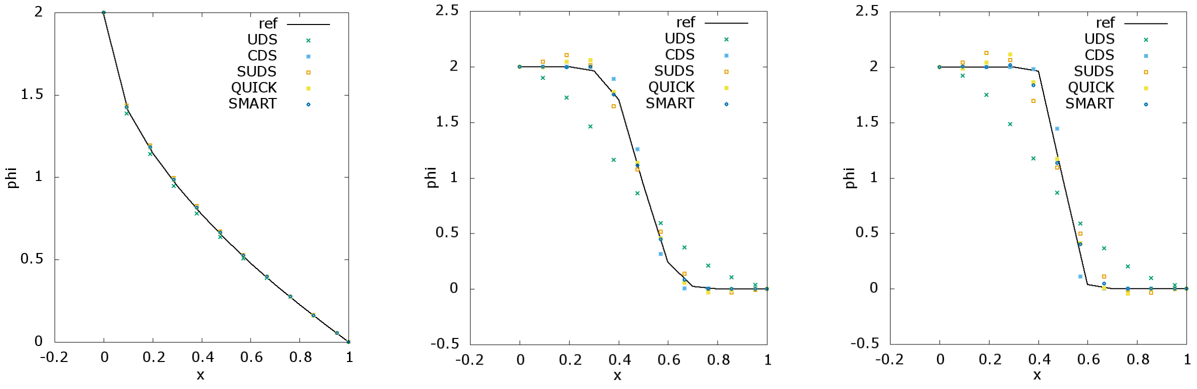

(a) $Pe = 10$ **(b)** $Pe = 10^3$ **(c)** $Pe = 10^6$

Figure 4.4: ϕ distribution at the outlet for different convective schemes and Péclet numbers.

Analyzing the results, the SMART method is chosen for future problem. It shows neither overshooting nor false diffusion, giving at the same time the solution that get closest to the reference. It is important

---

[4] Unphysical because it involves a local decrease in the specific entropy of the flow, in contrast with the third law of thermodynamics: imagine that ϕ is the temperature of the fluid: this would mean that section of the fluid with the highest temperature, surrounded by regions of lower temperature, would increase its temperature in a spontaneous process.

to note, also, that the “instability” of the SMART scheme is not replicated in explicit methods, since the interpolation is performed only on already-known node values.

The results obtained with the SMART scheme show a substantial difference: when the Péclet number is low ($Pe = 10$), diffusion is dominant. Although convective transport is clear, diffusive transport substantially changes the distribution of the variable ϕ along its flow. For higher Pe, convective transport dominates, and the flow distribution almost follows the velocity distribution.

The Smith-Hutton problem is a relatively simple configuration: the velocity field is known, and does not depend on the convective term of the equation. In the reality, the velocity field is obtained with the momentum equation, that involves a nonlinear term dependent on the velocity itself. Whenever the velocity grows, the influence of this term increases and the complexity of the problem as well. The diffusive term acts as a dissipative force for the velocity; whenever this term becomes too little compared to the convective term, this dissipation becomes less influent and turbulence arises (due to the nonlinearity of the equation). This transition will be discussed and explained in the next section, where the convection-diffusion equation will be applied to the governing equations of fluid dynamics.

4.2 Laminar Flow

Laminar flows are characterized by relatively high momentum diffusion and low momentum convection. Hence, no eddies are created, since the kinetic energy of the fluid is damped by the diffusive term at a global scale. Laminar flow is always present at a local scale next to solid boundaries: in those regions the velocity is null due to wall adhesion, so the convective term disappears and the diffusive becomes significant.

Laminar flow is presented with two historically relevant problems: the **driven cavity** problem and the **differentially heated cavity** (sometimes referred as “thermally driven cavity”).

4.2.1 Driven Cavity – Laminar Flow

The driven cavity problem has been one of the first and most studied problems for the computational resolution of the momentum equation because of its simplicity and versatility. The 2D case is analyzed and compared with the reference article of Ghia, Ghia & Shin (1982) [68].

Problem definition

An infinitely-tall cavity having a square horizontal section of side L contains an incompressible fluid at $p = p_0$. At the time $t = 0$, one of the lateral walls starts moving at the velocity $u = U_0$. A xy section of the cavity is shown in fig. 4.5. The goal is to solve the velocity-pressure field of the fluid. The

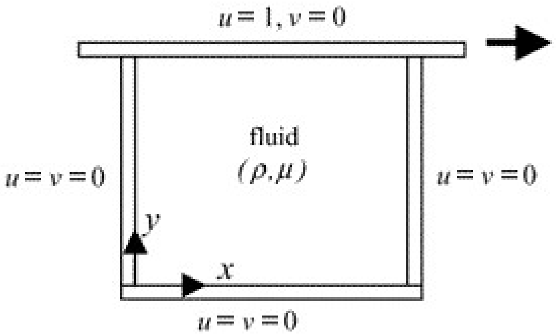

Figure 4.5: Horizontal section of the driven cavity. Figure retrieved from Marchi, Suero & Araki (2009) [69].

Re		
100	400	1000
3200	5000	7500

Table 4.4: Reynolds numbers analyzed.

solution depends on the **Reynolds number**, defined as $Re = \frac{\rho\, U_0\, L}{\mu}$. The Reynolds numbers is changed modifying the side of the cavity (the thermophysical properties of the fluid do not change).

Resolution of the governing equations

The equations that govern this problem are the mass conservation equation and the momentum equation. The method used to solve them is called **Fractional Step Method (FSM)**, firstly described by Chorin (1968) [70]; this method is known for its simplicity and accuracy.

The momentum conservation equation for incompressible flows 3.10 is analyzed. For simplicity, the convective and diffusive terms are grouped in the function $\mathbf{R}(\mathbf{u}) = -\rho\, (\mathbf{u} \cdot \nabla)\, \mathbf{u} + \mu\, \nabla^2 \mathbf{u}$.

$$\rho\, \frac{\partial \mathbf{u}}{\partial t} = \mathbf{R}(\mathbf{u}) - \nabla p \tag{4.15}$$

Eq. 3.8 and 3.10 are integrated in time. The mass equation is treated implicitly. The pressure-dependent term of the momentum equation is integrated implicitly, while the convective-diffusive term $\mathbf{R}(\mathbf{u})$ is integrated with a second order explicit Adams-Bashforth method: $\mathbf{R}\left(\mathbf{u}^{n+1/2}\right) = \frac{3}{2}\,\mathbf{R}(\mathbf{u}^n) - \frac{1}{2}\,\mathbf{R}\left(\mathbf{u}^{n-1}\right)$.

$$\nabla \cdot \mathbf{u}^{n+1} = 0 \tag{4.16}$$

$$\rho\, \frac{\mathbf{u}^{n+1} - \mathbf{u}^n}{\Delta t} = \frac{3}{2}\,\mathbf{R}(\mathbf{u}^n) - \frac{1}{2}\,\mathbf{R}\left(\mathbf{u}^{n-1}\right) - \nabla p^{n+1} \tag{4.17}$$

The FSM is then applied. It consists in the definition of an auxiliary vector $\mathbf{u}^p$, called *predictor velocity*; the vector is a projection of $\mathbf{u}^{n+1}$ and it can be seen as an intermediate step between $\mathbf{u}^n$ and $\mathbf{u}^{n+1}$.

$$\mathbf{u}^p := \mathbf{u}^{n+1} + \frac{\Delta t}{\rho}\, \nabla p^{n+1} \tag{4.18}$$

The existence and uniqueness of $\mathbf{u}^p$ is guaranteed by the Helmholtz decomposition theorem, that states that any vector field $\mathbf{w}$ can be uniquely decomposed in a pure gradient field and a divergence-free vector:

$$\mathbf{w} = \mathbf{a} + \nabla\varphi \tag{4.19}$$

In this case, $\mathbf{a} = \mathbf{u}^{n+1}$ and $\nabla\varphi = \frac{\Delta t}{\rho}\nabla p^{n+1}$; the condition $\nabla\cdot\mathbf{a} = 0$ comes from eq. 4.16. $\mathbf{u}^{n+1}$ is extracted from eq. 4.18 and inserted in eq. 4.17:

$$\rho\,\frac{\mathbf{u}^p - \cancel{\frac{\Delta t}{\rho}\nabla p^{n+1}} - \mathbf{u}^n}{\Delta t} = \frac{3}{2}\,\mathbf{R}\left(\mathbf{u}^n\right) - \frac{1}{2}\,\mathbf{R}\left(\mathbf{u}^{n-1}\right) - \cancel{\nabla p^{n+1}} \tag{4.20}$$

The divergence of eq. 4.18 is taken.

$$\nabla\cdot\mathbf{u}^p = \cancelto{0}{\nabla\cdot\mathbf{u}^{n+1}} + \frac{\Delta t}{\rho}\,\nabla\cdot\nabla p^{n+1} \tag{4.21}$$

It is then possible to express the three unknowns $\mathbf{u}^p$, p^{n+1}, $\mathbf{u}^{n+1}$ with three equations:

$$\mathbf{u}^p = \mathbf{u}^n + \frac{\Delta t}{\rho}\left[\frac{3}{2}\,\mathbf{R}\left(\mathbf{u}^n\right) - \frac{1}{2}\,\mathbf{R}\left(\mathbf{u}^{n-1}\right)\right] \tag{4.22}$$

$$\nabla^2 p^{n+1} = \nabla\cdot\mathbf{u}^p \tag{4.23}$$

$$\mathbf{u}^{n+1} = \mathbf{u}^p - \frac{\Delta t}{\rho}\,\nabla p^{n+1} \tag{4.24}$$

Eq. 4.22 is integrated over the staggered volume of the components of the velocity u and v (the projections on the x and y-axis respectively). The procedure for u is shown (it is analogue for v). u^n is moved to the left-hand side of the equation, which is integrated:

$$\int_{V_{P_x}} \left(u^p - u^n\right)\,dV = \left(u^p - u^n\right)\,V_{P_x} \tag{4.25}$$

Named R_u the projection of $\mathbf{R}\left(\mathbf{u}\right)$ on the x-axis, its integration over the volume becomes

$$\begin{aligned}\int_{V_{P_x}} R_u\,dV &= \int_{V_{P_x}} \left[-\rho\,\left(\mathbf{u}\cdot\nabla\right)\,u + \mu\,\nabla^2\,u\right]\,dV \\ &\underset{B.2,\;B.4,\;B.7}{=} -\int_{S_{f_x}} \left(\rho\,\mathbf{u}\right)\,u\cdot\mathbf{n}\,dS + \mu\int_{S_{f_x}} \nabla u\cdot\mathbf{n}\,dS\end{aligned} \tag{4.26}$$

Eq. 4.25 and 4.26 are inserted in eq. 4.22, then the latter is discretized:

$$u_P^p = u_P^n + \frac{\Delta t}{\rho\,V_{P_x}}\left(\frac{3}{2}\,R_u^{int,\,n} - \frac{1}{2}\,R_u^{int,\,n-1}\right) \tag{4.27}$$

where

$$R_u^{int} = -\left\{\left[(\rho\, u_e)\ u_e\ - (\rho\, u_w)\ u_w\right] S_w + \left[(\rho\, v_n)\ u_n\ - (\rho\, v_s)\ u_s\right] S_{s_x}\right\} \\ + \mu \left[\left(\frac{u_E - u_P}{d_{PE}} - \frac{u_P - u_W}{d_{PW}}\right) S_w + \left(\frac{u_N - u_P}{d_{PN}} - \frac{u_P - u_S}{d_{PS}}\right) S_{s_x}\right] \tag{4.28}$$

Eq. 4.23 is integrated over the volume V_P and the divergence theorem is used:

$$\int_{S_f} \nabla p^{n+1} \cdot \mathbf{n}\, dS = \int_{S_f} \mathbf{u}^p \cdot \mathbf{n}\, dS \tag{4.29}$$

The equation discretized becomes

$$\left(\frac{p_E^{n+1} - p_P^{n+1}}{d_{PE}} - \frac{p_P^{n+1} - p_W^{n+1}}{d_{PW}}\right) S_w + \left(\frac{p_N^{n+1} - p_P^{n+1}}{d_{PN}} - \frac{p_P^{n+1} - p_S^{n+1}}{d_{PS}}\right) S_s = \\ \frac{1}{\Delta t}\ \left[(\rho\, u_P^p - \rho\, u_W^p)\ S_w + (\rho\, v_P^p - \rho\, v_S^p)\ S_s\right] \tag{4.30}$$

from which it is possible to extract the convergence coefficients. Finally, eq. 4.24 is discretized:

$$u_P^{n+1} = u_P^p - \frac{\Delta t}{\rho}\, \frac{p_E^{n+1} - p_P^{n+1}}{d_{PE}} \tag{4.31}$$

The resolution of v_P^{n+1} is analogous. Having all the discretized equations, the algorithm to find the next time step is the following: u_P^p and v_P^p are found for every P by eq. 4.27; the pressures at $n+1$ are found by eq. 4.30; the velocity field, composed of u_P^{n+1} and v_P^{n+1}, is found by eq. 4.31.

Properties at the faces are calculated with different methods. Mass flows (in the form of $\rho\, u_f$) are evaluated with a mass balance over the control-volume surfaces. The velocities, appearing in the convective term, are interpolated with the SMART scheme.[5]

At the walls, where the relative velocity between fluid and solid is null, the fluid adheres perfectly: therefore, the pressure is hydrostatic; since the z-axis is fixed, the gradient towards the direction normal to the wall is zero ($p_P = p_{NB}$).

Defined d_{ew} and d_{ns} as the height and the length of each volume, the set CFL conditions become

$$\left.\begin{array}{l} \Delta t_c = 0.35\ \min\left(\frac{\sqrt{d_{ew}\, d_{ns}}}{|\mathbf{u}|}\right) \\ \Delta t_d = 0.08\ \min\left(\frac{\rho\, d_{ew}\, d_{ns}}{\mu}\right) \end{array}\right\} \quad \Delta t = \min\left(\Delta t_c,\, \Delta t_d\right) \tag{4.32}$$

where Δt_c is the convective time-step and Δt_d is the diffusive time-step. Δt_c depends on the velocity, so it has to be recalculated at every time-step.

---

[5] For the nodes next to the boundaries, the CDS scheme is used. In fact, it only uses the two nodes next to the face. SMART uses a couple of additional farther nodes: at boundaries, one of them is not available.

Results

A 128×128 velocity-staggered mesh is used. The stream-function and vorticity steady-state maps for the different Re (fig. C.5, C.6) show the same characteristics of the ones presented in the reference article. Regarding the stream function, in all the cases a large eddy that touches the four walls is created; at the top, its velocity is equal to the moving wall, making the eddy spin clockwise. In $Re = 100$, there are two counterclockwise secondary eddies of approximately the same measure in the two bottom corners. The center of the main eddy is located between the geometric center of the cavity and the top-right corner. For $Re = 400, 1000$ both the secondary eddies grow, being the bottom-right larger than the bottom-left. The center of the main eddy shifts toward the center. These evolutions continue for larger eddies. At $Re = 3200$ another counterclockwise secondary eddy generates at the top-left corner. At $Re = 7500$, finally, the bottom-right eddy splits in two smaller eddies; the smallest, located in the corner, does not interact with the main eddy, and rotates in the opposite direction of the other. Regarding the vorticity, as Re rises the higher and higher gradients are created.

The two components u and v of the velocity are compared – respectively along the vertical and horizontal line through the geometric center. The results agree with the reference study, as shown by fig. C.7 and C.8. For these Reynolds cases, diffusion plays a significant role. Looking at the maps, it is possible to see that the relative velocity between fluid and wall is null; then the absolute value of u and v increases until it reaches a maximum, and falls again. Close to the walls, diffusion is highly dominant. As Re increases, the location of the maximum absolute velocity shifts toward the wall: the high-diffusive region, where energy is dissipated, becomes increasingly thin. However, up to $Re = 7500$, no turbulence appears.

Looking at the results, it is clear that the method is robust: comparing fig. C.5(c) with fig. C.5(d), fig. C.6(c) with fig. C.6(d), fig. C.7(c) with fig. C.7(d) and fig. C.8(c) with fig. C.8(d), it is possible to acknowledge that a mesh of 128×128 nodes is sufficient for a consistent analysis of the problem. The SMART scheme made no errors with an explicit method, as expected, and the FSM resulted to be a correct tool to resolve mass and momentum conservation equations.

4.2.2 Differentially Heated Cavity – Laminar Flow

The Differentially Heated Cavity (DHC) is another famous benchmark problem for CFD. Its geometric and boundary-condition simplicity is the same as the driven cavity, with the introduction of the energy equation due to heat transfer. The DHC problem involves all the equations needed to describe the natural convection in a external receiver of a CRS plant, with the advantage that they can be studied with a much simpler configuration. A first, simple case of 2D DHC under the Boussinesq approximation is compared with two reference articles of De Vahl Davis (1983) [71, 72] to validate the computational algorithm created. At a later stage, the dependence of air properties on the temperature is made explicit. Finally, the computation is extended to the three dimensions.

4.2.2.A Boussinesq fluid, 2D flow

Problem definition

A Boussinesq fluid of Prandtl number $Pr = 0.71$ is located in a square cavity.[6] The top and the bottom boundaries are perfectly insulated, the west is kept at the temperature T_h and the east at T_c.

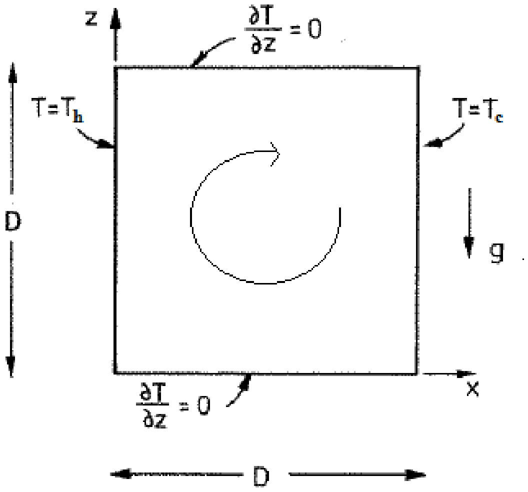

Figure 4.6: Differentially Heated Cavity, section of the vertical plane. Figure edited from De Vahl Davis & Jones (1983) [71].

The goal is to solve pressure, velocity and temperature fields of the fluid. The solution of the problem depends on the Rayleigh number $Ra := Gr\,Pr = \frac{\rho^2\,\beta\,g\,(T_h - T_c)\,D^3}{\mu^2}\,Pr$, being D the characteristic length of the flow (in this case, the side of the square).[7] Results are analyzed for $Ra = 10^3,\,10^4,\,10^5,\,10^6$.

Resolution of the governing equations

The procedure of the resolution of the driven cavity problem is take as reference to explain the resolution of the equations of the DHC problem, since they are similar and the FSM is used in this case as well. Since the DHC lateral walls are vertical, the notation is slightly different:

- the north n and south s references become top t and bottom b references;
- the y-axis becomes z, and the component of the velocity v becomes w.

---

[6] The Prandtl number is the ratio of viscous diffusion to thermal diffusion. It is defined as $Pr = \frac{\mu\,c_P}{k}$.

[7] Compare with eq. 2.15.

According to the Boussinesq approximation, the momentum equation takes the form of eq. 3.13. The parameter $\mathbf{R}\left(\mathbf{u}\right)$ is adjusted to the following form:

$$\mathbf{R}\left(\mathbf{u}\right) = -\rho_0 \, \left(\mathbf{u} \cdot \nabla\right) \, \mathbf{u} + \mu \, \nabla^2 \mathbf{u} - \rho_0 \, \beta \, \left(T - T_0\right) \, \mathbf{g} \tag{4.33}$$

Proceeding with the FSM, the space integration of $\mathbf{R}\left(\mathbf{u}\right)$ leads to

$$\begin{cases} R_u^{int} = R_u^{int,\,dc} \\ R_w^{int} = R_w^{int,\,dc} + \rho_0 \, \beta \, \left(T_t^{n+1} - T_0\right) \, g \, V_{P_z} \end{cases} \tag{4.34}$$

where $R_u^{int,\,dc}$ denotes the R_u^{int} of the driven cavity problem.

The energy equation for a Boussinesq fluid is introduced, having the form expressed by eq. 3.14. Using eq. B.2 and eq. 3.8, it is possible to write

$$\rho_0 \, \frac{\partial T}{\partial t} = -\rho_0 \, \left[\nabla \cdot \left(\mathbf{u} \, T\right)\right] + \frac{k}{c_P} \, \nabla^2 T = R\left(T\right) \tag{4.35}$$

where $R(T)$ represents the right-hand side of the equation rearranged. The energy equation is discretized with the second-order explicit Adams-Bashforth method:

$$\rho_0 \, \frac{T^{n+1} - T^n}{\Delta t} = R\left(T^{n+1/2}\right) = \frac{3}{2} \, R\left(T^n\right) - \frac{1}{2} \, R\left(T^{n-1}\right) \tag{4.36}$$

The equation is then integrated within the control volume V_P:

$$\rho_0 \, \frac{T_P^{n+1} - T_P^n}{\Delta t} \, V_P = \frac{3}{2} \, R_T^{int,\,n} - \frac{1}{2} \, R_T^{int,\,n-1} \tag{4.37}$$

R_T^{int} is the result of the volume integration of the term $R(T)$:

$$\begin{aligned} R_T^{int} &= -\,\rho_0 \int_{V_P} \nabla \cdot \left(\mathbf{u} \, T\right) \, dV + \frac{k}{c_P} \int_{V_P} \nabla^2 T \, dV \\ &\underset{B.7,\; B.4}{=} -\,\rho_0 \int_{S_P} \mathbf{u} \, T \, \mathbf{n} \, dS + \frac{k}{c_P} \int_{S_P} \nabla T \, \mathbf{n} \, dS \\ &\underset{\partial x \to \Delta x}{=} -\,\rho_0 \, \left[\left(u_P \, T_e - u_W \, T_w\right) \, S_w + \left(w_P \, T_t - w_B \, T_b\right) \, S_b\right] \\ &\qquad + \frac{k}{c_P} \, \left[\left(\frac{T_E - T_P}{d_{PE}} - \frac{T_P - T_W}{d_{PW}}\right) \, S_w + \left(\frac{T_T - T_P}{d_{PT}} - \frac{T_P - T_B}{d_{PB}}\right) \, S_b\right] \end{aligned}$$

Following eq. 4.37, the temperature of the control volume can be expressed as

$$T_P^{n+1} = T_P^n + \frac{\Delta t}{\rho_0 \, V_P} \, \left(\frac{3}{2} \, R_T^{int,\,n} - \frac{1}{2} \, R_T^{int,\,n-1}\right) \tag{4.38}$$

The boundary conditions are expressed for u, w, p and T. The fluid adheres perfectly to the walls

$(u,\, w = 0)$. Since the velocity is null, the pressure distribution is hydrostatic: the momentum equation reduces to $0 = -\nabla p - \rho_0\, \beta\; (T - T_0)\; \mathbf{g}$;[8] projected on the x and z axes it becomes:

$$\frac{\partial p}{\partial x} = 0, \qquad \frac{\partial p}{\partial z} = \rho_0\, \beta\; (T - T_0)\; g \tag{4.39}$$

The discretization of $\frac{\partial p}{\partial z}$ at the top and bottom walls leads to

$$\frac{p_T^{n+1} - p_P^{n+1}}{d_{PT}} = \rho_0\, \beta\; \left(T_P^{n+1} - T_0\right)\; g, \qquad \frac{p_P^{n+1} - p_B^{n+1}}{d_{PB}} = \rho_0\, \beta\; \left(T_P^{n+1} - T_0\right)\; g \tag{4.40}$$

from which it is possible to extract the discretization coefficients. The boundary conditions for the temperature, instead, are: at the west $T_P^{n+1} = T_h$, at the east $T_P^{n+1} = T_c$, at the top $T_P^{n+1} = T_B^{n+1}$, at the bottom $T_P^{n+1} = T_T^{n+1}$. Again, the discretization coefficients can be extracted.

Since the heat equation is discretized explicitly, an additional CFL condition for the energy equation is set:

$$\Delta t_k = 0.08\ \min\left(\frac{d_{ew}\, d_{ns}}{k/\left(\rho_0\, c_P\right)}\right) \tag{4.41}$$

Hence, the final time step is $\Delta t = \min\left(\Delta t_c,\, \Delta t_d,\, \Delta t_k\right)$.

Results

The study is performed for air at the reference temperature $T_0 = 300$ K: the air properties are taken at this temperature from Eckert & Drake (1987) [57]. The Prandtl number of the fluid is $Pr = 0.708$, essentially equal to the reference case.[9]

The west temperature is $T_h = 305$, while the east is $T_c = 295$.[10] This small ΔT guarantees the possibility to use the Boussinesq approximation. At $t = 0$, the fluid has a temperature of 295 K (as the cold wall); although in the study only the steady-state results are compared with the benchmark solution, this configuration was chosen to demonstrate the suitability of the code when applied to transients.

The meshes used are the same of the driven cavity problem. The number of internal nodes is 20×20 for $Ra = 10^3$, 40×40 for $Ra = 10^4$ and 60×60 for $Ra = 10^5,\, 10^6$. These numbers are the same used in the meshes of De Vahl Davis; as it will be shown in the analysis of the results, they are enough fine to supply correct solutions to the problem.

Nine parameters are analyzed: the absolute non-dimensional vorticity at the geometric center ψ_{mid}, the maximum absolute non-dimensional vorticity ψ_{max} and its location, the maximum non-dimensional horizontal velocity u_{mid} on the vertical mid-plane and its coordinates $x\,, z$, the maximum non-dimensional

---

[8] The second derivatives of the velocity, that appear in the Laplacian of the momentum equation, are not necessarily equal to zero. However, they are assumed to be negligible compared to the buoyancy forces.

[9] The decision of using the real air properties, that involves a slightly different Prandtl, is taken to be able to perform a more consistent comparison with the non-Boussinesq fluid that will be analyzed in the next sections.

[10] Since the difference of the temperature of the two walls is relatively low, thermal radiation is neglected.

vertical velocity w_{mid} on the horizontal mid-plane and its location, the average Nusselt number $\overline{Nu}$, the Nusselt number along the vertical mid-plane $Nu_{1/2}$, the Nusselt number Nu_0 at the hot wall and the maximum and the minimum Nusselt numbers Nu_{max}, Nu_{min} along the hot wall. The reference dimensional parameters are the height H, the temperature $\Delta T = T_h - T_c$, the density ρ_0 and the thermal diffusivity $\alpha = \frac{mu}{\rho\, c_P}$. The Nusselt number, which represents the non-dimensional heat transfer, is defined locally as

$$Nu = -\frac{\partial \hat{T}}{\partial \hat{x}} + \hat{u}\,\hat{T} \tag{4.42}$$

where $\hat{T} = \frac{T - T_c}{T_h - T_c}$, $\hat{x} = \frac{x}{D}$ and $\hat{u} = \frac{u\, D\, \rho_0\, c_P}{k}$ denote respectively the non-dimensional temperature, x coordinate and horizontal velocity. Nu_0 and $Nu_{1/2}$ are obtained by integrating the local Nusselt along the non-dimensional vertical line:

$$Nu_0 = -\int_0^1 \left(\frac{\partial \hat{T}}{\partial \hat{x}} + \hat{u}\,\hat{T} \right)\Bigg|_{\hat{x}=0} d\hat{z}, \qquad Nu_{1/2} = -\int_0^1 \left(\frac{\partial \hat{T}}{\partial \hat{x}} + \hat{u}\,\hat{T} \right)\Bigg|_{\hat{x}=1/2} d\hat{z} \tag{4.43}$$

Tab. 4.5 below shows a comparison between the benchmark solution [71] and the results obtained. The reference paper uses a second-order Finite Difference Method (FDM) based on the false transient method.

Table 4.5: Boussinesq 2D DHC – comparison between the results obtained and the benchmark values.

	Benchmark solution Ra				Results obtained Ra			
	10^3	10^4	10^5	10^6	10^3	10^4	10^5	10^6
$\lvert\psi_{mid}\rvert$	1.174	5.071	9.111	16.32	1.196	5.089	9.158	16.710
$\lvert\psi\rvert_{max}$	—	—	9.612	16.750	—	—	9.659	17.108
x, z	—	—	0.285, 0.601	0.151, 0.547	—	—	0.283, 0.600	0.150, 0.550
u_{max}	3.649	16.178	34.73	64.63	3.676	16.159	34.879	65.860
z	0.813	0.823	0.855	0.850	0.825	0.813	0.858	0.842
w_{max}	3.697	19.617	68.59	219.36	3.751	19.642	68.313	219.49
x	0.178	0.119	0.066	0.0379	0.175	0.113	0.0583	0.0417
$\overline{Nu}$	1.118	2.243	4.519	8.800	1.124	2.259	4.564	9.095
$Nu_{1/2}$	1.118	2.243	4.519	8.799	1.124	2.259	4.564	9.095
Nu_0	1.117	2.238	4.509	8.817	1.159	2.266	4.566	9.095
Nu_{max}	1.505	3.528	7.717	17.925	1.638	3.589	7.931	19.372
z	0.092	0.143	0.081	0.0378	0.025	0.138	0.075	0.025
Nu_{min}	0.692	0.586	0.729	0.989	0.704	0.584	0.723	0.952
z	1	1	1	1	0.975	0.988	0.992	0.992

The results obtained are essentially consistent with the benchmark solution for every parameter at every Ra. Comparing them to the work of the other authors resumed in the document, it is possible to see that all the results lie within the range of solutions of each variable. The differences can be due to the different method used, mesh configuration and in a minor way the different Pr number. The stream-function, the vorticity and the temperature field maps – shown in fig. C.9, C.10 and C.11 respectively – are in accordance with the reference article as well. The isotherms of fig. C.11 for $Ra = 10^3$ are almost vertical, although the hot fluid tends to concentrate on the higher part of the cavity. The streamlines suggest that the fluid is circulating homogeneously throughout the whole cavity. As the Ra grows, the hot fluid tends to stratify: hot air rises, due to the buoyancy forces, while cold air maintains near the bottom of the cavity. For $Ra = 10^4$, the flow stops moving in circles: near the center, the fluid flows around an eight-like shape; this helps to create two zones with $|\psi|_{max}$. The reason why the fluids move around this path is given by the fact that heated air rises until it encounters almost equally-hot air floating that does not naturally descends. Therefore, the heated air has to deviate to get inserted in the layers of the fluid that have its same temperature.

In the cases of $Ra = 10^5, 10^6$ a layer characterized by a high temperature gradient can be pointed out. This layer is characterized by high diffusion and low convection. The velocity within the layer is low: being null at the wall, it rapidly rises to a maximum and then descends gradually. The maximums shift towards the walls as the Rayleigh number rises: this can be viewed in fig. C.12 and tab. 4.5. The location of w_{max} shows a correlation with the fourth power of the Rayleigh number $\Delta x \propto Ra^{1/4}$.

Meshes finer than the ones used to show the results in tab. 4.5 were tried. The values at the steady state conditions were slightly different, but no significant alteration was found. The velocity and the temperature along the mid-axes were compared as well, and the curves were overlapping.

4.2.2.B Fluid with variable thermophysical properties, 2D flow

In this section, air is no longer considered as a Boussinesq fluid. Its thermophysical properties are calculated by means of correlations extracted from Eckert & Drake (1987) [57], and reported in sec. B.5. The great advantage of this approach is that its validity is guaranteed for a much wider range of ΔT: the correlations used are valid from 100 K to 1300 K, a range expected to cover all the temperatures arising in the natural convection in CRSs.

Although the Boussinesq approximation is no longer used, density is still assumed to be constant except in the buoyancy forces: the assumption of incompressible flow, that makes eq. 3.8 be still valid, permits to maintain the FSM approach. The fact that the fluid can be assumed as incompressible is a consequence of the fact that the natural convection analyzed involves low Mach numbers ($Ma < 0.3$).

Although eq. B.17a shows a dependence on the pressure, the Boussinesq approach showed that for the problem studied $\frac{p_{max}-p_{amb}}{p_{amb}} \approx 10^{-8}$ (at steady state). Therefore, pressure variations for the calculation of density can be neglected: ambient pressure is considered as the input of the density correlation (that must be taken into account in the calculation of ρ in the buoyancy forces).

The specific heat, as shown by eq. B.17c, shows only a slight dependence on the temperature. In order to reduce the computational cost of the problem and avoid the calculation of the property for every node, c_P is considered constant and calculated at T_0.

Resolution of the governing equations

The momentum equation for the fluid considered is expressed by eq. 3.9. The viscous term is elaborated:

$$\nabla \cdot \left[\mu \, \left(\nabla \mathbf{u} + \nabla \mathbf{u}^{\mathrm{T}}\right)\right] = \nabla \cdot \left[\mu \begin{pmatrix} \frac{\partial u}{\partial x} & \frac{\partial u}{\partial z} \\ \frac{\partial w}{\partial x} & \frac{\partial w}{\partial z} \end{pmatrix} + \mu \begin{pmatrix} \frac{\partial u}{\partial x} & \frac{\partial w}{\partial x} \\ \frac{\partial u}{\partial z} & \frac{\partial w}{\partial z} \end{pmatrix}\right] \underset{proj.}{=} \begin{cases} \nabla \cdot (\mu \, \nabla u) + \nabla \cdot \left(\mu \, \frac{\partial \mathbf{u}}{\partial x}\right) \\ \nabla \cdot (\mu \, \nabla w) + \nabla \cdot \left(\mu \, \frac{\partial \mathbf{u}}{\partial z}\right) \end{cases} \tag{4.44}$$

The x-axis is analyzed: the volume integration of the x-axis projection of eq. 4.44 leads to

$$\int_{V_{P_x}} \nabla \cdot \left[\mu \left(\nabla u + \frac{\partial \mathbf{u}}{\partial x}\right)\right] dV \underset{B.7}{=} \int_{S_x} \left[\mu \left(\nabla u + \frac{\partial \mathbf{u}}{\partial x}\right)\right]\bigg|_{f_x} \mathbf{n} \, dS = \int_{S_x} \left[\mu \left(2 \, \frac{\partial u}{\partial x}, \, \frac{\partial u}{\partial z} + \frac{\partial w}{\partial x}\right)\right]\bigg|_{f_x} \mathbf{n} \, dS \tag{4.45}$$

The term is rearranged and discretized

$$\begin{aligned} & 2 \left(\mu_{e_x} \, \frac{\partial u}{\partial x}\bigg|_{e_x} - \mu_{w_x} \, \frac{\partial u}{\partial x}\bigg|_{w_x}\right) S_w + \left[\mu_{t_x} \, \left(\frac{\partial u}{\partial z} + \frac{\partial w}{\partial x}\right)\bigg|_{t_x} - \mu_{b_x} \, \left(\frac{\partial u}{\partial z} + \frac{\partial w}{\partial x}\right)\bigg|_{b_x}\right] S_{b_x} \\ = & \left(\mu_E \, \frac{u_E - u_P}{d_{PE_x}} - \mu_P \, \frac{u_P - u_W}{d_{PW_x}}\right) S_w + \left[\mu_{te} \, \left(\frac{u_T - u_P}{d_{PT}} + \frac{w_E - w_P}{d_{PE}}\right) - \mu_{be} \, \left(\frac{u_P - u_B}{d_{PB}} + \frac{w_{BE} - w_B}{d_{PE}}\right)\right] S_{b_x} \end{aligned} \tag{4.46}$$

The quantities μ_{te} and μ_{be} represent the viscosity calculated with the correlation for the temperatures T_{te} and T_{be} respectively at the top-east and bottom-east corner of the control volume P.[11] The considerations made for the x-axis are valid for the z-axis.

Eq. 4.46 is then inserted in eq. 4.28. The rest of equations are the same of the Boussinesq fluid study, except that $R_w^{int} = R_w^{int,\,dc} - \rho \, g \, V_{P_x}$, where ρ is now calculated with corr. B.17a.

The diffusive term of the Nusselt number $-\frac{\partial \hat{T}}{\partial \hat{x}}$ is now defined as $-\hat{k} \, \frac{\partial \hat{T}}{\partial \hat{x}}$, where $\hat{k} = \frac{k}{k_0}$ is the non-dimensional conductivity.

Results

The results of the four Rayleigh cases are compared with the Boussinesq fluid study in tab. 4.6. The results are almost the same: the only visible difference can be found in the coordinates of $|\psi|_{max}$. However, this is a “false” difference: as shown previously in fig. C.9(b), the stream function has essentially two maximums; in this case, the coordinates of the other maximum were chosen.[12] The maps are virtually equal to the previous ones.

An additional simulation is performed to study a DHC with large temperature differences ($\Delta T =$ 720 K), to verify the variable thermophysical properties approach outside the small range of temperatures

---

[11] T_{te} is calculated with a double interpolation on the x and y direction performed with the SMART scheme.

[12] It is possible, though, that a certain grade of symmetry has been lost, since the properties now are variable. For this restricted range of temperatures, though, the maps still appear symmetric.

Table 4.6: Variable thermophysical properties 2D DHC – comparison with Boussinesq fluid results.

	Boussinesq fluid Ra				Variable thermophysical properties Ra			
	10^3	10^4	10^5	10^6	10^3	10^4	10^5	10^6
$\lvert\psi_{mid}\rvert$	1.196	5.089	9.158	16.710	1.197	5.090	9.157	16.707
$\lvert\psi\rvert_{max}$	—	—	9.659	17.108	—	—	9.663	17.109
$x,\ z$	—	—	0.283, 0.600	0.150, 0.550	—	—	0.283, 0.600	0.850, 0.450
u_{max}	3.676	16.159	34.879	65.860	3.664	16.099	34.885	65.686
z	0.825	0.813	0.858	0.842	0.825	0.813	0.858	0.842
w_{max}	3.751	19.642	68.313	219.49	3.720	19.532	68.000	219.19
x	0.175	0.113	0.0583	0.0417	0.175	0.113	0.0583	0.0417
$\overline{Nu}$	1.124	2.259	4.564	9.095	1.124	2.259	4.564	9.095
$Nu_{1/2}$	1.124	2.259	4.564	9.095	1.123	2.259	4.564	9.095
Nu_0	1.159	2.266	4.566	9.095	1.160	2.266	4.566	9.094
Nu_{max}	1.638	3.589	7.931	19.372	1.651	3.594	7.953	19.438
z	0.025	0.138	0.075	0.025	0.025	0.138	0.075	0.025
Nu_{min}	0.704	0.584	0.723	0.952	0.707	0.589	0.726	0.955
z	0.975	0.988	0.992	0.992	0.975	0.988	0.992	0.992

previously analyzed. The results using the Boussinesq and the non-Boussinesq approach are compared with Le Quéré et al. (2005) [2] and found out to be consistent, as shown by tab. 4.7.

Table 4.7: Nusselt at the hot wall – 2D DHC with a large temperature difference using the variable thermophysical properties approach. Comparison with Le Quéré et al.

	Lé Queré		Results obtained	
	Bouss	non-Bouss	Bouss	non-Bouss
Nu_0	1.117	8.817	1.159	9.095

4.2.2.C Fluid with variable thermophysical properties, 3D flow

The study performed in sec. 4.2.2.B is extended to the three dimensions. The secondary horizontal component of the velocity v and the nodes N and S are introduced. A cubic cavity is considered. The north and south walls are assumed to be adiabatic, and the boundary conditions become $T_P^{n+1} = T_S^{n+1}$ and $T_P^{n+1} = T_N^{n+1}$ respectively.

The governing equations are not analyzed in detail, since their final form is unaltered respect the 2D case, except that the additional discretization along the y-axis is included. After defining $\Delta x := \sqrt[3]{V_P}$, the CFL conditions are reformulated in the following form:

$$\left.\begin{aligned} \Delta t_c &= 0.35\ \min\left(\frac{\Delta x}{|\mathbf{u}|}\right) \\ \Delta t_d &= 0.08\ \min\left(\frac{\rho\,\Delta x^2}{\mu}\right) \\ \Delta t_k &= 0.08\ \min\left(\frac{\Delta x^2}{k/(\rho_0\,c_P)}\right) \end{aligned}\right\} \quad \Delta t = \min\left(\Delta t_c,\ \Delta t_d,\ \Delta t_k\right) \tag{4.47}$$

Mesh definition

The numerical methodology is the same of the 2D case except for the mesh definition. The biggest issue of 3D analysis is that whenever a 2D mesh is projected along the third direction, the total number of nodes grows dramatically. To understand this problem, the meshes used in the 2D problem can be analyzed. The mesh used for $Ra = 10^4$ was a 20×20 mesh. A $20 \times 20 \times 20$ mesh used in the 3D case would employ 8000 nodes, comparable to a $\approx 89 \times 89$ 2D mesh. In the case of $Ra = 10^6$, a $60 \times 60 \times 60$ would have the same number of nodes of a $\approx 465 \times 465$ 2D mesh. Such meshes, coupled with the CFL conditions for the time step (eq. 4.47), would require a large amount of time to compute the solution. It is then necessary to change the mesh structure to reduce the number of nodes per direction.

The criterion used to choose the mesh density in the 2D DHC was based on the fact that the mesh needed to be fine enough to predict the properties distribution in the diffusive layer at the walls. That zone, in fact, is characterized by elevated gradients, causing a brusque change of the properties along the normal direction: for this reason, the assumption of FVM that the thermophysical properties are constant within the control volume can only be valid if the mesh is fine enough. If the mesh is too coarse, moreover, the interpolation of the fluxes at the faces can result rather imprecise. The resolution of the 2D problem, however, demonstrated that the zone far from the wall is characterized by relatively high stability and limited gradients of temperature and velocity.

For this reason, a hyperbolic mesh is designed. The mesh is built so that the nodes density is higher close to the walls, and coarser in the center of the cavity. Grid spacing is performed with the help of a hyperbolic-tangent function. The x-axis west faces definition is shown below:

$$x_w[i] = \frac{D}{2} \left\{ 1 + \frac{\tanh \left[\gamma \left(2 \, \frac{i-1}{N} - 1 \right) \right]}{\tanh \gamma} \right\} \tag{4.48}$$

The node density at the walls rises with the **concentration factor** γ, whereas at the center of the cavity it decreases. i and N represent respectively the i-th node and the total number of nodes along the x-direction.

The number of nodes and the concentration factor are selected so that the diffusive layer is adequately resolved. In particular, there are two diffusive layers: a thermal boundary layer, characterized by conductive heat transfer, and a viscous boundary layer, characterized by high velocity diffusion. By definition, given the reference properties T_∞ and w_∞, the thermal and viscous boundary layers are – respectively – the regions close to the walls in which $T \leq 0.99\, T_\infty$ and $|w| \leq 0.99\, |w_\infty|$ [73].[13] T_∞ and w_∞ are defined as the temperature and velocity where the influence of the boundaries is null. The two

---

[13] In this case, however, the velocity decreases after a maximum, so the definition cannot be used. The viscous boundary layer is the region that starts on the wall and ends at the the first point after $x_{w_{max}}$ such that $\frac{w_{max}-w}{w_{max}-w_\infty} = 0.99$.

boundary layers can be seen, for example, in fig. C.12(d). The temperature distribution in the thermal boundary layer is monotonic, while the velocity in the viscous boundary layer reaches a maximum and then decreases: in this case $w_\infty = 0$ and $T_\infty = T_0$. In the meshes used in the 2D problem, the viscous layer portion before the maximum was well-resolved with at least four grid points. In the 3D problem resolution the selection of the concentration parameter and the number of nodes will guarantee that the maximum vertical velocity is located at least at the fourth node from the wall (giving at least seven/eight nodes within the boundary layers).

Results

The results of the 2D and 3D non-Boussinesq fluid problems are compared in tab. 4.8. The mesh is $20 \times 20 \times 20$ up to $Ra = 10^5$, and $30 \times 30 \times 30$ for $Ra = 10^6$. $\gamma_1, \gamma_2, \gamma_3$ are all equal and have values of $0, 0.5, 1.5, 1.2$ for $Ra = 10^3$, $Ra = 10^4$, $Ra = 10^5$, $Ra = 10^6$.

Table 4.8: Variable thermophysical properties – comparison between 3D DHC and 2D DHC results.

	2D analysis Ra				3D analysis Ra			
	10^3	10^4	10^5	10^6	10^3	10^4	10^5	10^6
u_{max}	3.664	16.099	34.885	65.686	3.527	16.564	38.087	76.958
y	—	—	—	—	0.525	0.527	0.697	0.757
z	0.825	0.813	0.858	0.842	0.825	0.840	0.873	0.863
v_{max}	—	—	—	—	0.174	2.146	9.535	23.950
w_{max}	3.720	19.532	68	219.19	3.522	18.813	68.564	234.99
x	0.175	0.113	0.058	0.042	0.175	0.112	0.086	0.039
y	—	—	—	—	0.525	0.739	0.873	0.918
$\overline{Nu}$	1.124	2.259	4.564	9.095	1.076	2.098	4.363	8.799
$Nu_{1/2}$	1.123	2.259	4.564	9.095	1.075	2.098	4.363	8.798
Nu_0	1.160	2.266	4.566	9.094	1.080	2.099	4.363	8.800
Nu_{max}	1.651	3.594	7.953	19.438	1.780	3.773	8.131	19.088
y	—	—	—	—	0.025	0.473	0.622	0.796
z	0.025	0.138	0.075	0.025	0.025	0.112	0.0862	0.0394
Nu_{min}	0.707	0.589	0.726	0.955	0.720	0.542	0.647	0.797
y	—	—	—	—	0.525	0.160	0.946	0.0070
z	0.975	0.988	0.992	0.992	0.975	0.978	0.991	0.993

Comparing the results, it is possible to see that u_{max} becomes a little higher, especially for $Ra = 10^5, 10^6$. This difference is due to a different behavior of the fluid when the third direction is included: the maximum horizontal velocity does not occur at the mid y-normal plane, but between that plane and the lateral walls. The maximum velocity component v_{max}, introduced in the 3D analysis, demonstrates to be rather lower compared to u_{max} and w_{max}.[14] The location of u_{max} in the z-coordinate direction is close to the one obtained in the previous analysis. The observations made for u_{max} are also valid for w_{max}; in this case, though, the shift along the y-coordinate starts at $Ra = 10^4$. $\overline{Nu}$, $Nu_{1/2}$, Nu_0 and Nu_{min} become a little lower, while Nu_{max} increases (except for the highest Rayleigh).

---

[14] It is important to remember that u_{max} and w_{max} are the maximums of the mid x-normal and z-normal planes, whereas v_{max} is the global maximum of the cavity. The u and w global maximums occur at shifted position, and they are higher: $u_M = 121.977$ and $w_M = 235.71$ for $Ra = 10^6$.

The higher value of the maximums of the velocity components can be explained by the fact that, at the edges, the conductive layer expands more, as shown in fig. 4.7. The fluid located next to the edges is influenced by both the walls of the edge, so its velocity is raised. For low Rayleigh number, this effect is partially balanced by the fact that all the walls are relatively close and lower the fluid velocity.

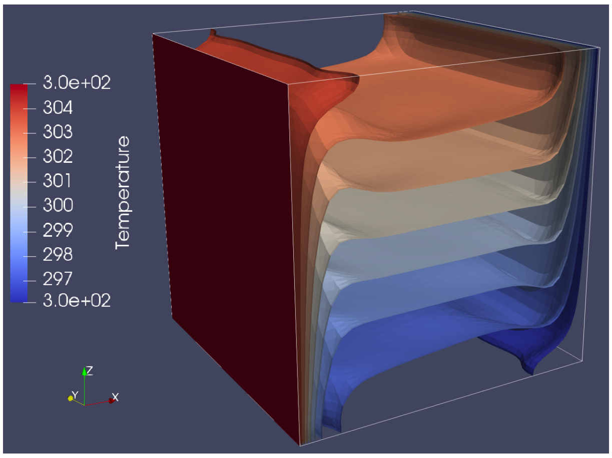

Figure 4.7: 3D DHC temperature map (variable thermophysical properties), isothermal surfaces for $Ra = 10^6$.

Fig. C.13 shows that the y-normal mid planes of the cavity are almost equal to the solution of the 2D cavity for $Ra = 10^3$, 10^6.

The Nusselt values at the hot wall and the mid vertical maps for the four configurations are consistent with the 3D study of Wang, Zhang & Guo (2017) [74], as shown in tab. 4.9 and fig. C.14.

Table 4.9: Comparison of the Nusselt number at the hot plate with the solution given by Wang et al.

		Ra			
		10^3	10^3	10^3	10^6
Nu_0	Whang et al.	1.070	2.054	4.325	8.543
	Developed code	1.080	2.099	4.363	8.800

4.3 Turbulent Flow

The flow of a fluid is called turbulent when it is characterized by sudden and chaotic changes in the velocity and pressure fields. The random movement of its particles has an influence on the heat transfer process, since parts of the fluid at different temperatures are continuously mixed. Turbulence arises when the kinetic energy of the fluid is so high that it cannot be damped by its viscosity. The instability of the fluid flow is a consequence of the nonlinear term of the momentum equation. Turbulence is strictly related with boundary conditions, since they influence locally the pressure and velocity field.

Turbulence will be analyzed as applied to the previous problems: the driven cavity and the differentially heated cavity. However, it is firstly introduced with an illustrative problem that is useful to show its main characteristics: the Burgers' equation.

4.3.1 Burgers' equation

The 1D Burgers' equation can be viewed as a simplified model of the Navier-Stokes equation:

$$\frac{\partial u}{\partial t} + u\,\frac{\partial u}{\partial x} = \frac{1}{Re}\,\frac{\partial^2 u}{\partial x^2} + f \qquad \longrightarrow \qquad \partial_t u + u\,\partial_x u = \frac{1}{Re}\,\partial_{xx} u + f \tag{4.49}$$

f is the **forcing term** of the equation. The equation is projected in the discrete Fourier space, defining $u\,(x,\,t) = \sum_{K=-N}^{N} \hat{u}_k\,(k,\,t)\;e^{ikx}$ (where N is the cut-off frequency):

$$\partial_t \hat{u}_k + \sum_{k=p+q} \hat{u}_P\,i\,q\,\hat{u}_q = -\frac{k^2}{Re}\,\hat{u}_k + F_k, \qquad k = -N, \ldots, N \tag{4.50}$$

where $F_k = 0$ for $k > 1$ and F_1 such that $\partial_t \hat{u}_1 = 0$ for $t > 0$. The kinetic energy equation for the k-th Fourier mode is obtained multiplying eq. 4.50 by $\overline{\hat{u}_k}$ and adding its complex conjugate.[15]

$$\partial_t E_k = \underbrace{-\frac{2\,k^2}{Re}\,E_k}_{diff.} \underbrace{-\left[\overline{\hat{u}_k}\,C_k\,(\hat{u}_p,\,\hat{u}_q) + \hat{u}_k\,\overline{C_k\,(\hat{u}_p,\,\hat{u}_q)}\right]}_{conv.} + \overline{\hat{u}_k}\,F_k + \hat{u}_k\,\overline{F_k} \tag{4.51}$$

where $C_k\,(\hat{u}_p,\,\hat{u}_q) \in \mathbb{C}$ is the convective contribution $C_k\,(\hat{u}_p,\,\hat{u}_q) = \sum_{k=p+q} \hat{u}_p\,i\,q\,\hat{u}_q$. Eq. 4.51 illustrates how energy transfers from large scales of motion to small scales. The diffusive term is responsible for kinetic energy dissipation: it grows with the square of the number of the mode k, so it is higher for higher frequencies (associated to smaller scales of motion). The higher the Reynolds, the lower the damping effect. The convective term, instead, is responsible for transporting energy from larger to smaller scales and vice versa; this process is known as **energy cascade**. The diffusive and convective terms in the Navier-Stokes equation have the same role: the diffusive term operates at the smaller scales (i.e. at smaller eddies, in case of turbulence), where the Laplacian of the velocity is greater, and damps the energy, while the non-linear convective term transports kinetic energy between scales of different size.

Problem definition

The goal is to solve the Burgers' equation for $Re = 40$. No mean flow is assumed ($\hat{u}_0 = 0$). The initial condition is $\hat{u}_k = k^{-1}$.

---

[15] The kinetic energy is defined as $E_k = \hat{u}_k\,\overline{\hat{u}_k}$, so $\partial_t E_k = \partial_t\left(\hat{u}_k\,\overline{\hat{u}_k}\right) = \hat{u}_k\,\partial_t\overline{\hat{u}_k} + \overline{\hat{u}_k}\,\partial_t\hat{u}_k$

Resolution

The mode $k = 0$ is not resolved, since $\hat{u}_0 = 0$. The negative modes are obtained directly from the positive, since $\hat{u}_k = \overline{\hat{u}_{-k}}$: this condition must be fulfilled to have $u(x,\, t) \in \mathbb{R}$. The forcing term makes that $\hat{u}_1 = k^{-1} \forall t$. Eq. 4.50 is discretized with a second-order explicit Adams-Bashforth method.

$$\frac{u_k^{n+1} - u_k^n}{\Delta t} = R\left(k^{n+1/2}\right) = \frac{3}{2}\, R\left(k^n\right) - \frac{1}{2}\, R\left(k^{n-1}\right), \qquad k > 1 \tag{4.52}$$

where $R\left(k\right) = -\frac{k^2}{Re}\, \hat{u}_k - C_k\left(\hat{u}_p,\, \hat{u}_q\right)$. A CFL-like condition must be set: $\Delta t < 0.08\, \frac{Re}{N^2}$.

The results of the problem are shown in fig. 4.8.

One step further: the Large Eddy Simulation model

The Large Eddy Simulation (LES) model is a mathematical model used to describe turbulence. The difference with a DNS approach is that LES does not solve all the scales of motion: the large scales are solved, while the small scales are modeled. The advantage of LES models is that they can reduce significantly the number of nodes of the mesh, and consequently the computational time required (especially in explicit methods, where a coarser mesh also involves a higher time step).

A spectral eddy-viscosity model developed by Métais & Lesieur (1992) [75] is shown below: the velocity in eq. 4.49 is filtered as

$$\partial_t \overline{u} + \overline{u}\, \partial_x \overline{u} = \nu\, \partial_{xx} \overline{u} + f - \partial_x \boldsymbol{\tau}\left(u\right) \tag{4.53}$$

$\boldsymbol{\tau}\left(u\right)$ is called **subfilter tensor**. $\boldsymbol{\tau}\left(u\right)$ can be obtained by the following formulas:

$$\boldsymbol{\tau}\left(u\right) = \nu_t\, \partial_x \overline{u} \tag{4.54a}$$

$$\nu_t\left(\frac{k}{N}\right) = \nu_t^{+\infty}\left(\frac{E_N}{N}\right)^{1/2} \nu_t^*\, \frac{k}{N} \tag{4.54b}$$

$$\nu_t^{+\infty} = 0.31\, \frac{5-m}{m+1}\, \sqrt{3-m}\, C_K^{-3/2} \tag{4.54c}$$

$$\nu_t^*\left(\frac{k}{N}\right) = 1 + 34.5\, e^{-3.03\,(N/k)} \tag{4.54d}$$

where ν_t is the **eddy viscosity**, E_N is the energy associated to the N-th mode, m is the opposite of the slope of the energy spectrum and C_K is the Kolmogorov constant. For the Burgers' equation, $m \approx 2$ and $C_K \approx 0.4523$. The subfilter tensor can be merged with the viscosity ν of eq 4.53 as $\nu_{eff}\left(k\right) = \nu + \nu_t\left(k\right)$.

Results

The results obtained at the steady state are presented in fig. 4.8. $N = 100$ solves the equation with

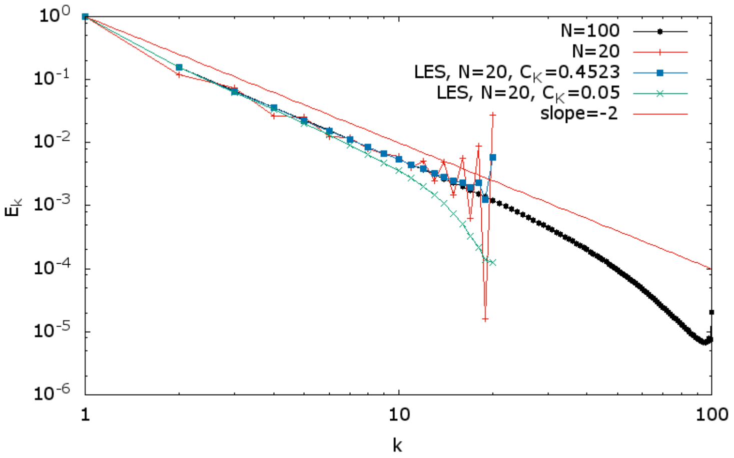

Figure 4.8: Kinetic energy over Fourier mode – solution of the 1D Burgers' equation.

enough modes to provide a precise result. The standard solution for $N = 20$ starts oscillating at its highest frequencies. The model demonstrates that there is a surplus of energy that accumulates on these frequencies and cannot be passed to higher ones to be damped by the viscosity. The LES case, instead, provides an almost realistic result also for $N = 20$: although energy cannot be dissipated in the small scales, it is artificially dispersed by the effective viscosity ν_{eff} of the spectral model. The figure also shows how the impact of the eddy viscosity is enhanced by a lower Kolmogorov constant.

4.3.2 Near-wall mesh definition in turbulent flows

The near-wall region in turbulent flow has a rather different nature respect to the rest of the domain. Turbulence is characterized by chaotic flow and isotropic energy transport through convection. The wall boundary layer is characterized by geometry dependence, anisotropic eddy propagation and high diffusion. The near-wall region has to be well-designed, since it is the zone where the largest amount of energy is dissipated. The near-wall region can be described using non-dimensional wall coordinates. Two quantities can be defined: the **non-dimensional average velocity** u^+ flowing parallel to the surface and the **non-dimensional wall coordinate** y^+ perpendicular to the wall [76].[16]

$$y^+ = \frac{y\, u_\tau}{\mu/\rho}, \qquad u^+ = \frac{u}{u_\tau}, \qquad \text{where} \quad u_\tau = \sqrt{\frac{\tau_w}{\rho}}, \qquad \tau_w = \mu \left.\frac{\partial u}{\partial y}\right|_{y=0}$$

u_τ is the **shear velocity**, and τ_w is the wall shear stress. The near-wall region dependence between u^+ and y^+ is shown in fig. 4.9. Three zones can be distinguished:

viscous sublayer region characterized by linear growth of the velocity, due to high viscosity ($y^+ < 5$)

buffer layer transition region between viscous and log-law region ($5 < y^+ < 30$)

---

[16] u^+ is averaged in time since in a turbulent flow the velocity is not constant. However, especially in the part of the region closest to the wall, the flow is laminar due to the high viscous forces, and u^+ coincides with the instant velocity.

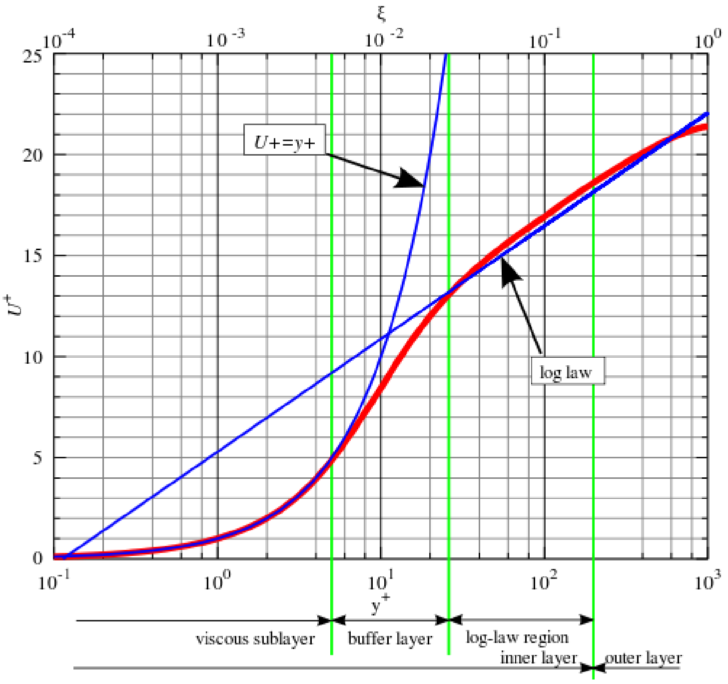

Figure 4.9: Velocity profiles in the inner layer expressed in wall-coordinates. Figure retrieved from Wikipedia [76].

log-law region zone characterized by a logarithmic growth of the velocity ($y^+ > 30$)

In order to predict the distribution of the quantities of interest in the near-wall region, all the zones are computed with a sufficient number of nodes. The most critical zone is the first, since it is the thinnest. The approach used in this work has been described by Zhang et al. (2015) [77]: in order to perform a consistent wall analysis, the first node must occur at a distance $y^+ <= 1$. This method will be used in the analysis of the DHC problem.

4.3.3 Driven Cavity – Turbulent Flow

Although the driven cavity problem has been studied by many authors, there is still uncertainty in the identification of the Re at which transition to instability can be observed. In the reference paper analyzed in sec. 4.2.1 the authors were able to obtain steady state results up to $Re = 10000$. Peng, Shiau & Hwang (2003) [78] obtained the first Hopf bifurcation leading to a periodic state at $Re \approx 7500$. Erturk, Corke & Gökçöl (2005) [79] were able to solve the steady state equation up to $Re = 21000$. Bruneau & Saad (2006) [80] evaluated the first Hopf bifurcation at $Re \approx 8000$, looking if a small perturbation added to the steady state eventually dissolves. In this study, turbulence appears between $Re = 7500$ and $Re = 10000$.

Six Reynolds values are investigated: $Re = 10000,\ 12500,\ 15000,\ 17500,\ 20000,\ 21000$. It is not possible to use the approach shown in sec. 4.3.2 to the driven cavity problem: a hyperbolic mesh of 256×256

nodes with $\gamma = 2.5$ still cannot keep the location of the first node below $y^+ = 1$. This is due to the fact that the wall shear stress at the top-right corner goes to infinite when the mesh is finer.[17] Therefore, the mesh suitability is verified comparing the results from an external reference. $Re = 10000$ is solved with a 128×128 constant mesh, while the other cases are solved with a 256×256 constant mesh.

The turbulent driven cavity is characterized by a periodical oscillation of the velocity and pressure fields that varies with the Reynolds number. After an initial chaotic transient, the flow reaches a statistical steady state, as shown in fig. 4.10(a) by the plot of the horizontal velocity in correspondence of five fictitious probes at different locations for the case $Re = 10000$. It is possible to see that the oscillation becomes stable at $t \approx 1000$ s. Fig. 4.10(a), however, only shows points at a distance of 40 seconds; a magnification of the region between $t = 2100$ s and $t = 2130$ s is shown in fig. 4.10(b). The oscillations shown in the right figure have a frequency of 0.58 Hz, which is close to the value of 0.61 Hz identified by Bruneau & Saad. The effect of these oscillations on the flow can be visualized by the stream function map of the cavity: some significant captures are shown in fig. C.15. The frames at $t = 401$ s and $t = 407$ s are almost equal, showing that the periodicity is equal throughout the whole cavity. The instant frames are also useful to understand the nature of the eddies: comparing the frames at $t = 401$ s and $t = 406$ s, it is possible to see that the two eddies located at the left corners periodically splits and then reunite again. Average solutions of the stream function and the velocities along the mid vertical and horizontal axes are computed, evaluating a sufficient period that permits to neutralize the oscillations. For the case $Re = 10000$, the averaging has been performed between $t = 1440$ s and $t = 2160$ s (the region delimited

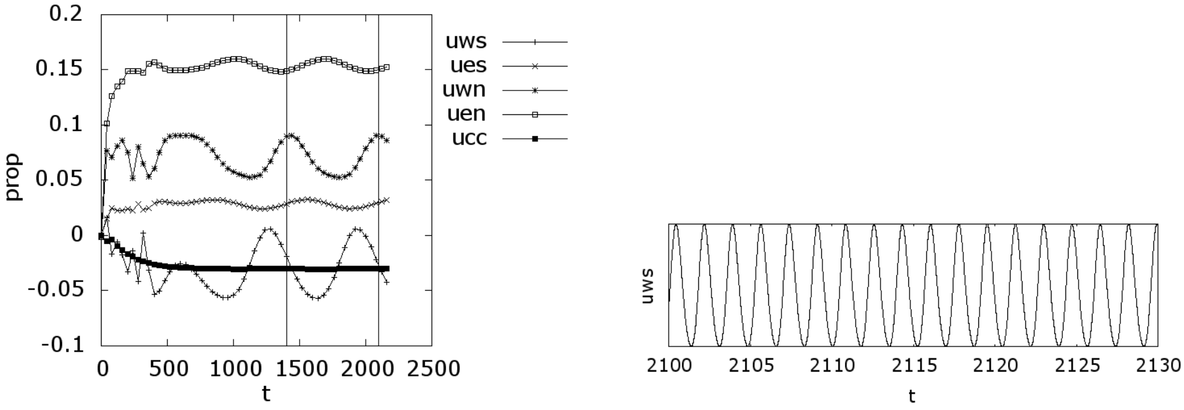

(a) Whole time domain considered

(b) Magnification for $t \in (2100, 2130\,s)$, south-west probe

Figure 4.10: Local oscillation of the horizontal component of the velocity at different locations.

---

[17] To understand this issue, it is possible to focus on the north-east control volume: the mass flow u_w entering its west face must be equal to the one leaving from the south face v_s (since the mass flow onto two other faces is null due to presence of the physical walls). The two shear stresses at the north and east faces are $\tau_{w_N} = \mu \left| \frac{u_N - u_w}{dy} \right|$ and $\tau_{w_E} = \mu \left| \frac{v_E - v_s}{dx} \right|$ where u_N is the north wall velocity, while v_E is the east wall velocity. Since $u_N \neq v_E$, the two numerators cannot be equal to zero simultaneously. If dx and dy go to zero, one of the two fractions diverges.

by the vertical line in fig. 4.10(a)). The results are shown in fig. C.17. From fig. C.17(a) it is possible to identify the three secondary eddies that arise for $Re = 10000$ in both corners of the south wall, in accordance with the steady-state solution of Erturk et al.

The periodicity of the flow repeats for the other Reynolds cases. The frequencies of the smallest oscillation are $f = 0.58,\, 0.68,\, 0.65,\, 0.61$ Hz, for $Re = 10000,\, 12500,\, 15000,\, 17500$ respectively; from $Re = 20000$ onwards the oscillations become more unstable, and it is no longer possible to detect a single frequency. For $Re = 15000$, the two inner secondary eddies located in the south-east corner start periodically splitting as well.

The results of the average horizontal velocity along the mid vertical axis are presented in fig. C.16, compared with the steady state solution of Erturk et al. The results appear quite similar to the reference case, although some differences can be found in the region near the north and south walls: these differences are somehow expected since the turbulent nature of the fluid has a large impact on the outer part of the largest eddy, that coincides with the boundary layer region next to the center of every wall.

Although the results seem to provide a realistic solution, a computation with a finer mesh is not carried out since the computational cost is too high. The reference papers used finer meshes up to 1024×1024 nodes and high-order schemes to validate their results. Therefore, the results obtained are likely to be quite less accurate respect to the references. Mesh refinement is still needed in order to confirm the suitability of the meshes for the study of turbulence in the driven cavity problem. On the other hand, the results obtained are similar to the reference solutions enough to affirm that the code developed provides a correct computational framework for the resolution of the problem.

4.3.4 Differentially Heated Cavity – Turbulent Flow

Although the third dimension should be always considered in fluid dynamics (since the motion of a fluid can be described in 2D only under some approximations), the most relevant differences between 2D and 3D motion arise when turbulence is involved. Turbulence, in fact, is isotropic, and always develops in the three directions regardless of the boundary conditions. However, as explained in sec. 4.2.2.C, the computational cost grows dramatically with 3D analysis, especially with turbulent flows, that request a higher number of increasingly small control volumes and, as a consequence of the CFL conditions, a lower time step. Given the high CPU cost of 3D, a first 2D approach is presented: the lower time of computation, in fact, makes it possible to analyze two cases: $Ra = 6.4 \cdot 10^8$ and $Ra = 2 \cdot 10^9$. The 3D analysis, instead, is restricted to $Ra = 6.4 \cdot 10^8$, since the elevated computational time does not permit to carry out simulations at $Ra = 2 \cdot 10^9$.

The results obtained are compared with the reference work of Trias, Gorobets, Soria & Oliva (2010) [81,82]. Trias et al. analyzed a vertical DHC of aspect ratio $A_z = 4$ for cases ranging from $Ra = 6.4 \cdot 10^8$

to $Ra = 10^{11}$.[18] The authors performed a 3D simulation. Differently from this thesis, they assumed a Boussinesq fluid. In the present work, instead, the *variable termophysical properties* approach is used, according to what presented in the laminar flow. Trias et al. considered Periodic Boundary Conditions (PBC) at the secondary vertical walls: the flow is extended indefinitely along the y direction being mirrored from one wall to the other. In the present work, instead, the additional walls are considered physically present and adiabatic, according to the approach used in the laminar flow.

Results

Eight time-averaged parameters are compared: the Nusselt number at the hot wall $\overline{Nu}_0$, the maximum and minimum Nusselt numbers at the hot wall $\overline{Nu}_{max}$ and its z location, the maximum velocities at the mid horizontal plane $\overline{u}_{max_{xy}}$ and $\overline{w}_{max_{xy}}$ and their x location, the maximum velocities and the temperature at the mid x-perpendicular vertical plane $\overline{u}_{max_{yz}}$, $\overline{w}_{max_{yz}}$ and $\overline{T}_{max_{yz}}$ and their z location. The average Nusselt of the whole cavity is not considered, since it is assumed to be equal to the Nusselt at the hot wall (as demonstrated by the previous analyses). Moreover, the maximum first node location in wall non-dimensional coordinates Δy^+_{max} is reported. The computation of average values, as in the driven cavity problem, is performed as soon as the system reaches a statistical steady state. The comparison between the reference case and the results computed are shown in tab. 4.10. In the 2D case, properties are considered constant along the third direction (i.e. $\overline{u}_{max_{xy}} \equiv \overline{u}_{max_x}$ etc.). In the 3D case, a horizontal aspect ratio $A_y = 2$ (the ratio of the depth to the length) is assumed, as in the reference study.

Table 4.10: Turbulent DHC – comparison between reference and the variable thermophysical properties models developed.

	3D Reference Ra		2D results Ra		3D results Ra
	$6.4 \cdot 10^8$	$2 \cdot 10^9$	$6.4 \cdot 10^8$	$2 \cdot 10^9$	$6.4 \cdot 10^8$
$\overline{Nu}_0$	49.24	66.63	49.24	65.92	48.19
$\overline{Nu}_{max}$	171.89	260.49	174.03	252.38	197.32
z	$3.63 \cdot 10^{-3}$	0	$3.66 \cdot 10^{-3}$	$2.37 \cdot 10^{-3}$	$4.48 \cdot 10^{-4}$
$\overline{u}_{max_{xy}}$	$9.02 \cdot 10^{-4}$	$6.36 \cdot 10^{-4}$	–	–	$3.71 \cdot 10^{-3}$
x	$2.22 \cdot 10^{-1}$	$2.29 \cdot 10^{-1}$	–	–	$1.75 \cdot 10^{-2}$
$\overline{w}_{max_{xy}}$	$2.22 \cdot 10^{-1}$	$2.22 \cdot 10^{-1}$	$2.23 \cdot 10^{-1}$	$2.23 \cdot 10^{-1}$	$2.74 \cdot 10^{-1}$
x	$7.26 \cdot 10^{-3}$	$5.76 \cdot 10^{-3}$	$8.03 \cdot 10^{-3}$	$5.60 \cdot 10^{-3}$	$8.03 \cdot 10^{-3}$
$\overline{u}_{max_{yz}}$	$2.72 \cdot 10^{-2}$	$1.76 \cdot 10^{-2}$	$1.89 \cdot 10^{-2}$	$1.92 \cdot 10^{-2}$	$7.62 \cdot 10^{-2}$
z	$9.52 \cdot 10^{-1}$	$9.57 \cdot 10^{-1}$	$9.51 \cdot 10^{-1}$	$9.51 \cdot 10^{-1}$	$9.75 \cdot 10^{-1}$
$\overline{w}_{max_{yz}}$	$4.47 \cdot 10^{-2}$	$1.67 \cdot 10^{-2}$	–	–	$2.76 \cdot 10^{-2}$
z	$6.91 \cdot 10^{-2}$	$6.01 \cdot 10^{-2}$	–	–	$4.13 \cdot 10^{-2}$
$\overline{T}_{max_{yz}}$	$8.91 \cdot 10^{-1}$	$8.93 \cdot 10^{-1}$	$8.92 \cdot 10^{-1}$	$8.84 \cdot 10^{-1}$	$9.07 \cdot 10^{-1}$
z	$9.85 \cdot 10^{-1}$	1	1	1	$8.79 \cdot 10^{-1}$
Δy^+_{max}	–	–	$9.85 \cdot 10^{-1}$	$8.83 \cdot 10^{-1}$	$9.28 \cdot 10^{-1}$

All the results seem to be rather concordant with the benchmark solution, despite the differences in

---

[18] The aspect ratio, in this case, is the ratio of the height to the length – respectively z to x coordinate.

boundary conditions and fluid model. The 2D case, in particular, shows to be suitable to the resolution of the DHC up to $Ra = 2 \cdot 10^9$: the differences with the 3D reference case are minimum. The 3D computation, instead, is characterized by some dissimilarities, especially regarding maximum and minimum values. This behavior could be a consequence of the presence of adiabatic vertical walls, that still play a crucial role for a Rayleigh close to the critical one determining transition between laminar and turbulent flow. In fact, the proximity of these secondary walls could prevent the turbulent eddies from expanding isotropically: for such a Rayleigh, the vortex magnitude is still elevated. If this supposition is correct, the influence of the secondary vertical walls is expected to diminish as Ra increases.

Fig. 4.11 shows the average temperature field for the 2D and 3D resolution of the DHC. The mid y-normal plane of the 3D cavity is rather different from the 2D temperature map. This difference is due to the fact that the eddy formation in the 3D case is not completely chaotic: periodically, three main vortexes keeps on forming in three approximately fixed locations. The three vortexes can be pointed out in the second hottest isotemperature surface of fig. 4.11(d). This nature cannot obviously predicted by the 2D computation, so the maps shown in fig. 4.11(a) and fig. 4.11(c) are different. The fluid is fully stratified outside the boundary layer and the eddy formation zone. The thermal boundary layer shrinks as the Rayleigh increases, confirming the trend started with the laminar flow; fig. C.18 shows the mid z

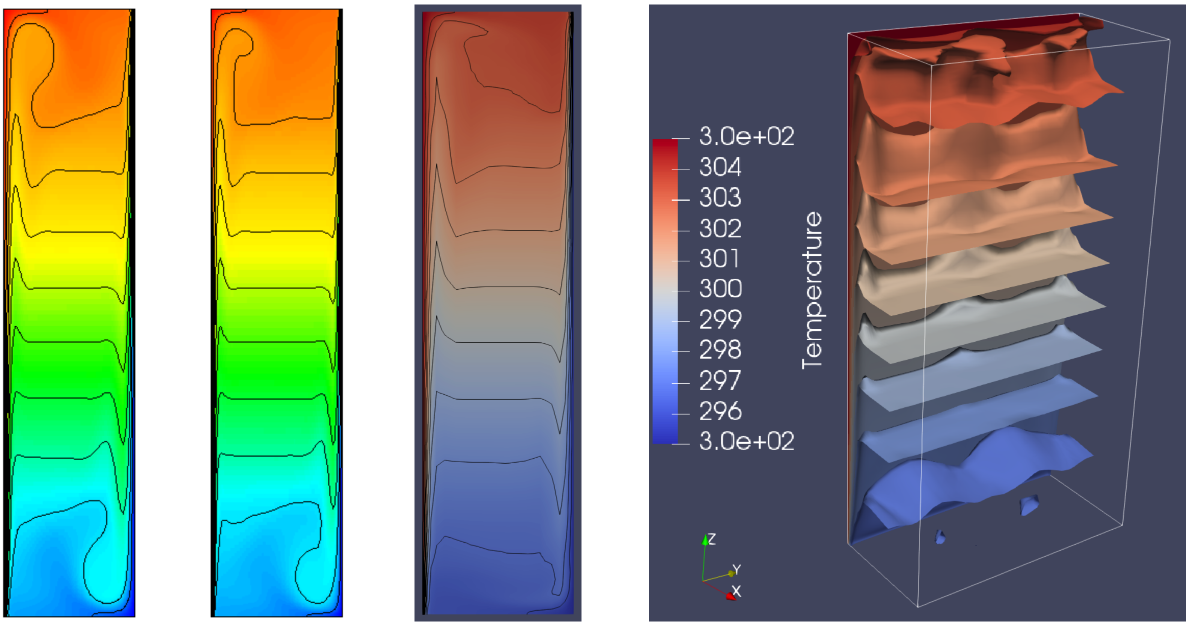

(a) $Ra = 6.4 \cdot 10^8$, 2D

(b) $Ra = 2 \cdot 10^9$, 2D

(c) $Ra = 6.4 \cdot 10^8$, 3D mid plane

(d) $Ra = 6.4 \cdot 10^8$, 3D side view

Figure 4.11: Time-averaged temperature maps for the turbulent differentially heated cavity.

line for the 2D computation, showing that the phenomenon is valid also for the viscous boundary layer.

Towards a LES model for the Differentially Heated Cavity

LES has been already presented in sec. 4.3.1. The main advantage over a DNS is the modelization of the small-scale eddies, that permits to choose a much coarser mesh, and reduce dramatically the computational cost of the problem. When turbulence arises, DNS becomes prohibitive for most industrial simulation applications, since the computational time becomes too elevated. Therefore, LES is usually exploited to overcome this issue. In this section, the application of various LES models to the differentially heated cavity problem is presented. Since LESs work appropriately only if the three dimensions are considered, the model will be applied to the already-presented 3D DHC.

The main approach of LES, as already explained in sec. 4.3.1, consists in spacial filtering the Navier-Stokes equations. The subfilter tensor $\boldsymbol{\tau}\left(\overline{\mathbf{u}}\right)$ is introduced to act as a energy-dissipating factor at small scales. The most used closure model assumption is

$$\boldsymbol{\tau}\left(\overline{\mathbf{u}}\right) \approx -2\,\nu_e\,\mathbf{S}\left(\overline{\mathbf{u}}\right) \tag{4.55a}$$

$$\nu_e = \left(C_m\,\Delta\right)^2\,D_m\left(\overline{\mathbf{u}}\right) \tag{4.55b}$$

where $\mathbf{S}\left(\overline{\mathbf{u}}\right) = \frac{1}{2}\left(\nabla\overline{\mathbf{u}} + \nabla\overline{\mathbf{u}}^{\mathrm{T}}\right)$ is the rate-of-strain tensor, ν_e is the eddy viscosity, C_m is the model constant, Δ is the subgrid characteristic filtering length, and $D_m\left(\overline{\mathbf{u}}\right)$ is the differential operator associated to the model. In this work, the latter is defined for a family of eddy-viscosity models that depend on **five invariants**, according to Trias, Folch, Gorobets, & Oliva (2015) [83]: the Smagorinsky model (1963) [84], the Wall-Adapting Local Eddy (WALE) model (1999) [85], the Vreman's model (2004) [86] and the Verstappen's model (2011) [87]. The five invariants are tensors based on the 3D velocity field:

$$\left\{Q_G,\,R_G,\,Q_S,\,R_S,\,V^2\right\}$$

where $Q_A = \frac{1}{2}\left\{\mathrm{tr}^2\left(\mathbf{A}\right) - \mathrm{tr}\left(\mathbf{A}^2\right)\right\}$ and $R_A = \det\mathbf{A}$ denote the second and third invariant of the generic tensor $\mathbf{A}$. Q_G and R_G are referred to the tensor $\mathbf{G}\left(\overline{\mathbf{u}}\right) = \nabla\mathbf{u}$, while Q_S and R_S to $\mathbf{S}\left(\overline{\mathbf{u}}\right)$. The last invariant is defined as $V^2 = 4\left[\mathrm{tr}\left(\mathbf{S}^2\,\boldsymbol{\Omega}^2\right) - 2\,Q_S\,Q_\Omega\right]$ where $\boldsymbol{\Omega} = \mathbf{G} - \mathbf{S}$. The model parameters are shown in tab. 4.11. The subgrid length used is $\Delta = \sqrt[3]{V_P}$, being V_P the volume related to the node P.

Although the last three models are more suitable to solve problems highly dependent on boundary conditions, the C++ code developed does not to run for them (probably due to some mistake done in the writing process), and the lack of time available does not permit to point out the cause. The only working code is the one related to the Smagorinsky model. The great limitation of the Smagorinsky model is that the damping effect it involves does not vanish in the near-wall regions, where the flow is laminar: this causes an overdamping that provides an unrealistic computation result whenever physical boundary

Table 4.11: LES models parameters definition – differential operator and model constant.

Model	$D_m\left(\overline{\mathbf{u}}\right)$	C_m
Smagorinsky	$2\left(-Q_S\right)^{1/2}$	0.165
WALE	$\dfrac{\left(V^2/2+2\,Q_G^2/3\right)^{3/2}}{\left(-2\,Q_S\right)^{5/2}+\left(V^2/2+2\,Q_G^2/3\right)^{5/4}}$	0.596
Vreman's	$\left[\dfrac{V^2+Q_G^2}{2\left(Q_G-2\,Q_S\right)}\right]^{1/2}$	0.266
Verstappen's	$-\lvert R_S\rvert/Q_S$	0.527

conditions are present.

The computation run for the DHC confirms this effect: both in $Ra = 6.4 \cdot 10^8$ and $Ra = 2 \cdot 10^9$, the flow of the fluid stabilizes and reaches the steady-state. This is a physical nonsense, as DNSs demonstrated that the transition to turbulence occurs for $Ra \in \left(1 \div 5 \cdot 10^8\right)$. The steady-state solutions of the LES is shown in fig. 4.12 for illustrative purposes. The Nusselt numbers computed are totally unrealistic as well: the average Nusselt is $\overline{Nu}_0 = 126.818$ for $Ra = 6.4 \cdot 10^8$, while the DNS gave $\overline{Nu}_0 = 48.19$; the maximum Nusselt is $\overline{Nu}_{max} = 614.97$ for $Ra = 2 \cdot 10^9$, while the DNS gave $\overline{Nu}_{max} = 197.32$.

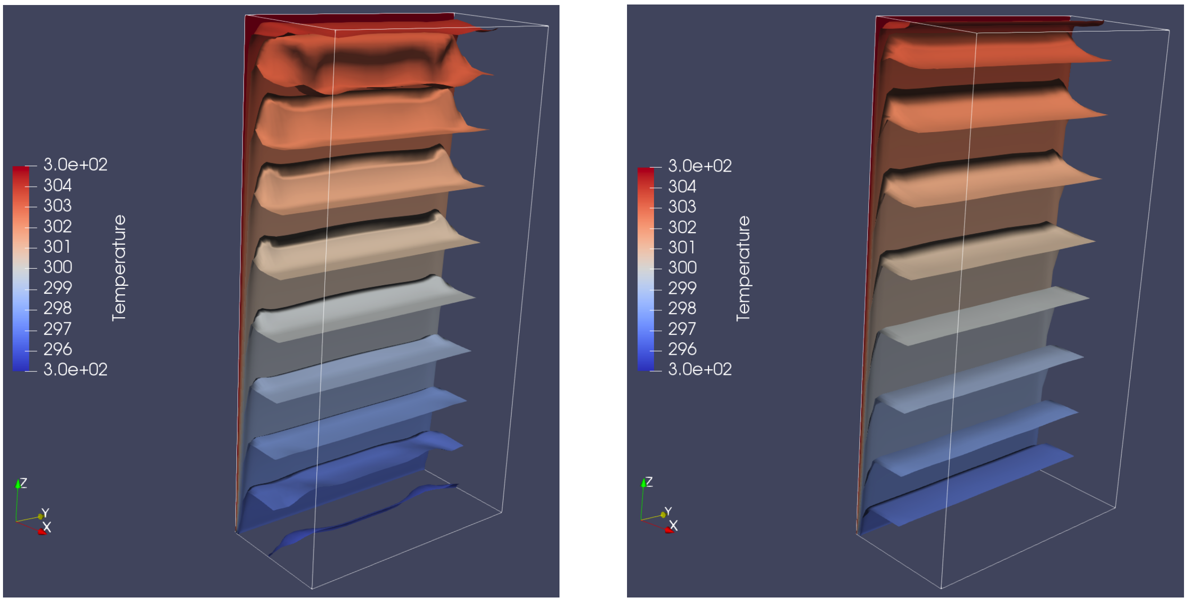

(a) $Ra = 6.4 \cdot 10^8$

(b) $Ra = 2 \cdot 10^9$

Figure 4.12: Steady-state temperature maps, Smagorinsky LES model of a differentially heated cavity.

Although LES can be an interesting tool to analyze highly-turbulent DNSs, corrections on the other three models presented must be adjusted to provide a consistent computation, since the Smagorinsky model has demonstrated to be unsuitable for this problem.

4.4 Final Considerations

Chapter 4 verified the codes developed both in laminar and in turbulent flows involving heat transfer processes. The codes were able to provide a full resolution of the mass, momentum and energy equations. The three unknown of the equations (pressure, velocity and temperature) can be computed not only at a particular instant of time, but also averaged for a preselected period of time.[19]

Both the 2D and 3D DNS codes are now able to be applied to the study of natural convection problems having different geometry, boundary conditions and initial conditions. In particular, they can be used to estimate the heat transfer processes involved in a receiver of a Central Receiver System. The LES code, instead, is still not ready to be used, although a deep inspection could make it possible to fix it giving the possibility to have another efficient tool for the study of natural convection processes.

Natural convection can also be coupled with the conduction occurring at the receiver with the design of a custom code that couples the conduction code validated in sec. 4.1.1 and the natural convection codes.

---

[19] Actually, in the continuity, Navier-Stokes and energy equation also other unknowns appear: the thermophysical properties ρ, μ, c_P, k. However, as assumed in the study, they can be assumed to be functions of the temperature.

5

Possible Application of the Codes to a Thermal Receiver and Final considerations

Contents

5.1 Setup for the Application of the Codes to a Thermal Receiver

As presented in sec. 2.2.3, solar tower receivers can be structured in many different ways. The codes developed in chapter 4 are able to solve with small modifications the natural convection occurring at a panel of an external tubular receiver (the panel of 70 tubes shown in fig. 2.3(a) is a good example). The receiver of *Solar Two* used in the performance analysis of sec. 2.4.3 is an example that can be studied with the developed codes, and the natural convection losses calculated in the performance analysis can be corrected to more realistic results. Following the study presented in sec. 2.4.3, the receiver height is $H = 6.2\,\mathrm{m}$. The average receiver temperature $\overline{T}_r = 774\,\mathrm{K}$ and the ambient temperature of $T_{amb} = 315.15\,\mathrm{K}$ ($42\,^\circ\mathrm{C}$) assumed in the analysis lead to a Rayleigh number for of $Ra \approx 7.7 \cdot 10^{11}$ (being the thermophysical properties calculated using the formulas given in sec. B.5). Such a number, given the limited CPU resources available for this study, makes the computational time needed too large: the study of the differentially driven cavity problem done by Trias et al., in comparison, gives only results up to a Rayleigh number of $Ra = 10^{11}$, despite the use of the MareNostrum supercomputer ($>$150000 CPUs) [81]. However, a possible modelization of the convection losses study solved with the 2D natural convection code developed is presented in fig. 5.1: following the setup that will be explained, a first CFD analysis on the receiver can be performed, in case sufficient computational resources are available. The codes developed so far worked with a rectangular cavity having the walls at different temperatures. In this model, the vertical west wall tries to recreate a flat panel of the tubular receiver.[1] The central section corresponds to the receiver itself, having the average temperature of $\overline{T}_r$; the upper and lower sections of the wall correspond to fictitious adiabatic walls. The three other walls represent three fictitious walls having a temperature equal to T_{amb}. The role of the fictitious walls is to recreate

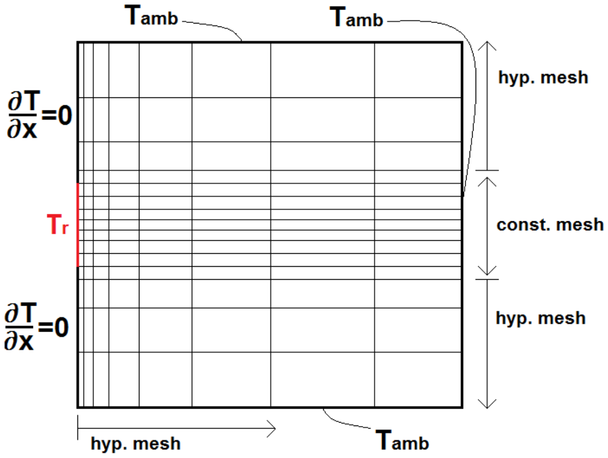

Figure 5.1: Mesh and boundary conditions definition for the computational study of natural convection in a cylindrical tubular receiver. The red line corresponds to a simplified panel of the receiver.

---

[1] The assumption of studying a flat panel as the receiver is the same made by Siebers & Krabaal: given the really thin boundary layer that forms, the cylindrical surface can be assumed as a vertical flat surface [52].

the phenomena occurring in the real convection at the receiver: the adiabatic walls drive the hot flux upwards, without introducing nor dissipating energy; the walls at ambient temperature "artificially damp" the energy absorbed by air, recreating the dispersion of the hot fluid in the ambient. It is crucial that the fictitious walls have no noticeable effect on the flow close to the receiver panel, where the Nusselt study is performed. For this reason, the energy-damping walls have to be put sufficiently distant from the receiver: their placement at a farther position should not change the convective losses at the receiver. The inner-layer at the hot panel must be well-resolved: the approach explained in sec. 4.3.2 can be applied, applying horizontally an adjusted version of the hyperbolic mesh described by eq. 4.48. The same mesh function can be used for spacing vertically the upper and lower west walls; vertical spacing at the receiver can be constant, according to fig. 5.1.

An interesting consequence of the resolution of the computational problem is the possibility to create a customized Nusselt correlation for the particular receiver analyzed, as a function of the Rayleigh number: the new correlation takes into account the effect of the variable thermophysical properties, that cannot be neglected for such high temperature gradients. The correlation obtained could be substituted in eq. 2.15 and used to calculate the overall convective losses. As an illustrative case, the study is performed on the 2D DHC of aspect ratio $A_r = 4$. Two cases of DHC are compared: the *benchmark* *case*, having the hot wall at $T_h = 305\,K$ and the cold wall at $T_c = 295$ K, and the *receiver case*, having the hot wall at $T_h = 774$ K and the cold wall at $T_c = 315$ K. The Nusselt result of the benchmark case is really close to the correlation computed by Trias et al, shown in fig. 5.2(a). Although the charts appear to be quite similar, it is important to state that the difference of the maximum Nusselt numbers obtained between the benchmark and the receiver case is rather high, especially for a high Rayleigh number. $Ra = 2 \cdot 10^9$, for example, involves that $\overline{Nu}_{max} \approx 252$ for the benchmark case, while $\overline{Nu}_{max} \approx 280$ for the receiver case. The same occurs with average Nusselt number, although the difference is less

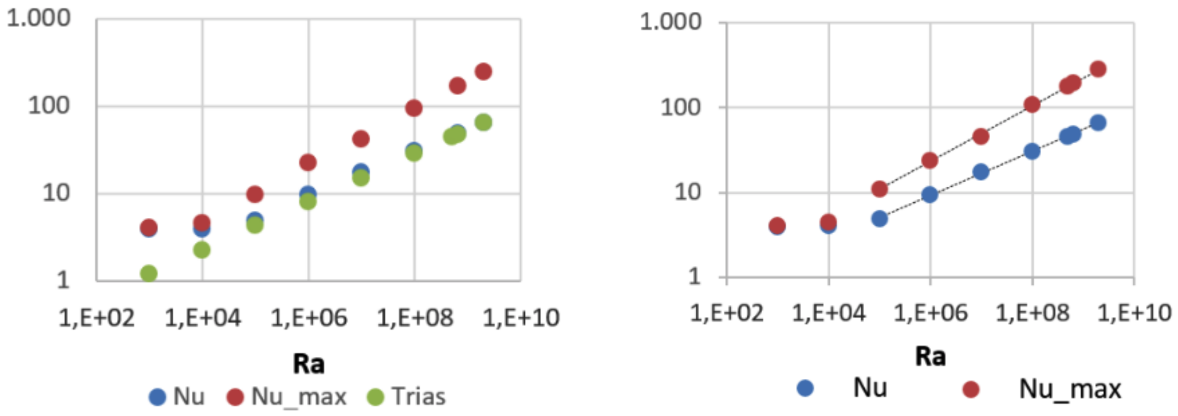

(a) Benchmark configuration

(b) Receiver configuration

Figure 5.2: $\overline{Nu}_0$ and $\overline{Nu}_{max}$ as a function of Ra, 2D DHC.

marked. The correlations for the Nusselt numbers in the receiver case is calculated. The first two Rayleigh numbers analyzed are not taken into account, since the flow behavior differs significantly as the viscous forces are still high: this can be seen in fig. 5.2(a), that shows that the average Nusselt computed differs from the correlation obtained by Trias et al. Therefore, only seven Rayleigh numbers have been analyzed, from $Ra = 10^5$ to $Ra = 2 \cdot 10^9$. The correlations obtained, whose trend lines are shown in fig. 5.2(b), are

$$\overline{Nu}_0 = 0.2565\, Ra^{0.259} \qquad \overline{Nu}_{max} = 0.2495\, Ra^{0.328}$$

Similar correlations (together with many others) could be obtained by solving a real case of natural convection at the receiver, by means of the setup shown previously with the mesh designed in fig. 5.1. The 2D setup can be easily extended to a third dimension (considering the depth of the panel), using the 3D code developed.

5.2 Conclusions

This thesis describes and verifies a new code for the computational study of the mass, momentum and energy transfer processes. The computational structure developed represents an efficient tool, tailored in order to be able to be applied to solve natural convection problems that arise in a thermal receiver of a CSP plant. The code gives a strong result, since it can provide the instant (or time-averaged) values of:

- the local and global values of the heat transfer (through the Nusselt number);
- the velocity, temperature and pressure field throughout the whole domain;
- the local viscosity, conductivity and density of the fluid;
- the shear stress at the walls τ_w.

Other physical quantities of the fluid (such as vorticity, stream function, enthalpy, ...) could be easily obtained whenever needed, applying small changes to the code. The computation of the fields is particularly precise, since it is carried out through a DNS, that fully solves the three equations. A possible application of the code has been presented in sec. 5.1: the computation of a Nusselt correlation specific to a receiver could be used in parallel to the correlation given by Siebers & Kraabel (eq. 2.14, 2.12, 2.11) in order to assess the convective losses.

The code developed still presents many limitations, that must be acknowledged for a future use. Its biggest limitation was the impossibility of testing it with a real case of convection: this operation is needed to confirm that the assumptions made are correct. A limitation included in the discussion of the setup for the application of the code to a panel of a cylindrical receiver (sec. 5.1) was the fact that the average temperature of the receiver $\overline{T}_r$ was extended to the whole panel; although it can be a first approximation useful to assess the global losses of the panel, in a real case the temperature varies significantly along the panel. Although a variable temperature at the west wall of fig. 5.1 can be easily implemented in the code, the difficult task is to hypothesize or compute the effective temperature distribution of the panel. The conduction within the panel could be easily implemented using the code developed in sec. 4.1.1; however, the forced conduction of the fluid flowing inside the tubes that compose the panel should be calculated. In addition, the thermal radiation of the panel should be considered. The final local balance for a node of the panel is shown in fig. 5.3. For the flow inside the tubes it is advisable to use a CFD code, to be able to solve it with precision; in theory, the codes presented could be modified to solve forced convection and applied to the inner fluid. Forced convection could be solved also for outer air, giving the possibility to analyze windy conditions. In that case, the whole convection process could be computed and the equations of Siebers & Kraabel would be completely substituted by a more realistic model.[2] In case of forced convection, a 3D simulation would become compulsory to simulate the flow around the whole cylindrical receiver: the setup explained in the previous section would no longer be valid, and an appropriate mesh should be developed to model the curved surface. The code could also be refined to solve different geometries (to be applied, for example, to a cavity receiver). The numerical approach could be modified in order to make the code more efficient: for example, with the use of a higher-order discretization, an adaptive time-step method, or an alternative implicit solver for the computation of pressure field. Moreover, parallelization of the code should be considered as a high-priority implementation, in order to dramatically reduce the computational time. Last but not least, the LES code could be corrected, giving the possibility to use it as an alternative to the DNS.

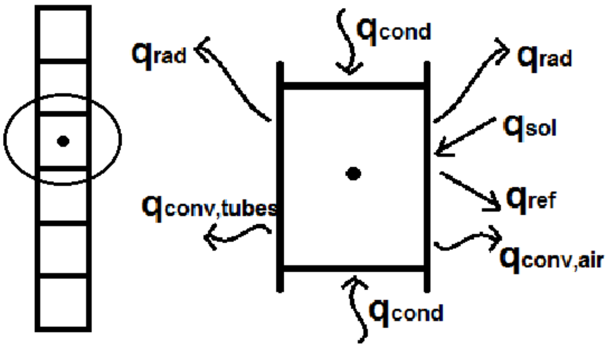

Figure 5.3: Panel modelization, with a magnification of the thermal balance at a particular node.

Although many ameliorations are still possible, a code able to provide a locally-detailed result of natural convection has been provided, and it is ready to be applied.

---

[2] In fact, the authors acknowledge the limits of their correlation regarding forced convection [52].

Bibliography

[1] OECD (2017), renewable energy (indicator). Accessed on 10 August 2017. [Online]. Available: https://data.oecd.org/energy/renewable-energy.htm

[2] P. Le Quéré, C. Weisman, H. Paillère, J. Vierendeels, E. Dick, R. Becker, M. Braack, and J. Locke, "Modelling of natural convection flows with large temperature differences: A benchmark problem for low mach number solvers. part 1. reference solutions," *ESAIM: Mathematical Modelling and Numerical Analysis*, vol. 39, no. 3, pp. 609–616, 2005, accessed on 27 October 2017.

[3] S. A. Kalogirou, "Solar thermal collectors and applications," *Progress in Energy and Combustion Science*, vol. 30, pp. 231–295, 2004, accessed on 12 August 2017.

[4] C.-J. Winter, R. L. Sizmann, and L. L. Vant-Hull, *Solar power plants*. Springer-Vlg, 1991, accessed on 25 October 2017.

[5] Energy.gov. (2013) Dish/engine system concentrating solar power basics. Accessed 24 October 2017. [Online]. Available: https://energy.gov/eere/energybasics/articles/dishengine-system-concentrating-solar-power-basics

[6] ——. (2013) Linear concentrator system basics for concentrating solar power. Accessed 24 October 2017. [Online]. Available: https://energy.gov/eere/energybasics/articles/linear-concentrator-system-basics-concentrating-solar-power

[7] ——. (2013) Power tower system concentrating solar power basics. Accessed 24 October 2017. [Online]. Available: https://energy.gov/eere/energybasics/articles/power-tower-system-concentrating-solar-power-basics

[8] H. L. Zhang, J. Baeyens, J. Degrève, and G. Cacères, "Concentrated solar power plants: Review and design methodology," *Renewable and Sustainable Energy Reviews*, vol. 22, pp. 466–481, accessed on 14 August 2017.

[9] X. Xu, K. Vignarooban, B. Xu, K. Hsu, and A. M. Kannan, “Prospects and problems of concentrating solar power technologies for power generation in the desert regions,” *Renewable and Sustainable Energy Reviews*, vol. 53, pp. 1106–1131, 2016, accessed on 15 August 2017.

[10] H. Müller-Steinhagen and F. Trieb, “Concentrating solar power,” *A review of the technology. Ingenia Inform QR Acad Eng*, vol. 18, pp. 43–50, 2004, accessed on 16 August 2017.

[11] M. Taylor, K. Daniel, A. Ilas, and E. Y. So, “Renewable power generation costs in 2014,” *International Renewable Energy Agency*, 2015, accessed on 27 October 2017.

[12] NREL, Ivanpah Solar Electric Generating System. Accessed on 18 August 2017. [Online]. Available: https://www.nrel.gov/csp/solarpaces/project_detail.cfm/projectID=62

[13] Y. Tian and C.-Y. Zhao, “A review of solar collectors and thermal energy storage in solar thermal applications,” *Applied energy*, vol. 104, pp. 538–553, 2013, accessed on 18 August 2017.

[14] A. Sayigh, *Renewable Energy: A Status Quo*, ser. River Publishers Series in Ren. River Publishers, 2016, accessed on 19 August 2017.

[15] F. Téllez, C. Vilasante, and M. Burisch, “State of the art in heliostats and definition of specifications,” 2014, accessed on 19 August 2017.

[16] H. Price, E. Lupfert, D. Kearney, E. Zarza, G. Cohen, R. Gee, and R. Mahoney, “Advances in parabolic trough solar power technology,” *Journal of solar energy engineering*, vol. 124, no. 2, pp. 109–125, 2002, accessed on 20 August 2017.

[17] Wikipedia, “Compact linear fresnel reflector — wikipedia, the free encyclopedia,” 2017, accessed on 27 October 2017. [Online]. Available: https://en.wikipedia.org/wiki/Compact_linear_Fresnel_reflector

[18] G. Zhu, T. Wendelin, M. J. Wagner, and C. Kutscher, “History, current state, and future of linear fresnel concentrating solar collectors,” *Solar Energy*, vol. 103, pp. 639–652, 2014, accessed on 27 October 2017.

[19] Center for Study of Science, Technology and Policy (CSTEP). (2014) Global Review of Solar Tower Technology. Accessed on 15 August 2017. [Online]. Available: http://www.seriius.org/pdfs/global-review-solar-tower-technology.pdf

[20] Q. Zhang, X. Li, Z. Wang, J. Zhang, B. El-Hefni, and L. Xu, “Modeling and simulation of a molten salt cavity receiver with dymola,” *Energy*, vol. 93, no. Part 2, pp. 1373 – 1384, 2015, accessed 24 October 2017.

[21] Powerfromthesun.net. Power from the sun :: Chapter 10. Accessed 24 October 2017. [Online]. Available: http://www.powerfromthesun.net/Book/chapter10/chapter10.html

[22] C. K. Ho and B. D. Iverson, "Review of high-temperature central receiver designs for concentrating solar power," *Renewable and Sustainable Energy Reviews*, vol. 29, pp. 835–846, 2014, accessed on 8 September 2017.

[23] K. Prashant. Concentrated solar thermal technology : Part ii – prashant karhade. Accessed 24 October 2017. [Online]. Available: http://prashantkarhade.com/concentrated-solar-thermal-technology-part-ii

[24] H. Müller-Steinhagen, "Concentrating solar thermal power," *Philosophical Transactions of the Royal Society A: Mathematical, Physical and Engineering Sciences*, vol. 371, 2013, accessed 24 October 2017.

[25] T. Menigault, G. Flamant, and B. Rivoire, "Advanced high-temperature two-slab selective volumetric receiver," *Solar energy materials*, vol. 24, no. 1-4, pp. 192–203, 1991, accessed on 20 August 2017.

[26] K. Kitzmiller and F. Miller, "Thermodynamic cycles for a small particle heat exchange receiver used in concentrating solar power plants," *Journal of Solar Energy Engineering*, vol. 133, no. 3, p. 031014, 2011, accessed 24 October 2017.

[27] J. Stekli, L. Irwin, and R. Pitchumani, "Technical challenges and opportunities for concentrating solar power with thermal energy storage," *Journal of Thermal Science and Engineering Applications*, vol. 5, no. 2, p. 021011, 2013, accessed 24 October 2017.

[28] U. Pelay, L. Lingai, F. Yilin, S. Driss, and R. Mark, "Thermal energy storage systems for concentrated solar power plants," *Renewable and Sustainable Energy Reviews*, vol. 79, pp. 82–100, 2017, accessed on 18 August 2017.

[29] U.S. Department of Energy. (2013) Concentrating solar power thermal storage system basics. Accessed on 18 August 2017. [Online]. Available: https://energy.gov/eere/energybasics/articles/concentrating-solar-power-thermal-storage-system-basics

[30] S. M. Flueckiger, B. D. Iverson, S. V. Garimella, and J. E. Pacheco, "System-level simulation of a solar power tower plant with thermocline thermal energy storage," *Applied Energy*, vol. 113, no. Supplement C, pp. 86 – 96, 2014, accessed 25 October 2017.

[31] M. Liu, N. H. S. Tay, S. Bell, M. Belusko, R. Jacob, G. Will, W. Saman, and F. Bruno, "Review on concentrating solar power plants and new developments in high temperature thermal energy storage technologies," *Renewable and Sustainable Energy Reviews*, vol. 53, pp. 1411–1432, 2016, accessed on 19 August 2017.

[32] International Energy Agency, "Electricity information," 2017, accessed on 21 August 2017. [Online]. Available: http://www.oecd-ilibrary.org/energy/electricity-information-2017_electricity-2017-en

[33] ——. (2015) Key electricity trends – based on monthly data. Accessed on 21 August 2017. [Online]. Available: https://www.iea.org/media/statistics/Keyelectricitytrends2015.pdf

[34] ——, “World energy outlook,” 2015, accessed on 22 August 2017.

[35] A. Graceffo. The impact of the us withdrawing from the paris accords. Accessed on 21 August 2017. [Online]. Available: https://www.foreignpolicyjournal.com/2017/07/13/the-impact-of-the-us-withdrawing-from-the-paris-accords/

[36] D. Carrington. The paris deal pullout is more damaging to the us than the climate. Accessed on 25 October 2017. [Online]. Available: https://www.theguardian.com/environment/2017/jun/01/donald-trump-paris-climate-deal-pullout-us-impact

[37] HELIOSCSP. Database of concentrated solar power projects all around the world. Accessed 25 October 2017. [Online]. Available: http://helioscsp.com/database-of-concentrated-solar-power-projects-all-around-the-world

[38] M. Mehos, C. Turchi, J. Jorgenson, P. Denholm, C. Ho, and K. Armijo, *On the Path to SunShot. Advancing Concentrating Solar Power Technology, Performance, and Dispatchability*, 2016, accessed on 23 August 2017.

[39] Solargis. World dni solar resource map. Accessed 25 October 2017. [Online]. Available: http://solargis.com/assets/graphic/free-map/GHI/Solargis-World-GHI-solar-resource-map-en.png

[40] L. Byrnes, C. Brown, J. Foster, and L. D. Wagner, “Australian renewable energy policy: Barriers and challenges,” *Renewable Energy*, vol. 60, pp. 711–721, 2013, accessed on 23 August 2017.

[41] Clean Energy Council, “Clean Energy Australia,” report, 2016, accessed on 23 August 2017. [Online]. Available: https://www.cleanenergycouncil.org.au/dam/cec/policy-and-advocacy/reports/2017/clean-energy-australia-report-2016/CEC_AR_2016_FA_WEB_RES.pdf

[42] G. Carr. (2012) Sunny uplands. Accessed on 23 August 2017. [Online]. Available: https://www.economist.com/news/21566414-alternative-energy-will-no-longer-be-alternative-sunny-uplands

[43] Pv price quotes. Accessed on 23 August 2017. [Online]. Available: http://pv.energytrend.com/pricequotes.html

[44] Lazard, “Lazard’s levelized cost of energy analysis – version 10.0,” report, 2016, accessed on 24 August 2017. [Online]. Available: https://www.lazard.com/media/438038/levelized-cost-of-energy-v100.pdf

[45] J. Duffie and W. Beckman, *Solar engineering of thermal processes*. John Wiley and Sons, New York, NY, 1980, accessed on 4 September 2017.

[46] J. Hansen. Storms of my grandchildren. Accessed 25 October 2017. [Online]. Available: http://www.columbia.edu/~mhs119/Storms/

[47] J. M. Lata, M. Rodríguez, and M. Á. de Lara, “High flux central receivers of molten salts for the new generation of commercial stand-alone solar power plants,” *Journal of Solar Energy Engineering*, vol. 130, no. 2, p. 021002, 2008, accessed on 5 September 2017.

[48] J. Cardemil, A. Starke, V. Scariot, I. Grams, and S. Colle, “Evaluating solar radiation attenuation models to assess the effects of climate and geographical location on the heliostat field efficiency in brazil,” *Energy Procedia*, vol. 49, pp. 1288–1297, 2014, proceedings of the SolarPACES 2013 International Conference, Accessed on 5 September 2017.

[49] M. Schmitz, P. Schwarzbözl, R. Buck, and R. Pitz-Paal, “Assessment of the potential improvement due to multiple apertures in central receiver systems with secondary concentrators,” *Solar Energy*, vol. 80, no. 1, pp. 111–120, 2006, accessed on 5 September 2017.

[50] D. Reznik, “Camera-based heliostat tracking controller,” Patent, 2009, US Patent App. 12/497,385.

[51] M. J. Montes, C. Rubbia, R. Abbas, and J. M. Martínez-Val, “A comparative analysis of configurations of linear fresnel collectors for concentrating solar power,” *Energy*, vol. 73, no. Supplement C, pp. 192 – 203, 2014, accessed 25 October 2017.

[52] D. L. Siebers and J. S. Kraabel, “Estimating convective energy losses from solar central receivers,” Sandia National Labs., Livermore, CA (USA), Tech. Rep., 1984, accessed on 5 September 2017.

[53] J. E. Pacheco, R. Bradshaw, D. Dawson, W. De la Rosa, R. Gilbert, S. Goods, M. Hale, P. Jacobs, S. A. Jones, G. J. Kolb *et al.*, “Final test and evaluation results from the solar two project,” *Report No. SAND2002-0120, Sandia National Laboratories*, vol. 45, 2002, accessed on 6 September 2017.

[54] Weather history for daggett-barstow airport. Accessed on 7 September 2017. [Online]. Available: https://www.wunderground.com/history/airport/KDAG/2017/7/27/DailyHistory.html?req_city=&req_state=&req_statename=&reqdb.zip=&reqdb.magic=&reqdb.wmo=&MR=1

[55] F. Eddhibi, M. B. Amara, M. Balghouthi, and A. Guizani, “Optical study of solar tower power plants,” in *Journal of Physics: Conference Series*, vol. 596, no. 1. IOP Publishing, 2015, p. 012018, accessed on 7 September 2017.

[56] J. M. Christian and C. K. Ho, “Cfd simulation and heat loss analysis of the solar two power tower receiver,” in *Proceedings of the ASME 2012 energy sustainability and fuel cell conference, San Diego, CA*, 2012. [Online]. Available: http://proceedings.asmedigitalcollection.asme.org/proceeding.aspx?articleid=1719551

[57] E. R. G. Eckert and R. M. Drake Jr, *Analysis of heat and mass transfer*. Hemisphere Publishing, 1987, accessed on 6 September 2017.

[58] C. J. Noone, “Optimization of central receiver concentrated solar thermal: site selection, heliostat layout & canting,” Ph.D. dissertation, Massachusetts Institute of Technology, 2011, accessed on 8 September 2017.

[59] J. Kim, J.-S. Kim, and W. Stein, “Simplified heat loss model for central tower solar receiver,” *Solar Energy*, vol. 116, no. Supplement C, pp. 314 – 322, 2015, accessed on 27 October 2017.

[60] J. Fang, J. Wei, X. Dong, and Y. Wang, “Thermal performance simulation of a solar cavity receiver under windy conditions,” *Solar Energy*, vol. 85, no. 1, pp. 126 – 138, 2011, accessed on 27 October 2017.

[61] P. Le Quéré, F. Penot, and M. Mirenayat, “Experimental study of heat loss through natural convection from an isothermal cubic open cavity,” *Sandia Laboratory Report No. SAND81-8014*, 1981, accessed on 27 October 2017.

[62] J. Salat, S. Xin, P. Joubert, A. Sergent, F. Penot, and P. L. Quéré, “Experimental and numerical investigation of turbulent natural convection in a large air-filled cavity,” *International Journal of Heat and Fluid Flow*, vol. 25, no. 5, pp. 824–832, 2004, selected papers from the 4th International Symposium on Turbulence Heat and Mass Transfer.

[63] R. J. LeVeque, “Finite difference methods for differential equations,” 2006, accessed on 28 October 2017.

[64] R. Courant, K. Friedrichs, and H. Lewy, “On the partial difference equations of mathematical physics,” *IBM journal of Research and Development*, vol. 11, no. 2, pp. 215–234, 1967, accessed on 13 September 2017.

[65] S. D. Conte and C. W. D. Boor, *Elementary Numerical Analysis: An Algorithmic Approach*, 3rd ed. McGraw-Hill Higher Education, 1980, accessed on 16 September 2017.

[66] R. Smith and A. Hutton, “The numerical treatment of advection: A performance comparison of current methods,” *Numerical Heat Transfer, Part A Applications*, vol. 5, no. 4, pp. 439–461, 1982, accessed on 16 September 2017.

[67] S. Patankar, *Numerical heat transfer and fluid flow*. CRC press, 1980, accessed on 18 September 2017.

[68] U. Ghia, K. N. Ghia, and C. Shin, “High-re solutions for incompressible flow using the navier-stokes equations and a multigrid method,” *Journal of computational physics*, vol. 48, no. 3, pp. 387–411, 1982, accessed on 19 September 2017.

[69] C. H. Marchi, R. Suero, and L. K. Araki, “The lid-driven square cavity flow: numerical solution with a 1024 x 1024 grid,” *Journal of the Brazilian Society of Mechanical Sciences and Engineering*, vol. 31, no. 3, pp. 186–198, 2009, accessed 25 October 2017.

[70] A. J. Chorin, “Numerical solution of the navier-stokes equations,” *Mathematics of computation*, vol. 22, no. 104, pp. 745–762, 1968, accessed on 21 September 2017.

[71] G. de Vahl Davis and I. Jones, “Natural convection in a square cavity: a comparison exercise,” *International Journal for numerical methods in fluids*, vol. 3, no. 3, pp. 227–248, 1983, accessed on 24 September 2017.

[72] G. de Vahl Davis, “Natural convection of air in a square cavity: a bench mark numerical solution,” *International Journal for numerical methods in fluids*, vol. 3, no. 3, pp. 249–264, 1983, accessed on 24 September 2017.

[73] T. L. Bergman and F. P. Incropera, *Fundamentals of heat and mass transfer*, 7th ed. John Wiley & Sons, 2011, accessed on 30 September 2017.

[74] P. Wang, Y. Zhang, and Z. Guo, “Numerical study of three-dimensional natural convection in a cubical cavity at high rayleigh numbers,” *International Journal of Heat and Mass Transfer*, vol. 113, pp. 217–228, 2017, accessed on 1 October 2017.

[75] O. Métais and M. Lesieur, “Spectral large-eddy simulation of isotropic and stably stratified turbulence,” *Journal of Fluid Mechanics*, vol. 239, pp. 157–194, 1992, accessed on 2 October 2017.

[76] Wikipedia. (2017) Law of the wall — wikipedia, the free encyclopedia. Accessed on 8 October 2017. [Online]. Available: https://en.wikipedia.org/w/index.php?title=Law_of_the_wall&oldid=800360259

[77] H. Zhang, F. X. Trias, A. Gorobets, Y. Tan, and A. Oliva, “Direct numerical simulation of a fully developed turbulent square duct flow up to re$_\tau$= 1200,” *International Journal of Heat and Fluid Flow*, vol. 54, pp. 258–267, 2015, accessed on 8 October 2017.

[78] Y.-F. Peng, Y.-H. Shiau, and R. R. Hwang, “Transition in a 2-d lid-driven cavity flow,” *Computers & Fluids*, vol. 32, no. 3, pp. 337–352, 2003, accessed on 3 October 2017.

[79] E. Erturk, T. C. Corke, and C. Gökçöl, “Numerical solutions of 2-d steady incompressible driven cavity flow at high reynolds numbers,” *International Journal for Numerical Methods in Fluids*, vol. 48, no. 7, pp. 747–774, 2005, accessed on 3 October 2017.

[80] C.-H. Bruneau and M. Saad, “The 2d lid-driven cavity problem revisited,” *Computers & Fluids*, vol. 35, no. 3, pp. 326–348, 2006, accessed on 3 October 2017.

[81] F. X. Trias, A. Gorobets, M. Soria, and A. Oliva, “Direct numerical simulation of a differentially heated cavity of aspect ratio 4 with rayleigh numbers up to 1011 – part i: Numerical methods and time-averaged flow,” *International Journal of Heat and Mass Transfer*, vol. 53, no. 4, pp. 665 – 673, 2010, accessed on 16 October 2017.

[82] ——, “Direct numerical simulation of a differentially heated cavity of aspect ratio 4 with rayleigh numbers up to 1011 – part ii: Heat transfer and flow dynamics,” *International Journal of Heat and Mass Transfer*, vol. 53, no. 4, pp. 674 – 683, 2010, accessed on 16 October 2017.

[83] F. X. Trias, D. Folch, A. Gorobets, and A. Oliva, “Building proper invariants for eddy-viscosity subgrid-scale models,” *Physics of Fluids*, vol. 27, no. 6, p. 065103, 2015, accessed on 18 October 2017.

[84] J. Smagorinsky, “General circulation experiments with the primitive equations: I. the basic experiment,” *Monthly weather review*, vol. 91, no. 3, pp. 99–164, 1963, accessed on 18 October 2017.

[85] F. Nicoud and F. Ducros, “Subgrid-scale stress modelling based on the square of the velocity gradient tensor,” *Flow, Turbulence and Combustion*, vol. 62, no. 3, pp. 183–200, 1999, accessed on 18 October 2017.

[86] A. W. Vreman, “An eddy-viscosity subgrid-scale model for turbulent shear flow: Algebraic theory and applications,” *Physics of Fluids*, vol. 16, no. 10, pp. 3670–3681, 2004, accessed on 18 October 2017.

[87] R. Verstappen, “When does eddy viscosity damp subfilter scales sufficiently?” *Journal of Scientific Computing*, vol. 49, no. 1, p. 94, 2011, accessed on 18 October 2017.

[88] J. Spencer, “Fourier series representation of the position of the sun,” *Search*, vol. 2, 1971, accessed on 28 October 2017.

[89] H. C. Hottel, “A simple model for estimating the transmittance of direct solar radiation through clear atmospheres,” *Solar Energy*, vol. 18, no. 2, pp. 129 – 134, 1976, accessed on 28 October 2017.

[90] P. Cooper, “The absorption of radiation in solar stills,” *Solar Energy*, vol. 12, no. 3, pp. 333 – 346, 1969, accessed on 28 October 2017.

A

Determining direct solar radiation

The Earth-Sun distance variates cyclically every year, influencing the extraterrestrial direct normal radiation G_{on}. According to Spencer (1971) [88], the latter can be calculated from eq. A.1:

$$G_{on} = G_{sc} \left(1 + 0.033 \, \cos \frac{360 \, n}{365} \right) \tag{A.1}$$

The beam component of the extraterrestrial radiation crosses the atmospheric layers. Hottel (1976) [89] suggested a model to calculate the beam radiation transmitted through the atmosphere. The atmospheric transmittance for beam radiation, defined as $\tau_b = \frac{G_{bn}}{G_{on}}$, where G_{bn} is the beam normal radiation, is equal to

$$\tau_b = a_0 + a_1 \, e^{-\frac{k}{\cos \theta_z}} \tag{A.2}$$

θ_z is the solar zenith angle (the angle between the normal of the Earth surface and the sun), and can be obtained with eq. A.3

$$\cos \theta_z = \cos \delta \, \cos \omega \, \cos \phi + \sin \delta \, \sin \phi \tag{A.3}$$

The angles appearing in the equation are shown in tab. A.1. The constants a_0, a_1, k appearing in eq. A.2

Table A.1: Important angles for the definition of the solar coordinates.

δ	the **solar declination** (the angular position of the sun at the solar noon) can be found by the equation of Cooper (1969) [90] $\delta = 23.45\,\sin\left(360\,\frac{284+n}{365}\right)$
ω	the **hour angle** (the sun displacement from the east to the west meridian due to terrestrial rotation) can be expressed as $\omega = 15\,t, \quad t = 0\,[\mathrm{h}]$ at noon, being t the solar time
ϕ	the **latitude** (the angular location respect to the equator) depends on the location of the collector

can be found from

$$a_0^* = 0.4237 - 0.00821\,(6 - A)^2 \tag{A.4a}$$

$$a_1^* = 0.5055 + 0.00595\,(6.5 - A)^2 \tag{A.4b}$$

$$k^* = 0.4237 - 0.00821\,(6 - A)^2 \tag{A.4c}$$

using the identities $r_0 = a_0/a_0^*$, $r_1 = a_1/a_1^*$ and $r_k = k/k^*$, where r_0, r_1 and r_k depend on climate types and are given in tab. A.2. The parameter A that appears in the eq. A.4a, A.4b and A.4c is the altitude of the site in kilometers.

Table A.2: Correction Factors for Climate Types, Hottel model.

Climate Type	r_0	r_1	r_k
Tropical	0.95	0.98	1.02
Mid-latitude Summer	0.97	0.99	1.02
Subarctic Summer	0.99	0.99	1.01
Mid-latitude Winter	1.03	1.01	1.00

Using the previous equations it is possible to calculate G_{bn} knowing G_{on}. Knowing G_{bn}, it is also possible to calculate its projection on a horizontal surface G_b, by means of the zenith angle

$$G_b = G_{bn}\,\cos\theta_z \tag{A.5}$$

where θ_z is obtained using eq. A.3.

B

Calculus

B.1 Calculus identities

$$\nabla(\phi\,\psi) = \phi\,\nabla\psi + \psi\,\nabla\phi \tag{B.1}$$

$$\nabla\cdot(\phi\,\mathbf{a}) = (\nabla\phi)\cdot\mathbf{a} + \phi\,(\nabla\cdot\mathbf{a}) \tag{B.2}$$

$$\nabla\cdot(\nabla\mathbf{a}^T) = \nabla\,(\nabla\cdot\mathbf{a}) \tag{B.3}$$

$$\nabla\cdot\nabla\mathbf{a} = \Delta\mathbf{a} = \nabla^2\mathbf{a} \tag{B.4}$$

$$\nabla\cdot(\nabla\times\mathbf{a}) = 0 \tag{B.5}$$

$$\tag{B.6}$$

B.2 Divergence theorem

The divergence theorem states that the volume integral of the divergence of a vector is equal to the net flux of the vector around the volume surfaces:

$$\int_V \nabla \cdot \mathbf{a}\, dV = \int_S \mathbf{a}\, \mathbf{n}\, dS \tag{B.7}$$

B.3 Stream function and vorticity in two dimensions

Given $\mathbf{u}(x, y) = u(x, y)\,\mathbf{i} + v(x, y)\,\mathbf{j}$ and $\boldsymbol{\psi} = \psi_1\,(x, y)\,\mathbf{i} + \psi_2\,(x, y)\,\mathbf{j} + \psi_3\,(x, y)\,\mathbf{k}$, it is possible to calculate the curl of $\boldsymbol{\psi}$ to apply the definition $\mathbf{u} = \nabla \times \boldsymbol{\psi}$

$$\mathbf{u} = \left(\frac{\partial \psi_3}{\partial y} - \cancelto{0}{\frac{\partial \psi_2}{\partial z}}\right)\mathbf{i} - \left(\frac{\partial \psi_3}{\partial x} - \cancelto{0}{\frac{\partial \psi_1}{\partial z}}\right)\mathbf{j} + \left(\frac{\partial \psi_2}{\partial x} - \frac{\partial \psi_1}{\partial y}\right)\mathbf{k} \tag{B.8}$$

Since $\mathbf{u}$ does not depend on the $\mathbf{k}$ component, the equation can be rewritten as

$$\mathbf{u} = \frac{\partial \psi_3}{\partial y}\,\mathbf{i} - \frac{\partial \psi_3}{\partial x}\,\mathbf{j} \tag{B.9}$$

Applying the vorticity definition $\boldsymbol{\omega} = \nabla \times \mathbf{u}$, instead

$$\nabla \times \mathbf{u} = \underset{\frac{\partial}{\partial z}=0}{\cancelto{0}{\left(0 - \frac{\partial v}{\partial z}\right)}}\mathbf{i} - \underset{\frac{\partial}{\partial z}=0}{\cancelto{0}{\left(0 - \frac{\partial u}{\partial z}\right)}}\mathbf{j} + \left(\frac{\partial v}{\partial x} - \frac{\partial u}{\partial y}\right)\mathbf{k} \tag{B.10}$$

Therefore, the vorticity can be expressed as $\boldsymbol{\omega} = \omega\,\mathbf{k}$ where $\omega = \frac{\partial v}{\partial x} - \frac{\partial u}{\partial y}$.

B.4 Conduction between different materials

Given a face f between the nodes R and L, the conduction of both sides of the face must be the same ($\dot{q}_{fl} = \dot{q}_{fr}$). The conduction heat flows can be expressed as

$$-\,k_L\,\frac{\partial T}{\partial s}\bigg|_f = -k_R\,\frac{\partial T}{\partial s}\bigg|_f \tag{B.11}$$

The equation can be discretized as

$$k_L\,\frac{T_f - T_L}{d_{Lf}} = k_R\,\frac{T_R - T_f}{d_{Rf}} \tag{B.12}$$

Solving eq. B.12 it is possible to extract T_f

$$T_f = \frac{\frac{k_R}{d_{Rf}}\, T_R + \frac{k_L}{d_{Lf}}\, T_L}{\frac{k_R}{d_{Rf}} + \frac{k_L}{d_{Lf}}} \tag{B.13}$$

Inserting T_f in the left or right-hand side of eq. B.11, the heat flux becomes

$$\dot{q}_f = \frac{T_R - T_L}{\frac{d_{Rf}}{k_R} + \frac{d_{Rf}}{k_R}} \tag{B.14}$$

The equation can be reformulated as

$$\dot{q}_f = k_f\, \frac{T_R - T_L}{d_{RL}} \tag{B.15}$$

where

$$k_f = \frac{d_{RL}}{\frac{d_{Rf}}{k_R} + \frac{d_{Rf}}{k_R}} \tag{B.16}$$

B.5 Air properties as a function of the temperature, extracted from Eckert & Drake

Dry air, $\mathbf{T = 100 \div 1300\,K}$

$$\rho\left[\frac{kg}{m^3}\right] = \frac{101325}{287\,T} \tag{B.17a}$$

$$k\left[\frac{W}{m\,K}\right] = \frac{2.648 \cdot 10^{-3}\,\sqrt{T}}{1 + (245.4/T) \cdot 10^{-12/T}} \tag{B.17b}$$

$$c_P\left[\frac{J}{kg\,K}\right] = 1034.09 - 2.849 \cdot 10^{-1}\,T + 7.817 \cdot 10^{-4}\,T^2 - 4.971 \cdot 10^{-7}\,T^3 + 1.077 \cdot 10^{-10}\,T^4 \tag{B.17c}$$

$$\mu\left[\frac{kg}{m\,s}\right] = \frac{1.458 \cdot 10^{-6}\,T^{1.5}}{T + 110.40} \tag{B.17d}$$

C

Additional figures

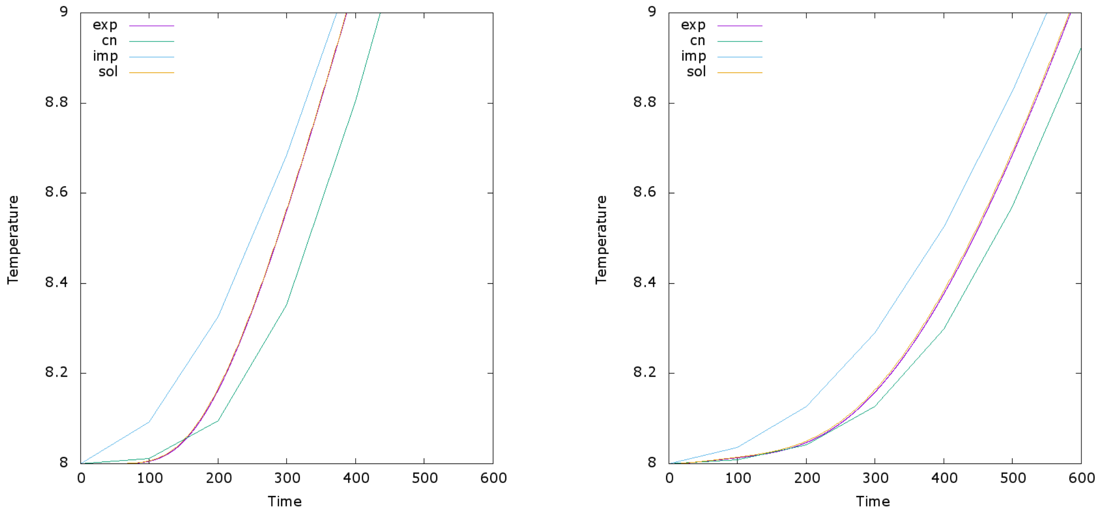

(a) Temperature at $P_1 = (0.65, 0.56)$ **(b)** Temperature at $P_2 = (0.74, 0.72)$

Figure C.1: 2D conduction – Temperature variation for the locations P_1 and P_2 for $t \in [0 : 600]\,\mathrm{s}$.

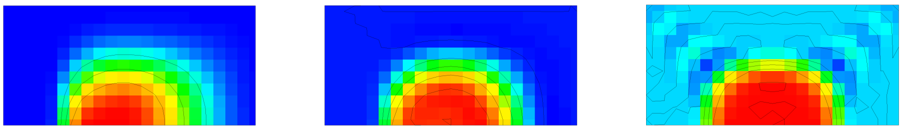

(a) UDS **(b)** SUDS **(c)** CDS

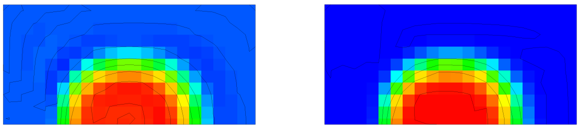

(d) QUICK **(e)** SMART

Figure C.2: Smith-Hutton problem – ϕ distribution for different convection schemes with a 21×10 mesh, $Pe = 10^6$.

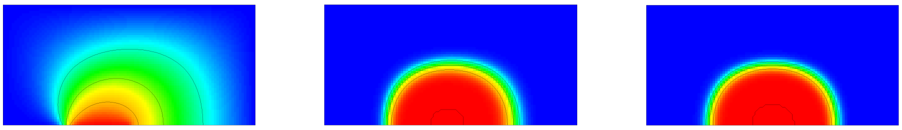

(a) $Pe = 10$ **(b)** $Pe = 1000$ **(c)** $Pe = 10^6$

Figure C.3: Smith-Hutton problem – ϕ distribution with a 101×50 mesh, SMART scheme.

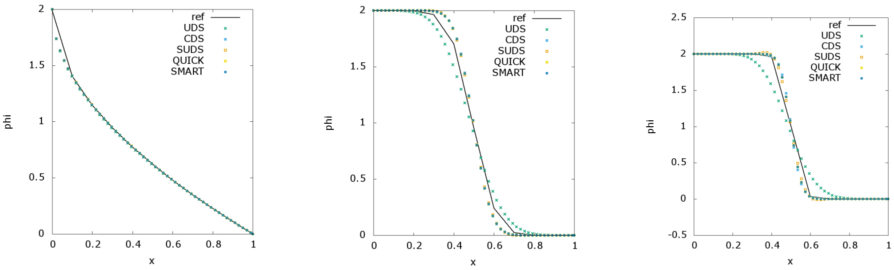

(a) $Pe = 10$ **(b)** $Pe = 1000$ **(c)** $Pe = 10^6$

Figure C.4: Comparison of different convection schemes – Smith-Hutton problem, outlet with a 101×50 mesh.

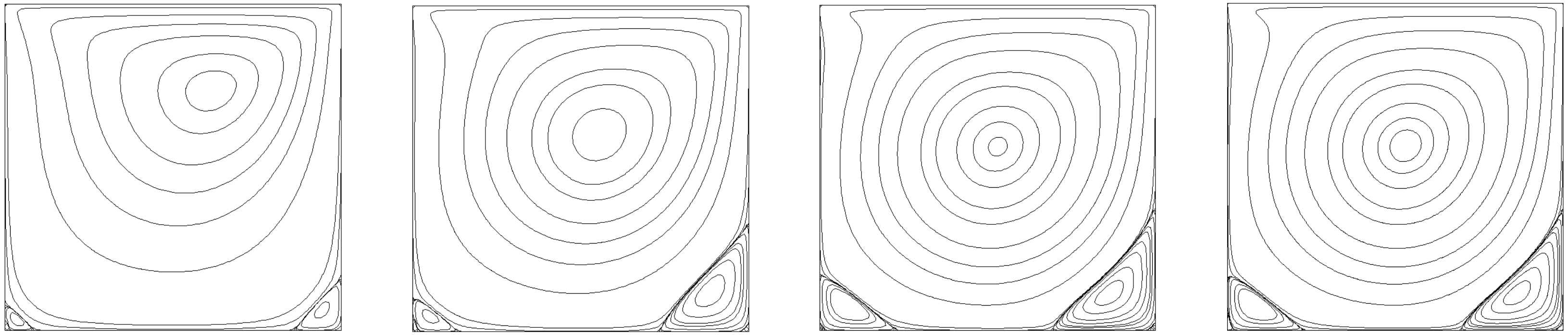

(a) $Re = 100$, mesh 128×128 **(b)** $Re = 400$, mesh 128×128 **(c)** $Re = 1000$, mesh 128×128 **(d)** $Re = 1000$, mesh 256×256

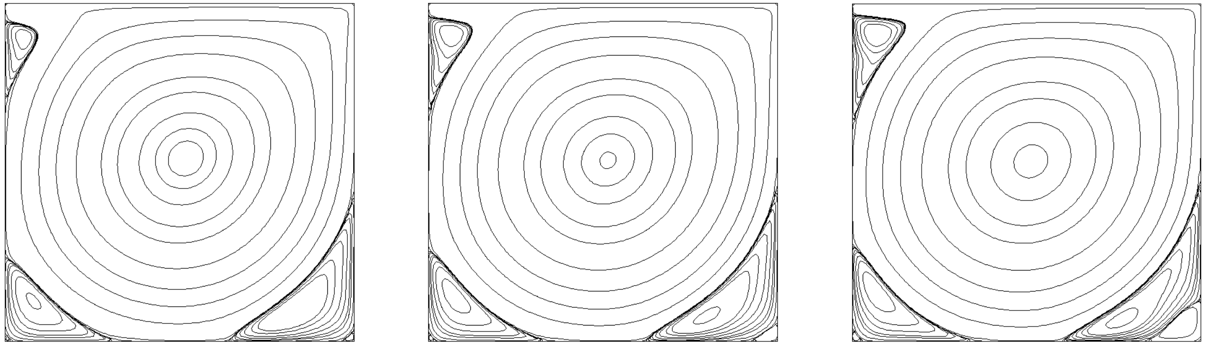

(e) $Re = 3200$, mesh 128×128 **(f)** $Re = 5000$, mesh 128×128 **(g)** $Re = 7500$, mesh 128×128

Figure C.5: Laminar driven cavity problem – stream function ψ map.

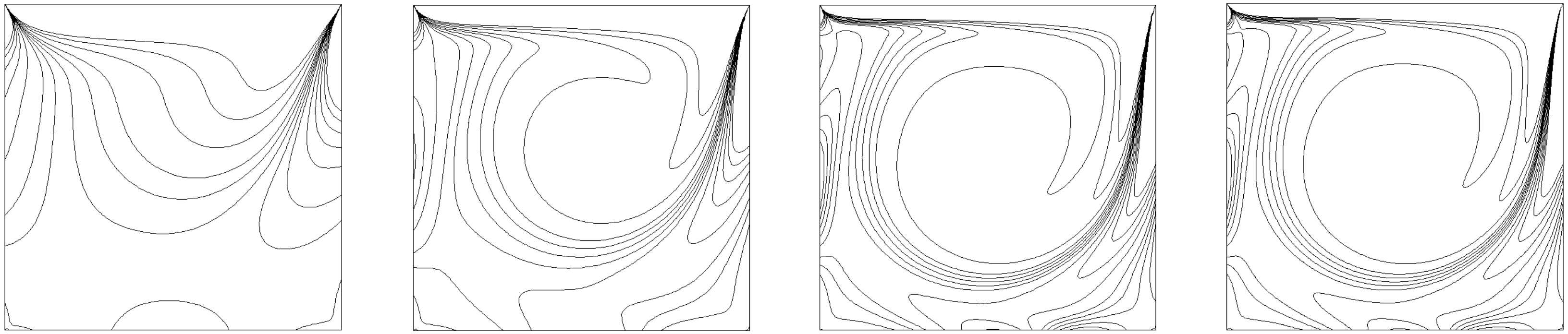

(a) $Re = 100$, mesh 128×128 **(b)** $Re = 400$, mesh 128×128 **(c)** $Re = 1000$, mesh 128×128 **(d)** $Re = 1000$, mesh 256×256

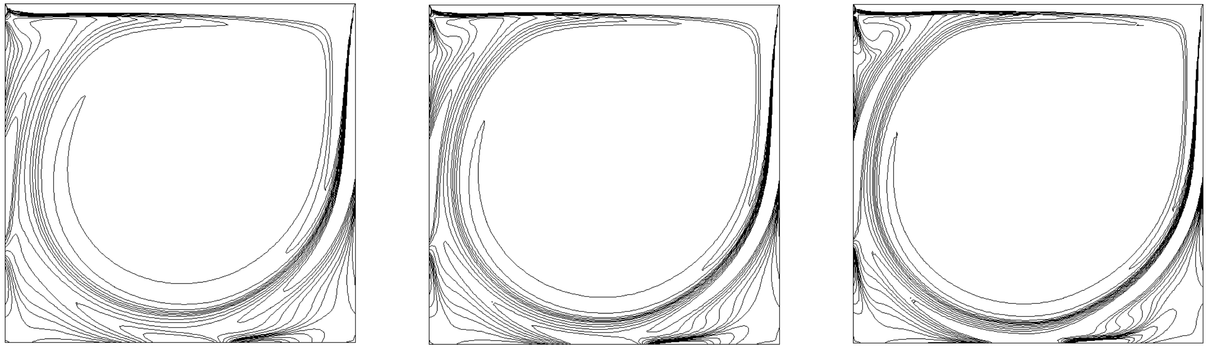

(e) $Re = 3200$, mesh 128×128 **(f)** $Re = 5000$, mesh 128×128 **(g)** $Re = 7500$, mesh 128×128

Figure C.6: Laminar driven cavity problem – vorticity ω map.

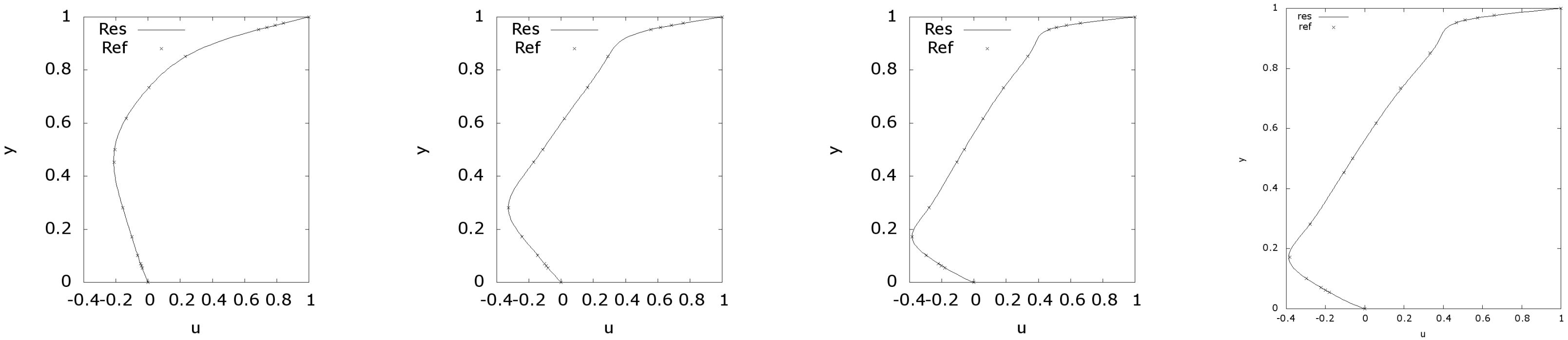

(a) $Re = 100$, mesh 128×128 **(b)** $Re = 400$, mesh 128×128 **(c)** $Re = 1000$, mesh 128×128 **(d)** $Re = 1000$, mesh 256×256

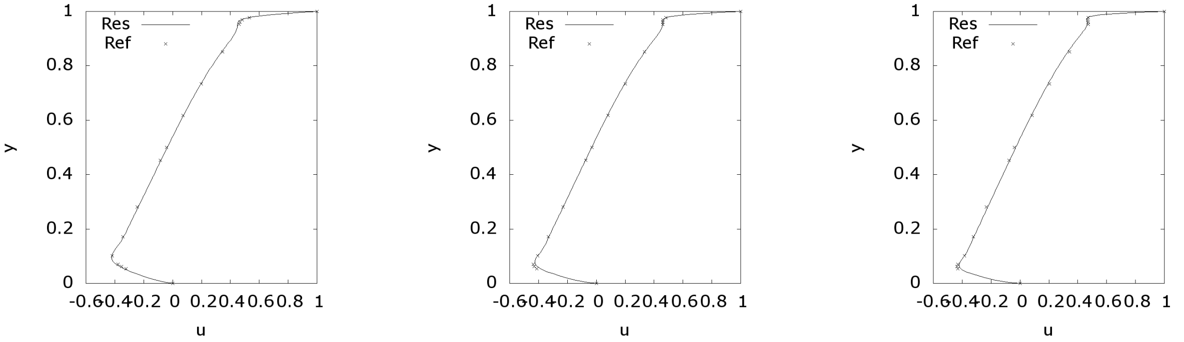

(e) $Re = 3200$, mesh 128×128 **(f)** $Re = 5000$, mesh 128×128 **(g)** $Re = 7500$, mesh 128×128

Figure C.7: Laminar driven cavity problem – horizontal velocity u map along the vertical line through the geometric center.

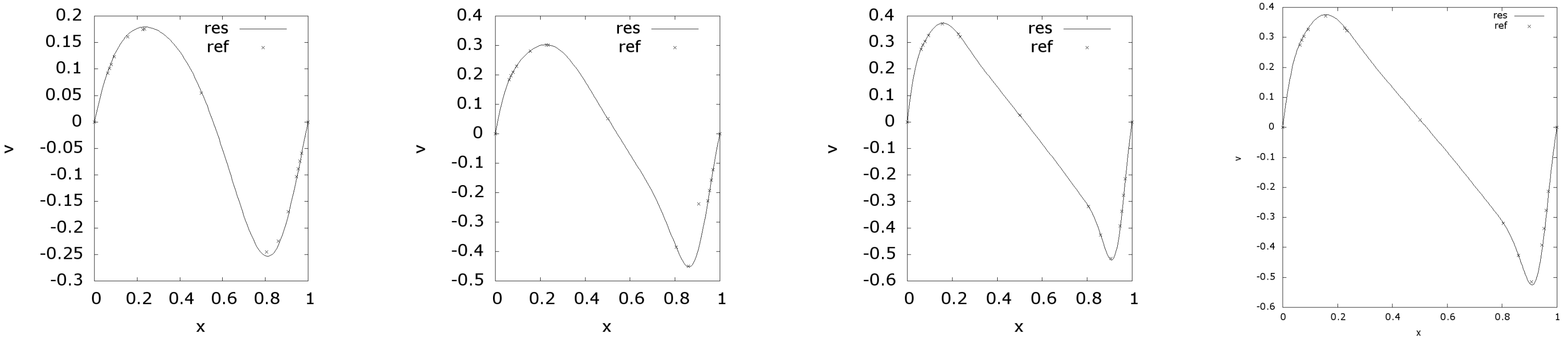

(a) $Re = 100$, mesh 128×128 **(b)** $Re = 400$, mesh 128×128 **(c)** $Re = 1000$, mesh 128×128 **(d)** $Re = 1000$, mesh 256×256

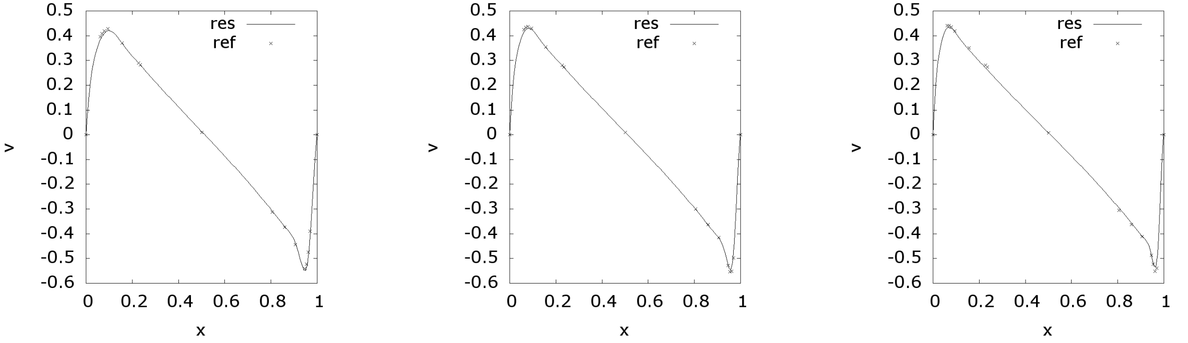

(e) $Re = 3200$, mesh 128×128 **(f)** $Re = 5000$, mesh 128×128 **(g)** $Re = 7500$, mesh 128×128

Figure C.8: Laminar driven cavity problem – vertical velocity v map along the horizontal line through the geometric center.

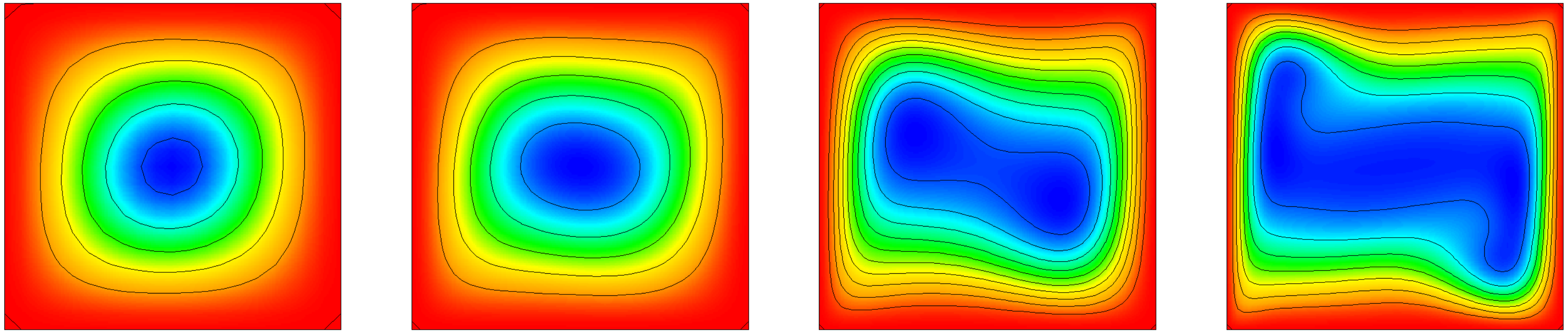

(a) $Ra = 10^3$ **(b)** $Ra = 10^4$ **(c)** $Ra = 10^5$ **(d)** $Ra = 10^6$

Figure C.9: Laminar 2D Boussinesq DHC – non-dimensional stream function ψ distribution.

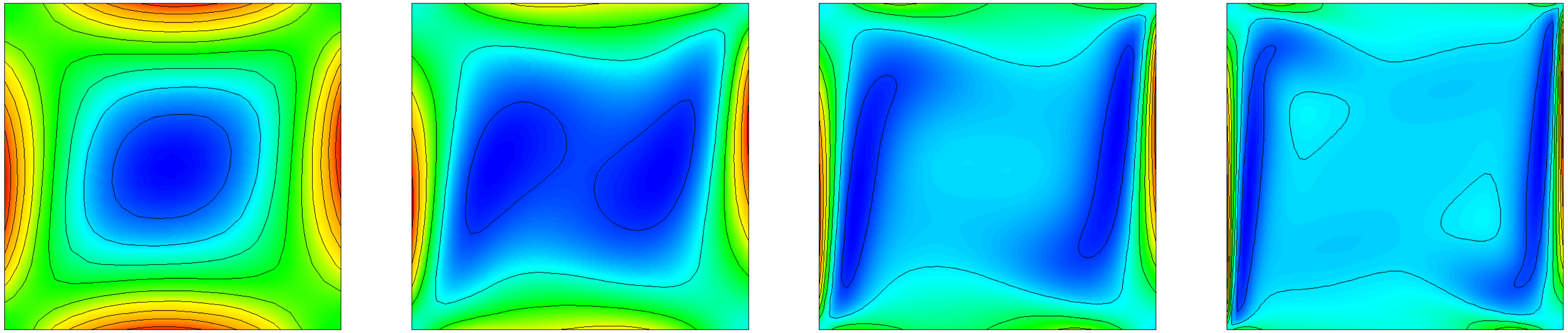

(a) $Ra = 10^3$ **(b)** $Ra = 10^4$ **(c)** $Ra = 10^5$ **(d)** $Ra = 10^6$

Figure C.10: Laminar 2D Boussinesq DHC – non-dimensional vorticity ω distribution.

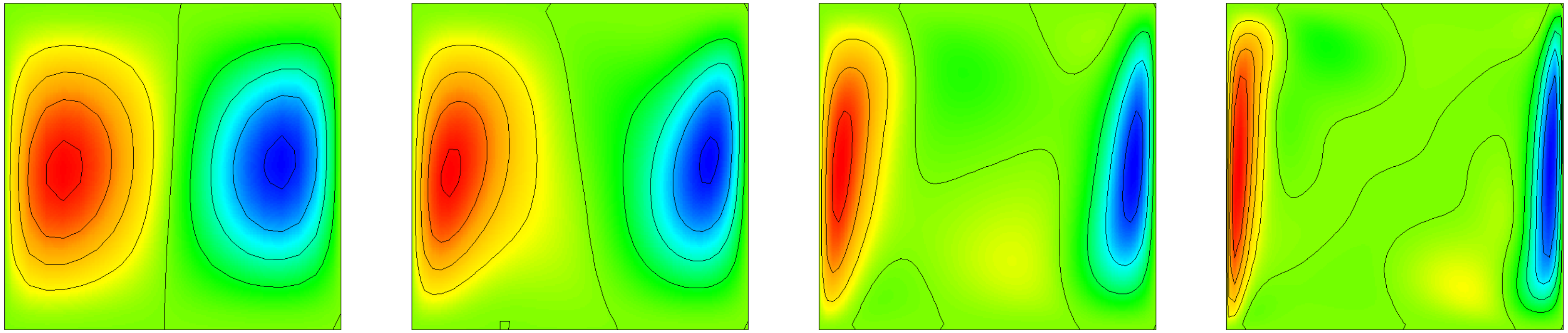

(a) $Ra = 10^3$ **(b)** $Ra = 10^4$ **(c)** $Ra = 10^5$ **(d)** $Ra = 10^6$

Figure C.12: Laminar 2D Boussinesq DHC – non-dimensional velocity w distribution, boussinesq fluid in a DHC.

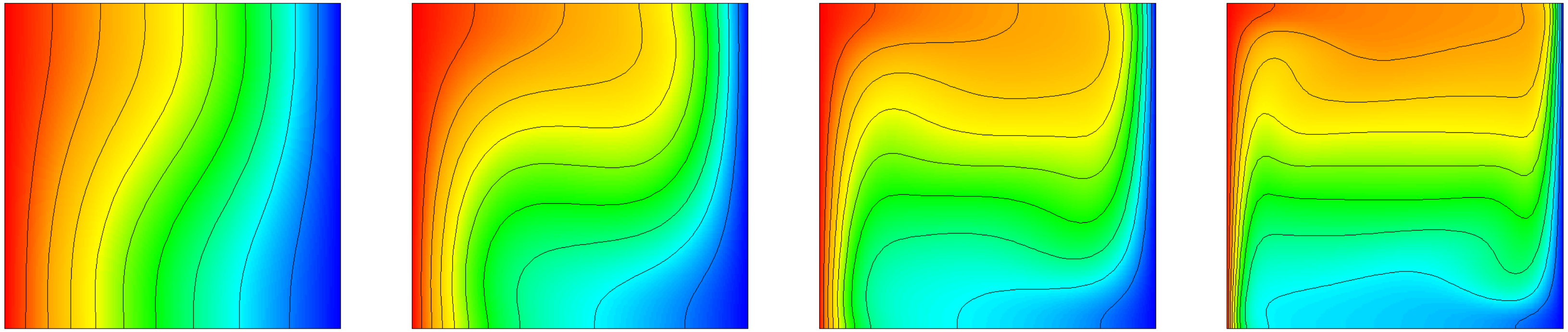

(a) $Ra = 10^3$ **(b)** $Ra = 10^4$ **(c)** $Ra = 10^5$ **(d)** $Ra = 10^6$

Figure C.11: Laminar 2D Boussinesq DHC – non-dimensional Temperature T distribution.

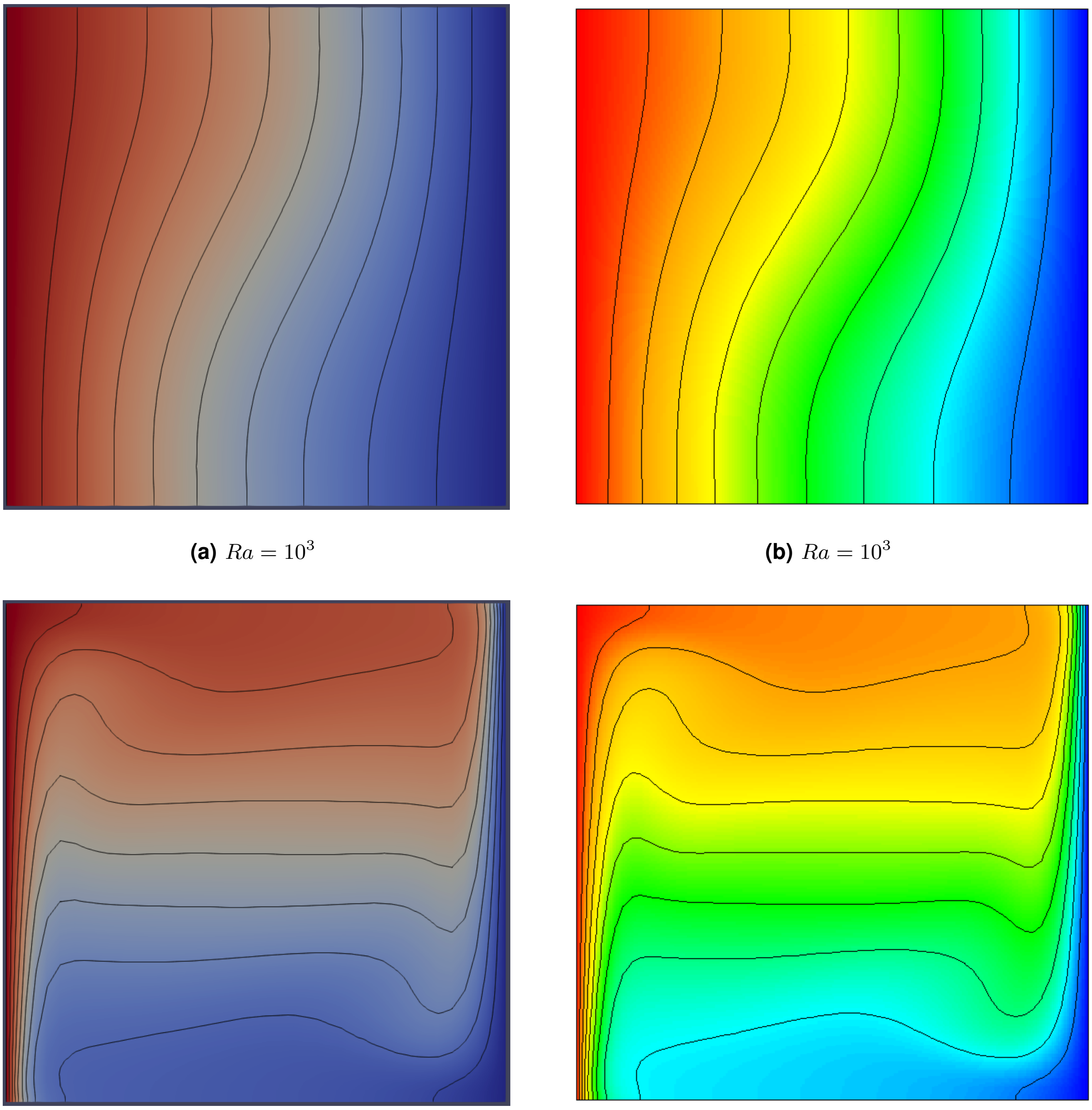

(a) $Ra = 10^3$ **(b)** $Ra = 10^3$

(c) $Ra = 10^6$ **(d)** $Ra = 10^6$

Figure C.13: Variable thermophysical properties DHC – 3D mid vertical planes temperature maps compared with 2D temperature map.

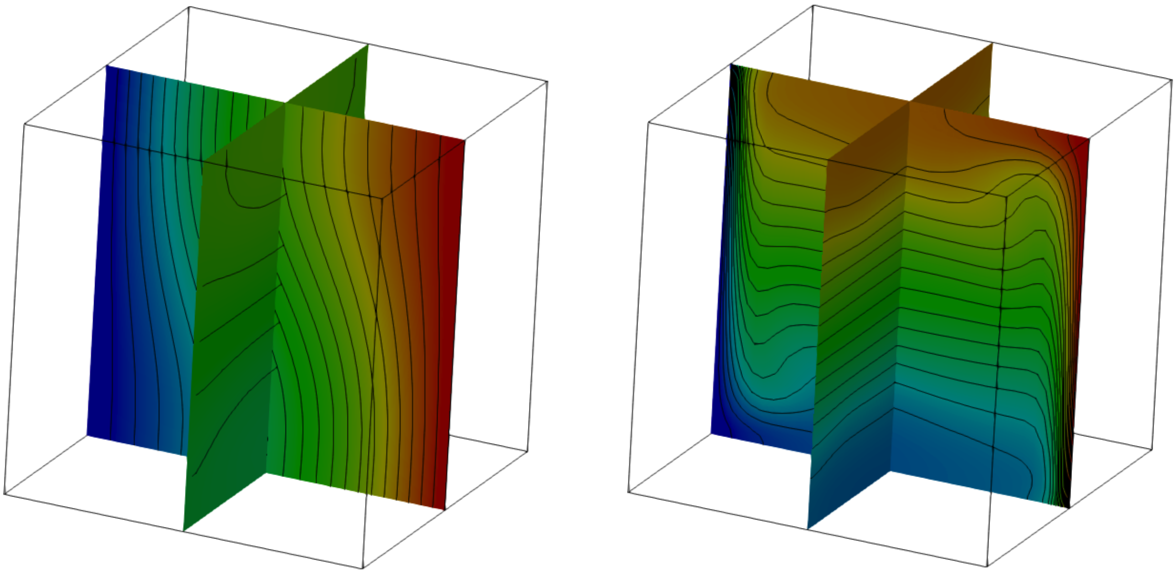

(a) $Ra = 10^3$ **(b)** $Ra = 10^6$

Figure C.14: Variable thermophysical properties DHC – 3D mid vertical planes temperature maps.

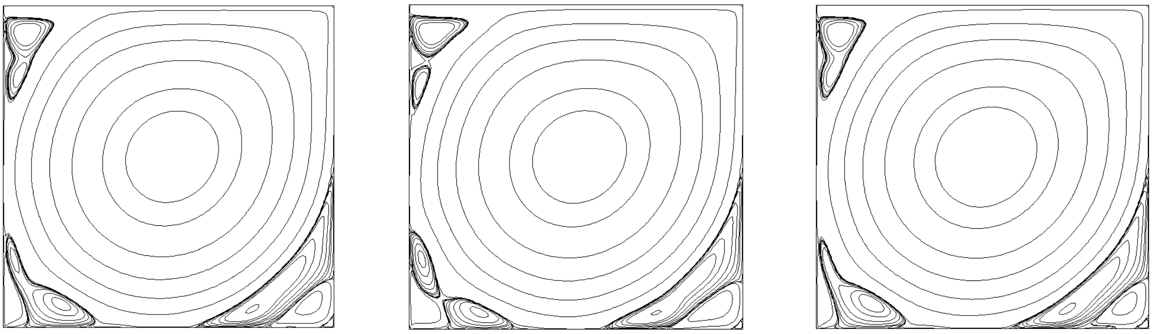

(a) $t = 401$ s **(b)** $t = 406$ s **(c)** $t = 407$ s

Figure C.15: Turbulent driven cavity – stream function maps for $Re = 10000$.

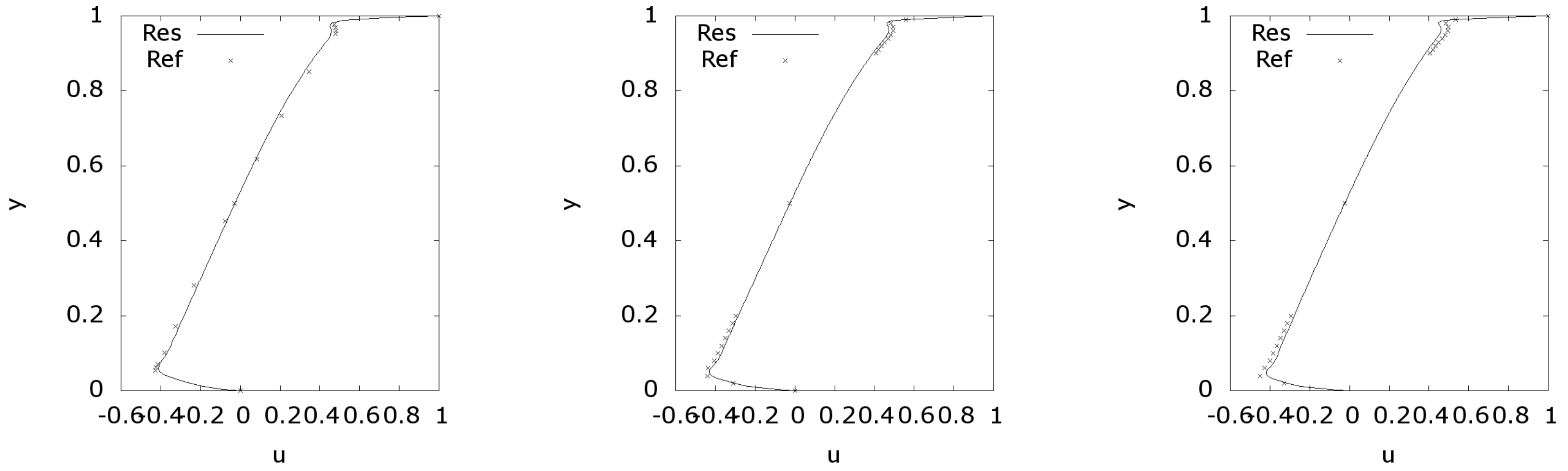

(a) $Re = 10000$, mesh 128×128

(b) $Re = 12500$, mesh 256×256

(c) $Re = 15000$, mesh 256×256

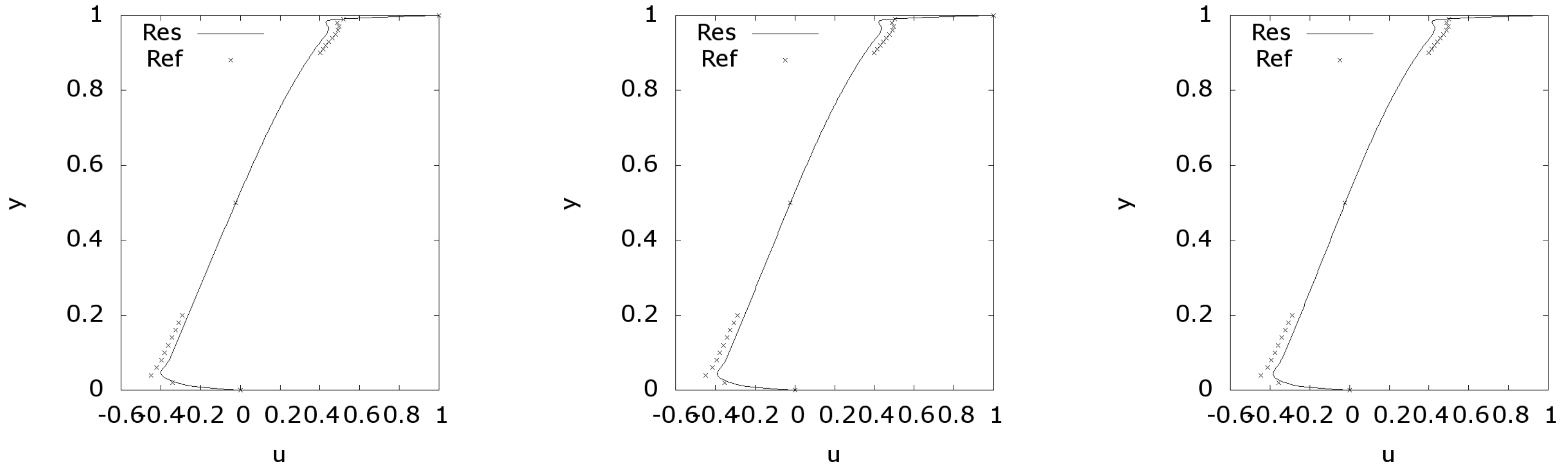

(d) $Re = 17500$, mesh 256×256

(e) $Re = 20000$, mesh 256×256

(f) $Re = 21000$, mesh 256×256

Figure C.16: Turbulent driven cavity – Time-averaged orizontal velocity u map along the vertical line through the geometric center.

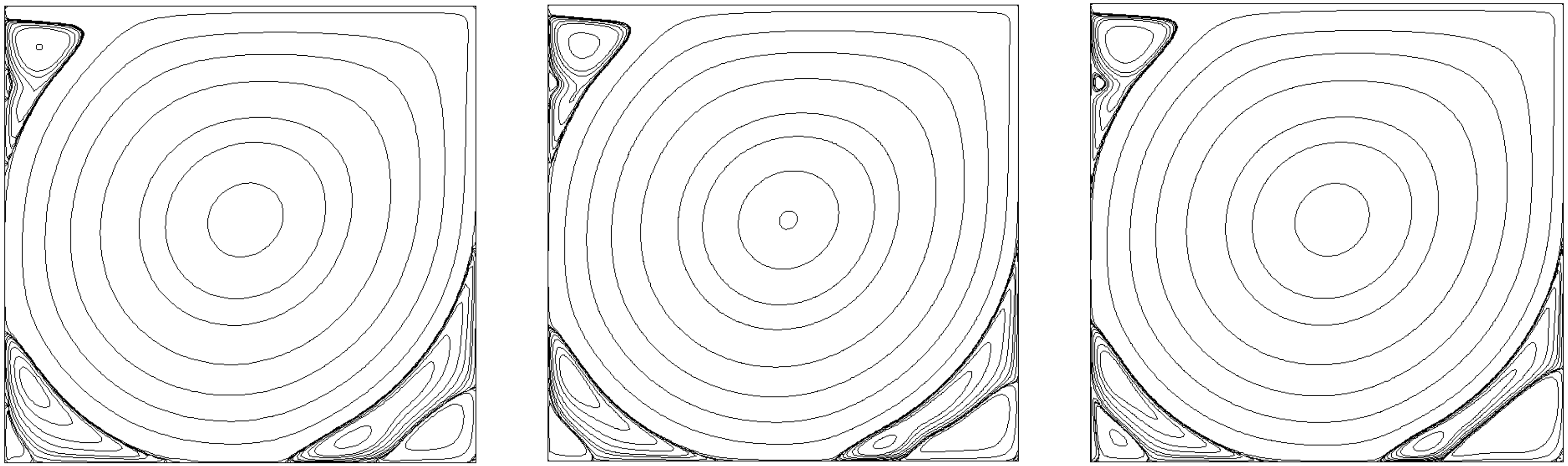

(a) $Re = 10000$, mesh 128×128 **(b)** $Re = 12500$, mesh 256×256 **(c)** $Re = 15000$, mesh 256×256

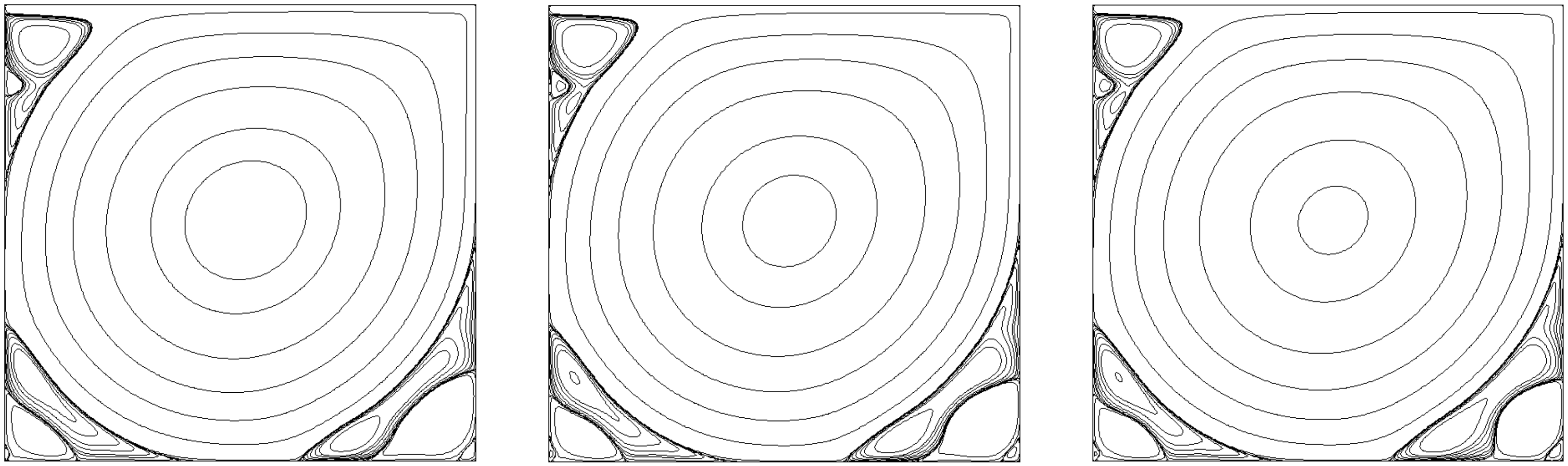

(d) $Re = 17500$, mesh 256×256 **(e)** $Re = 20000$, mesh 256×256 **(f)** $Re = 21000$, mesh 256×256

Figure C.17: Turbulent driven cavity – Time-averaged stream function ψ map.

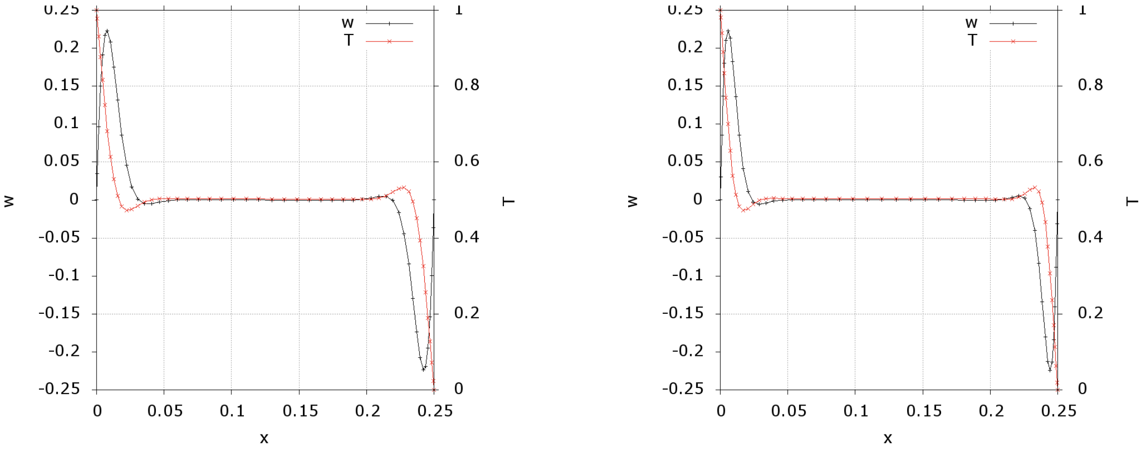

(a) $Ra = 6.4 \cdot 10^8$ **(b)** $Ra = 2 \cdot 10^9$

Figure C.18: Variable thermophysical properties 2D turbulent DHC – non-dimensional T and w time-averaged distribution along the mid z axis.